Investigation of Charge-Transfer Dynamics in Organic Materials for Solar Cells

Christian T. Weisspfennig

Brasenose College, Oxford



Thesis submitted in fulfilment of the requirements for the degree of Doctor of Philosophy at the University of Oxford

Trinity Term, 2013

Investigation of Charge-Transfer Dynamics in Organic Materials for Solar Cells

Christian T. Weisspfennig, Brasenose College, Oxford

Thesis submitted in fulfilment of the requirements for the degree of Doctor of Philosophy at the University of Oxford. Trinity Term, 2013

Abstract

This thesis improves our understanding of the charge-transfer dynamics in organic materials employed in dye-sensitized and nanotube-thiophene solar cells. For the purpose of this work, a femtosecond transient absorption spectroscopy setup was built. Additionally, microsecond transient absorption spectroscopy was utilised to explore dynamics on a longer time-scale.

In the first study, the dependence of dye regeneration and charge collection on the pore-filling fraction (PFF) in solid-state dye-sensitized solar cells (DSSCs) is investigated. It is shown that while complete hole transfer with PFFs as low as ∼30% can be achieved, improvements beyond this PFF are assigned to a stepwise increase in the charge-collection efficiency in agreement with percolation theory. It is further predicted that the charge-collection efficiency saturates at a PFF of ∼82%.

The study is followed by an investigation of three novel hole-transporting materials for DSSCs with slightly varying HOMO levels to systematically explore the possibility of reducing the loss-in-potential and thus improving the device efficiency. It is shown that despite one new HTM showing a 100% hole-transfer yield, all devices based on the new HTMs performed worse than those incorporating spiro-OMeTAD. Furthermore, it is demonstrated that the design of the HTM has an additional impact on the electronic density of states present at the TiO_2 electrode surface, and hence influences not only hole- but also electron-transfer from the sensitizer.

Finally, a study on a polymer-single-walled carbon nanotube (SWNT) molecular junction is presented. Results from femtosecond spectroscopic techniques show that the polymer poly(3-hexylthiophene) (P3HT) is able to transfer charges to the SWNT within 430 fs. Addition of excess P3HT polymer leads to long-lived free charges making these materials a viable option for solar cells.

Acknowledgements

I would like to thank my supervisor, Prof. Laura M. Herz, for her constant support and advice during my DPhil. I am very grateful for the opportunity to have worked here. I would also like to thank Dr. Henry J. Snaith for all the invaluable discussions and support.

Thanks to my collaborators Dr. Sam Stranks, Dr. Mike Lee, Derek Hollmann, Chris Menelaou, and Dr. Joel Teuscher. A special thanks goes to the past and present members of the Oxford Semiconductor Group, especially Callum, Hannah, Chaw-Keong, Christian, Chris, Katie, Sam, Priti, and Patrick. It has been a great pleasure working in this group. The good working atmosphere as well as the fun times in and outside the lab will be missed.

I am grateful to Brasenose College and its members for all the opportunities, the many dinners and the generally great time I have been given here at Oxford. I thank my family, my parents, Hartmut and Elisabeth, and my sister Kathrin for the encouragement and the support they have given me not only throughout my time as DPhil student, but throughout all my life. I would also like to thank Jon Rooney, Ruben Kubiak, Christoph Schäff, and Johannes Wenz.

Finally, I would like to acknowledge the Engineering and Physical Sciences Research Council (EPSRC) for funding my university and college fees, as well as John Larry Kelly, Jr. who, in 1956, established the theoretical foundations I have based my financial support on.

Contents

1 Introduction **1**

1.1 Introduction and Motivation 1

1.2 Thesis Outline 4

2 Theory and Background **7**

2.1 Organic Semiconductors 7

2.1.1 Introduction 7

2.1.2 Basic Properties 8

2.1.3 Charge Generation 9

2.1.4 Charge Transport 15

2.2 Carbon Nanotubes 21

2.2.1 Introduction 21

2.2.2 Structure 22

2.2.3 Electronic Properties 23

2.2.4 Optical Properties 24

2.3 Photovoltaic Cells 26

2.3.1 Introduction 26

2.3.2 Light Absorption and Photocurrent Generation 27

2.3.3 Current-Voltage Characteristic 28

2.3.4 Equivalent Circuit of a Photovoltaic Cell 29

2.3.5 Power-Conversion Efficiency 30

2.3.6 Efficiency Limitations 32

2.4 Organic Photovoltaics 33

2.4.1 Introduction 33

2.4.2 Light Absorption 34

2.4.3 Charge Dissociation and Recombination 35
2.5 Dye-Sensitized Solar Cells 38
2.5.1 Introduction 38
2.5.2 Architecture and Operation Principles 38
2.5.3 Solid-state Hole-Transporting Materials 42
2.5.4 Ionic Additives 48
2.6 Summary 50

3 Experimental Methods **53**
3.1 Introduction 53
3.2 UV-VIS Absorption Spectroscopy 53
3.3 Femtosecond Transient Absorption Spectroscopy 55
3.3.1 Introduction 55
3.3.2 Ultrashort Laser Pulses 55
3.3.3 Pump-Probe Technique 56
3.3.4 Nonlinear Optics 58
3.3.5 Second Harmonic Generation (SHG) 59
3.3.6 Supercontinuum Generation (SCG) 60
3.3.7 Optical Parametric Amplification (OPA) 62
3.3.8 Setup 63
3.3.9 Time Resolution 67
3.3.10 Artifacts 69
3.4 Microsecond Transient Absorption Spectroscopy 71
3.4.1 Introduction 71
3.4.2 Setup 71
3.5 Photoluminescence Upconversion Spectroscopy 72
3.5.1 Introduction 72
3.5.2 Setup 72
3.6 Time-Correlated Single Photon Counting (TCSPC) 74
3.7 Scanning Electron Microscopy (SEM) 74
3.8 Monte Carlo Simulations of Pore Infiltration 75
3.8.1 Introduction 75

3.8.2 Pore Filling Simulation . . . 75
3.8.3 Exciton Diffusion Simulation . . . 77
3.8.4 Hole-Transfer Simulation . . . 77
3.9 Sample Preparation Techniques . . . 78
3.10 Summary . . . 80

4 Dependence of Dye Regeneration and Charge Collection on the Pore-Filling Fraction in Solid-State Dye-Sensitized Solar Cells 81
4.1 Introduction . . . 81
4.2 Results and Discussion . . . 84
4.3 Conclusion . . . 102

5 Optimizing the Energy Offset Between Dye and Hole-Transporting Material in Solid-State Dye-Sensitized Solar Cells 105
5.1 Introduction . . . 105
5.2 Results and Discussion . . . 107
5.2.1 Material Properties . . . 107
5.2.2 Device Data . . . 109
5.2.3 Pore Filling . . . 112
5.2.4 Hole Transfer . . . 113
5.2.5 Charge Extraction . . . 123
5.3 Conclusion . . . 124

6 Ultrafast Charge Separation at a Polymer-Single-walled Carbon Nanotube Molecular Junction 127
6.1 Introduction . . . 127
6.2 Experimental Details . . . 128
6.3 Discussion . . . 137
6.4 Conclusion . . . 140

7 Conclusions 143
7.1 Summary of Key Results . . . 143
7.2 Outlook and Future Work . . . 145

A Appendix **147**

A.1 Derivation of Equation 4.5 147

Bibliography **149**

Abbreviations **165**

Publications

C. T. Weisspfennig, D. J. Hollman, C. Menelaou, S. D. Stranks, H. J. Joyce, M. B. Johnston, H. J. Snaith and L. M. Herz Dependence of Dye Regeneration and Charge Collection on the Pore-Filling Fraction in Solid-State Dye-Sensitized Solar Cells. *Advanced Functional Materials*, **24** (5), 1616–3028, 2014.

C. T. Weisspfennig, M. M. Lee, J. Teuscher, P. Docampo, S. D. Stranks, H. J. Joyce, H. Bergmann, I. Bruder, D. V. Kondratuk, M. B. Johnston, H. J. Snaith, and L. M. Herz Optimizing the Energy Offset Between Dye and Hole-Transporting Material in Solid-State Dye-Sensitized Solar Cells *The Journal of Physical Chemistry C*, **117** (39), 19850–19858, 2013.

S. D. Stranks, C. Weisspfennig, P. Parkinson, M. B. Johnston, L. M. Herz and R. J. Nicholas. Ultrafast charge separation at a polymer–single-walled carbon nanotube molecular junction. *Nano Letters*, **11**:66–72, 2011.

S. D. Stranks, C. Weisspfennig, P. Parkinson, M. B. Johnston, L. M. Herz and R. J. Nicholas. Ultrafast charge separation at a single-walled carbon nanotube-polymer interface. *MRS Proceedings*, **1286**:mrsf10-1286-e02-07, 2011.

S. D. Stranks, C. Yong, J. A. Alexander-Webber, C. Weisspfennig, M. B. Johnston, L. M. Herz and R. J. Nicholas Nanoengineering Coaxial Carbon Nanotube–Dual-Polymer Heterostructures. *ACS Nano*, **6**:6058–6066, 2012.

Chapter 1

Introduction

1.1 Introduction and Motivation

The rising demand and limited supply of the world's main energy sources as well as concerns over their negative effects on the climate have made the availability of clean, reliable and affordable energy one of the key challenges to humanity in the 21st century [1]. The world's average power consumption has risen from around 5 TW in 1971 to more than 11 TW in 2010 and is expected to increase to 20-23 TW in 2035 [2]. In 2008, renewable energy sources such as biofuel, biomass, wind power, hydropower, geothermal and solar energy accounted for only 18.5% of the world's electricity generation despite a rapid growth driven by a combination of cost reductions and market-creating policies [3]. To achieve international goals of reducing energy-related CO_2 levels by 50% by 2050, energy generation from renewable sources needs to double by 2020 [3]. This requires specific renewable energy sources, such as solar energy, to increase at a rate of 22% per year.

Solar energy is the cleanest, most abundant and inexhaustible of all the current energy sources [4]. The power from the sun incident on the surface of the Earth is estimated to be about 180,000 TW, more than 15,000 times the current power demand [4]. The current limited use of solar energy is caused by high production costs and long pay-back periods due to energy-intensive fabrication processes of the highly purified silicon employed in the standard solar cells [5]. Silicon solar cell costs have decreased from USD 4.00 per Watt in

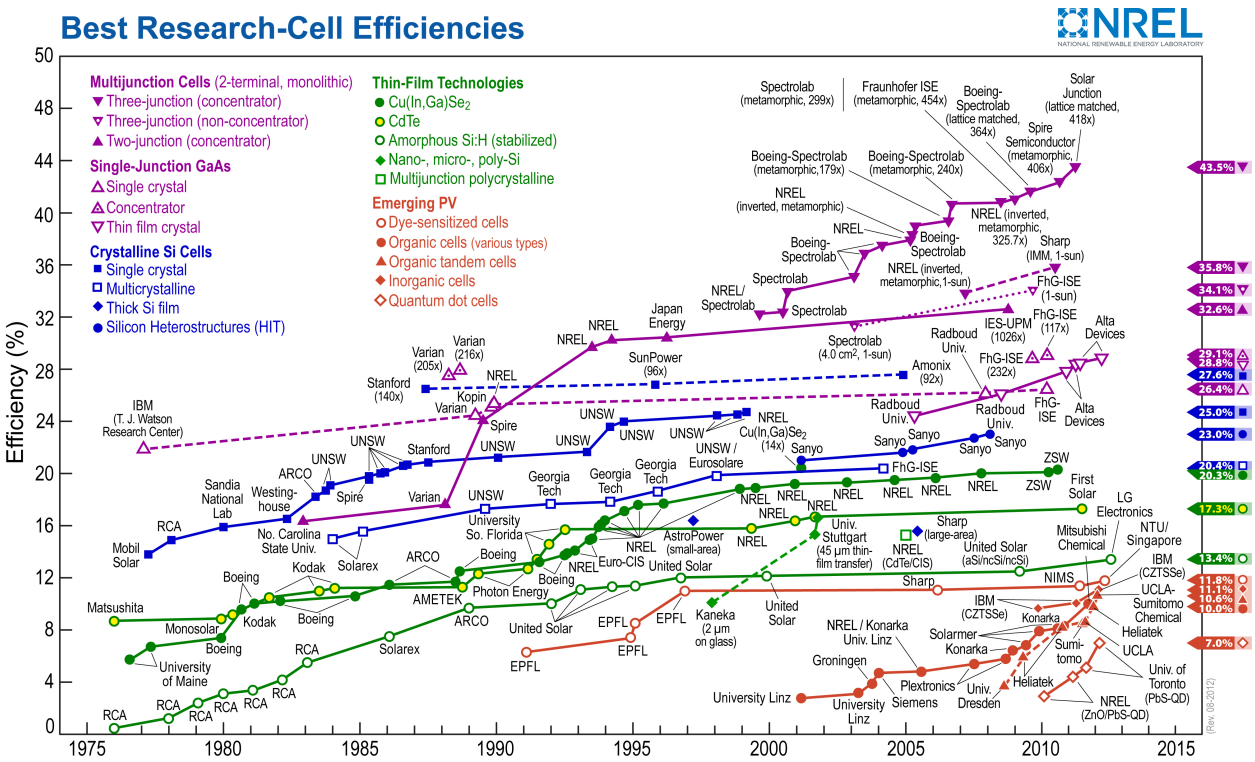

Figure 1.1: US National Renewable Energy Laboratory (NREL) data on the development of best research-cell efficiencies over time [7].

2008 to USD 1.25 per Watt in 2011 for power-conversion efficiencies ranging from 15% to 20% [6]. However, in order to compete with conventional energy sources, the development of even cheaper cells with higher power-conversion efficiencies is required.

Research on photovoltaic effects in organic solar cells in the 1950s and the first dye-sensitized solar cell in 1991 introduced new classes of low-cost photovoltaics [8, 9]. Further studies over the last two decades has resulted in steady improvements in power-conversion efficiencies reaching values above 10% as seen in Fig. 1.1. The unique properties of organic and dye-sensitized solar cells make them not only a viable substitute for current photovoltaic technology but introduce the possibility of new commercial applications for solar cells. Dye-sensitized solar cells separate light absorption, electron and hole transport using three different materials [10, 11]. By changing the light absorbing dye, solar cells of different colours can be produced which can be used for different design applications. Fig. 1.2 shows examples of dye-sensitized solar cells with different coloured dyes and one of the first commercial applications of these solar cells. Using this technique, it is also possible to produce



Figure 1.2: Left: Dye-sensitized solar cells in different colours. Photograph courtesy of Oxford Photovoltaics. Right: A dye-sensitized solar cell powered keyboard for the iPad. Photograph courtesy of G24 Innovations.

solar cells that are transparent to the human eye by using organic materials that absorb mostly infrared light. Recently, a polymer solar cell has been developed which reaches a 4% power-conversion efficiency while being 70% transparent in the visible spectrum [12]. Furthermore, these solar cells can be attached to the windows of houses or cars generating electricity in places currently not being used.

The maximum theoretical power-conversion efficiency for single-junction solar cells is just over 30% [13]. Deviations from this maximum for inorganic solar cells is mainly caused by the loss-in-potential, which is approximately the difference between the optical bandgap of the photoactive material divided by the charge of an electron, and the open-circuit voltage [6]. In contrast to inorganic solar cells, organic solar cells require an over-potential to drive charge generation/separation. Fig. 1.3 shows the theoretically attainable maximum power-conversion efficiencies of dye-sensitized solar cells versus the absorption onset of the light-absorbing dye for various loss-in-potentials. One of the biggest challenges for organic solar cells is therefore to minimize the loss-in-potential required to achieve efficient charge generation and charge separation.

Transient absorption spectroscopy (TAS) is one of the techniques used to study these processes. A laser pulse is used to photoexcite a material, while a second light pulse measures the change in absorbance for a specific wavelength over time. By choosing a wavelength a specific species absorbs, e.g. the electrons in the electron-transporting material, the con-

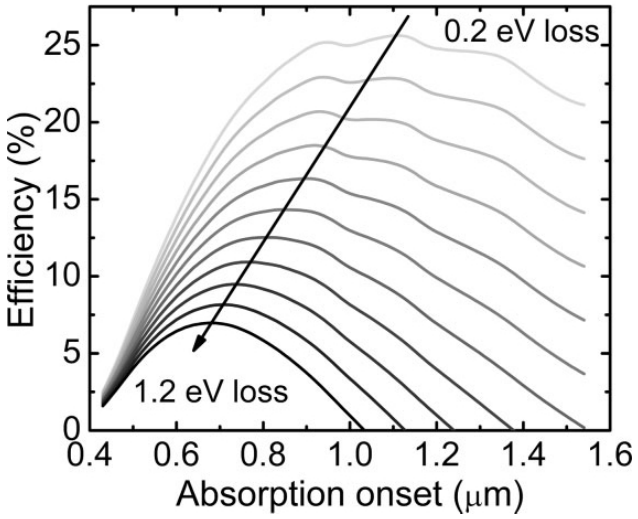

Figure 1.3: Maximum attainable power-conversion efficiency of dye-sensitized solar cells versus absorption onset of the light absorbing dye for various loss-in-potentials [14].

centration of charges and their lifetimes can be extracted. This thesis aims to enhance the understanding of the fundamental properties governing charge transfer and charge transport in organic and dye-sensitized solar cells by using transient absorption spectroscopy. Results from this work will lay the foundation for future improvements in cost and device efficiency.

1.2 Thesis Outline

Chapter 2 summarizes the theoretical background for this work. The fundamental characteristics of organic semiconductors and their effects on charge generation and charge transport are discussed. This is followed by an introduction to the operating principles and characterization of photovoltaic cells. The chapter concludes with a detailed discussion of the two specific types of solar cells studied in this work, polymer-single-walled carbon nanotube and dye-sensitized solar cells.

The experimental methods used in this study are summarized in Chapter 3. Part of this work was to design and set up a femtosecond transient absorption system which is discussed in detail, including the basic working principles and possible artifacts arising during measurements. Additionally, UV-VIS absorption spectroscopy as well microsecond transient absorption spectroscopy are presented.

Chapter 4 presents a study on the dependence of dye regeneration and charge collection on the pore-filling fraction in dye-sensitized solar cells. The incomplete filling of the pores with the hole-transporting material is believed to be one of the loss mechanisms in dye-sensitized solar cells [15]. Despite this importance, the exact mechanisms are still unknown. In the study presented here, microsecond transient absorption spectroscopy is employed to measure the hole-transfer rate from the dye to the hole-transporting material 2,2',7,7'-tetrakis(N,N-di-p-methoxyphenylamine)-9,9'-spirobifluorene (spiro-OMeTAD). Results show that complete hole transfer can be achieved with pore-filling fractions (PFFs) as low as ∼30% due to charges diffusing through the dye monolayer network first before transferring to the HTM. Improvements of the power-conversion efficiency beyond ∼30% pore filling are assigned to a higher charge-collection efficiency which is found to occur in steps in agreement with percolation theory. It was further predicted that for standard mesoporous TiO_2 with 20 nm pore size, the photocurrent should show no further improvement beyond a ∼83% pore-filling fraction.

In Chapter 5, a study on three novel hole-transporting materials for dye-sensitized solar cells is presented. Spiro-OMeTAD was one of the first solid-state hole-transporting materials and is to date still the most efficient material recently used in a solar cell achieving a record power-conversion efficiency of 7.2% [16, 17]. Further improvements, however, could be achieved by using hole-transporting materials with deeper highest occupied molecular orbital (HOMO) levels in order to reduce the loss-in-potential. Using femto- and microsecond transient absorption spectroscopy, the hole-transfer dynamics of three novel hole-transporting materials with slightly varying HOMO levels were studied and compared to spiro-OMeTAD to explore the possibility of reducing the loss-in-potential. It was found that based on a model of inhomogeneous broadening of the energy levels [18] a minimum energy offset of approximately 180 meV is required for 90% efficient hole transfer. In comparison, the hole-transfer yield of spiro-OMeTAD is shown to be 75% due to a smaller offset. Additionally, it is shown that the design of the HTM has an impact on the electronic density of states present at the TiO_2 electrode surface, and hence influences not only hole- but also electron-transfer from the sensitizer.

Chapter 6 presents a study investigating the charge photogeneration dynamics at the interface formed between single-walled carbon nanotubes (SWNTs) and poly(3-hexylthiophene) (P3HT). Photovoltaic devices employing SWNTs blends with conjugated polymers are expected to achieve good power-conversion efficiencies due to the many promising properties of SWNTs such as their large aspect ratio, high carrier mobility and controllable solubilisation in polymer solution [19, 20]. However, power-conversion efficiencies have been low so far [21–24]. Using several ultrafast spectroscopic techniques it is shown that charge transfer does occur between a single molecular layer of P3HT wrapped around a (6,5) SWNT which is known to form a type-II heterojunction [25]. Addition of excess P3HT to the blend leads to long-term charge separation making the incident-photon-to-electron conversion efficiency (IPCE) comparable to conventional P3HT-fullerene blends.

Lastly, Chapter 7 summarizes the key results of this work and explains its implications for organic and dye-sensitized solar cells. Additionally, the future work that may follow from the findings is discussed.

Chapter 2

Theory and Background

2.1 Organic Semiconductors

2.1.1 Introduction

Inorganic materials, such as silicon or gallium arsenide, have been used in the semiconductor industry since the mid 1900's. In contrast, only at the end of the 1970's, when doped polyacetylene was found to be a highly conducting polymer, extensive research started to be conducted on organic semiconductors [26]. Organic semiconductors have relatively low production and processing costs compared to inorganic semiconductors. Additionally, they exhibit a high flexibility and a low weight [27]. These properties offer a wide range of potential applications such as organic light-emitting diodes (OLED) [28–31], photovoltaics (OPV) [9, 32] or field-effect transistors (OFET) [33–36]. For most applications the charge transport within the organic semiconductor plays a major role in the performance of the device. Properties such as transport efficiency or heat loss can be optimized once the charge carrier dynamics are better understood. It is therefore of great interest to study these processes.

2.1.2 Basic Properties

The properties of organic semiconductors are derived from the carbon atom. The ability to absorb light and transport charge carriers derives from the sp^2-hybridization. Two sp^2-hybridized carbon atoms form a σ-bond by an overlap of their sp^2-orbitals. Additionally, the perpendicular p_z-orbitals form π-bonds. The energy gap between the occupied bonding orbital and the unoccupied anti-bonding orbital of the σ-bond is higher than the energy gap of the π-bonds which lies in the range of the visible and ultraviolet spectrum (see Fig. 2.1).

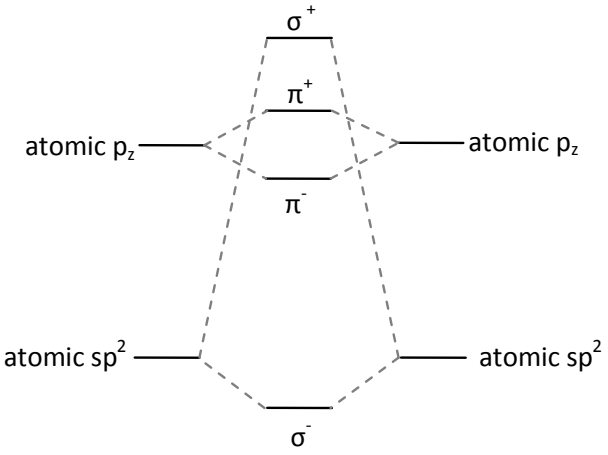

Figure 2.1: Energy states of two sp^2-hybridized carbon atoms [37].

Organic semiconductors can be broadly divided into two major classes, small molecules and polymers. While polymers are long molecular chains, small molecule organic semiconductors consist of molecules with about 10-100 atoms having a filled π-electron system [38]. Organic semiconductors are fabricated using simple and low-cost techniques such as spin-coating, ink-jet printing and spray deposition. Intermolecular bonding of organic molecules results from the relatively weak van der Waals force. As a result, the electronic wave function is strongly localized to individual molecules. Inorganic semiconductors, in contrast, have stronger intermolecular forces due to covalent bonding. Due to the weak intermolecular force in organic materials, compared to the stronger intramolecular forces, the electronic excited states of many organic crystals exhibit very similar properties to those of free molecules. This has led to the model of an "oriented gas" for organic molecular crystals [39]. Disor-

dered organic materials however generally show a broadened energy spectrum that differs considerably from the spectrum in the gas phase. Additionally, due to the low dielectric constant of approximately 3-5, photoexcitation in organic semiconductors usually results in the generation of a tightly bound electron-hole pair in the form of an exciton with binding energies of ∼0.3-0.5 eV, as discussed in more detail in the following sections [40–42].

2.1.3 Charge Generation

The intrinsic charge carrier density n of a semiconductor is given by

$$n = N_0 \exp\left(-\frac{E_g}{2k_B T}\right) \tag{2.1}$$

where N_0 is the effective density of states and E_g the energy gap. In organic semiconductors the energy gap is larger than the thermal energy at room temperature ($E_g \gg kT$). Only a small number of electrons are thus thermally activated into a higher excited state which leads to a low intrinsic charge carrier density. Instead, next to (electro-)chemical and field-effect doping, charge carriers can be created either by injection from a contact or through photoexcitation.

Charge Injection

In the case of charge injection two contacts, usually planar metal plates, are connected to the material. Charges are injected from one contact and removed from the other one. Two types of contacts need to be distinguished. For the first type of contacts, the Ohmic contact, the current is limited by the organic semiconductor rather than by the contact. For the second type, the current is contact-limited. The first case is useful when the charge transport is studied within the organic semiconductor and the second case can be used when the control of the current should be independent of external resistance [43].

Photoexcitation

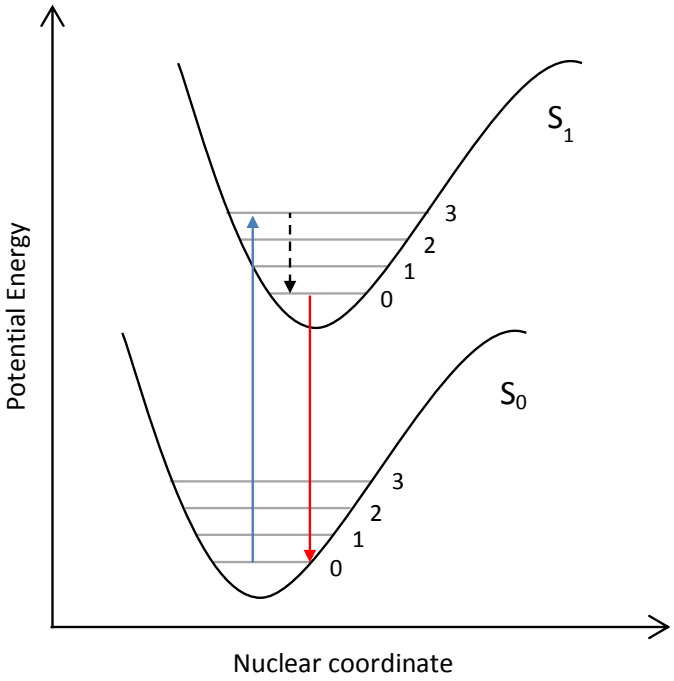

Figure 2.2: Energy diagram for photoexcitation and photoluminescence. The arrows indicate the Frank-Condon transitions while the dashed line indicates the non-radiative transition from the higher vibrational to the ground vibrational state. The energy difference between excitation and emission transition is the Stokes shift [44].

In the case of photoexcitation in organic materials, the absorption of light promotes an electron from the highest-occupied molecular orbital (HOMO) level into a higher excited state. These optical transitions must obey both momentum and spin selection rules. Electronic states with net spin zero are called singlets (S), states with a spin of one are called triplets (T). The lowest optical energy transition is from the HOMO level into the lowest-unoccupied molecular orbital (LUMO) level, corresponding to a transition from the singlet S_0 state into the first single state S_1. Due to the electron-lattice coupling the electronic S_i levels are split further into vibrational energy levels, as schematically shown in Fig. 2.2 using the Frank-Condon principle, which states that an electronic transitions is most likely to occur without changes in the nuclear coordinates.

The possible type of transitions of an isolated molecule are shown in Fig. 2.3. Through absorption of a photon, an electron is promoted from the ground state S_0 to the first or

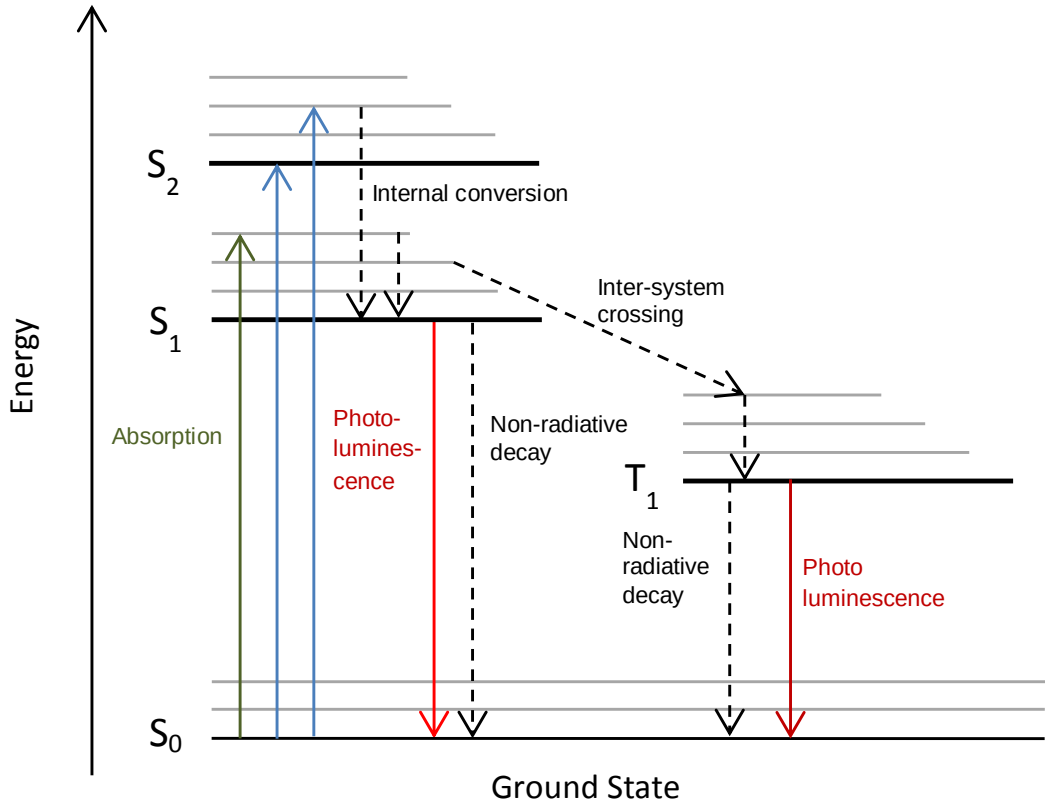

Figure 2.3: Jablonski diagram of electronic transitions in an organic semiconductor.

second singlet state S_1 or S_2. Direct transitions into higher singlet states are possible as well. The electron can then decay non-radiatively or through photoluminescence after internal conversion occurred. Alternatively, the electron can transfer via a vibrational transition involving spin-orbit coupling, so called inter-system crossing, from a singlet into a triplet state. Direct excitations from the ground state into the triplet state cannot occur, with the exception of multi-photon processes, since a photon is a spin-1 particle. From the triplet state, the electron can again decay either non-radiatively or through photoluminescence after possible internal conversion. Not shown are possible transitions from the first triplet state to higher triplet states which can also occur.

In organic semiconductors, due to the low dielectric constant on the order of 3-5 and due to weak non-covalent electronic interaction between organic molecules, the electron and hole are usually tightly bound in the form of an exciton after photoexcitation [40].

This stands in contrast to the free electron-hole pairs that are created in most inorganic semiconductors. Excitons can be divided into two limiting cases, Frenkel excitons and Mott-Wannier excitons. Frenkel excitons are bound very tightly by the Coulomb force and obtain orbital sizes that are small compared to the lattice constant (typically smaller than 5 Å). Mott-Wannier excitons, in contrast, are bound very loosely and exhibit orbital sizes which are large in comparison with the lattice constant (typically in the range of 40-100 Å). Excitons in organic semiconductors usually exhibit binding energies of 0.3-0.5 eV [41, 42].

Charge Transfer and Separation

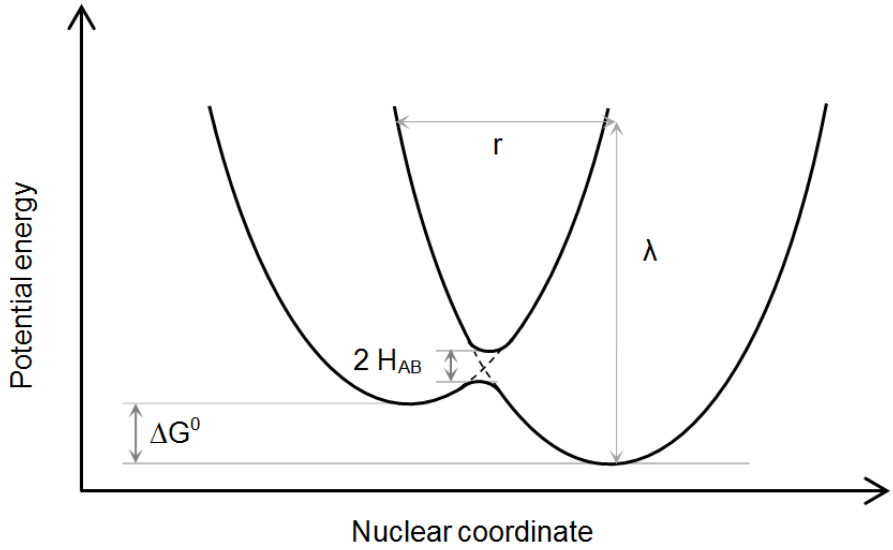

Figure 2.4: Energy diagram for electron transfer. ΔG^0: Difference in free energy between the initial and the final state, i.e. the driving force of the process. $|H_{AB}|$: Electronic coupling between initial and final state. λ: Reorganization energy.

In order for separation of the exciton into a free electron and hole to occur, the exciton binding energy needs to be overcome. This can be possible, for example, between a donor and acceptor molecule at a type-II heterojunction. Charge transfer can then be described by considering the overlap between the lowest vibrational state in the donor's excited state with the vibrational state of the acceptor with similar energy, as schematically shown in Fig. 2.4. The process is driven by the driving force ΔG_0, while the reorganisation energy λ puts a barrier to the transformation. Mathematically, electron transfer can be described

using the the classical Marcus theory which was first formulated in 1956 [45]. The rate of electron transfer is given by [46]

$$k_{et} = \frac{2\pi}{\hbar}|H_{AB}|^2 \frac{1}{\sqrt{4\pi\lambda k_b T}} \exp\left(\frac{(\lambda + \Delta G^0)^2}{4\lambda k_b T}\right) \tag{2.2}$$

where ΔG^0 is the difference in free energy between the initial and the final state, i.e. the driving force of the process, $|H_{AB}|$ is the electronic coupling between initial and final state, and λ is the reorganization energy. Thus, electron transfer is described by only three factors: the driving force, reorganizational energy, and the electronic coupling between initial and final state. To include intramolecular vibrations into the equation, the reorganizational energy can be extended by adding the intramolecular reorganizational energy which is given by [47]

$$\lambda_{\text{tot}} = \lambda_0 + \lambda_i \tag{2.3}$$

$$\lambda_i = \sum_l \lambda_{i,l} = \frac{1}{2}\sum_l f_l(\Delta q_{e,l})^2 \tag{2.4}$$

where f_l is the force constant of the lth normal mode and Δq_e is the change in equilibrium positions between the reactants and products.

Even after adding the intramolecular reorganizational energy, several problems with this basic formulation remain, e.g. partially incorrect temperature dependence and an excessively rapid falloff in the electron transfer rate with ΔG^0 [47]. These are caused because the classical Marcus theory assumes that the barrier must be crossed and quantum mechanical tunneling is not considered. However, modes coupled to electron transfer must be treated as quantum mechanical if the spacing between the vibrational levels is large compared to thermal energies, i.e. [47]

$$\frac{\hbar\omega_l}{k_bT} \gg 1 \text{ quantum} \tag{2.5}$$

$$\frac{\hbar\omega_l}{k_bT} \ll 1 \text{ classical} \tag{2.6}$$

This can be seen when the harmonic oscillator vibrational energy levels are inserted within the potential curves, as schematically shown in Fig. 2.5. Tunneling occurs optimally between the ground level in the reactant and the ninth vibrational level in the product curve. Thus, quantum mechanical tunneling needs to be taken into account in the electron transfer rate.

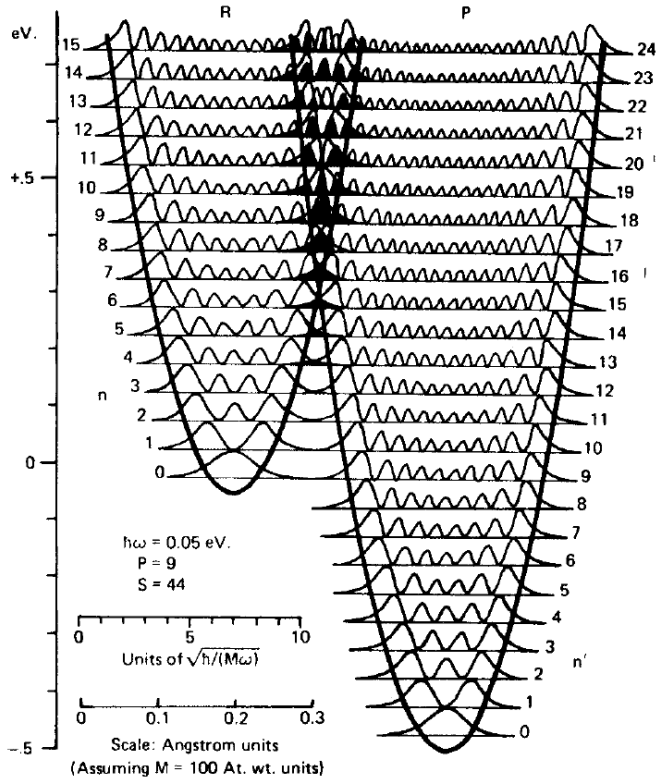

Figure 2.5: Schematic one-dimensional representation of the intersection between reactant and product vibrational levels [48].

Eqn. 2.2 can be generalised for non-adiabatic electron transfer for one coupled mode with $\hbar\omega_l \gg k_T$ to [49]

$$k_{et} = \frac{2\pi}{\hbar} H_{RP}^2 \frac{1}{\sqrt{4\pi\lambda_0 k_b T}} (FC) \tag{2.7}$$

where FC is the Frank-Condon factor

$$\mathrm{FC} = \sum_{\nu'} \exp(-S) \frac{S^{\nu'}}{\nu'!} \exp \frac{-(\lambda_0 + \nu'\hbar\omega + \Delta G^0)^2}{4\lambda_0 k_b T}. \tag{2.8}$$

Eqn. 2.8 is the sum over all possible vibrational overlap integrals between the initial vibrational level ν and the final level ν' [47]. The exponential term in the sum is the population of molecules in the assembly having the required energy to undergo electron transfer with energy conservation through channel $\nu = 0 \rightarrow \nu'$.

2.1.4 Charge Transport

Conductivity and mobility

In absence of any external potential, charge transport in organic semiconductors is purely diffusive and can be described by a simple diffusion equation [50]:

$$\left\langle x^2 \right\rangle = nDt \tag{2.9}$$

where $\langle x^2 \rangle$ is the mean-square displacement of the charges, D is the diffusion coefficient, t is the time, and n is an integer equal to 2, 4, or 6 for 1D, 2D, or 3D systems, respectively. The relationship between the mobility μ and the diffusion is given by the Einstein relation:

$$\mu = \frac{eD}{k_B T} \tag{2.10}$$

Using this relation, the relative broadening can described by

$$\frac{\langle \Delta x^2 \rangle}{\langle x \rangle} = \frac{k_B T}{eE} (2Dt)^{-1/2}. \tag{2.11}$$

If an external electric field is applied, it induces a drift of the charge carriers and transport can be described by the mean drift velocity $\nu_{\mathbf{D}}$. It is given by

$$\nu_{\mathbf{D}} = \mu \cdot \mathbf{E} \tag{2.12}$$

where $\mathbf{E}$ the electric field. Thus, μ is the intrinsic fundamental material property determining charge transport in an organic semiconductor. In the case of a non-cubic crystal μ is a tensor. The current density $\mathbf{j}$ is given by

$$\mathbf{j} = \sigma \mathbf{E} \tag{2.13}$$

where σ denotes the specific electrical conductivity. The current density $\mathbf{j}$ is related to the mean drift velocity by

$$\mathbf{j} = q\ n\ \nu_{\mathbf{D}} \tag{2.14}$$

where q is the elementary charge and n the charge carrier density. The relationship between conductivity and charge carrier mobility is then given by

$$\sigma = q\ n\ \mu \tag{2.15}$$

In inorganic semiconductors, due to the strong covalent bonding between the molecules, charge transport usually takes place easily. In organic semiconductors, however, the weak intermolecular forces lead to a strongly localized electronic wave function, as described earlier. As a result, the mobility in organic semiconductors can be orders of magnitude lower than in their inorganic counterparts.

Influence of Disorder on the Charge Transport

At a microscopic level two limiting cases of charge transport are distinguished: band and hopping transport. The method of transport for a specific organic semiconductor depends strongly on its intrinsic order.

In highly ordered organic semiconductors bandlike transport can be observed with mobilities exhibiting values in the range of 1 to 10 cm^2/Vs [40]. This low range compared to inorganic semiconductors, where the mobility is $\sim$3000 cm^2/Vs, is caused by the relatively small bandwidth of molecular organic solids due to a low delocalization of the wave function. It should be noted however that these observations only hold true for high-purity materials which can be obtained by zone refining in combination with other methods [51]. In the following, only such materials will considered.

In the case of bandlike transport a decrease in temperature increases the mobility. Charge carriers in the transport band possess a quasi-momentum $\mathbf{k}$ and are scattered by phonons. A decrease in temperature results in a decrease of the phonon density and thus in an increase of charge carrier mobility. This dependence of mobility in ordered organic solids on the temperature is described by a power law [40]

$$\mu(T) \propto T^{-n} \tag{2.16}$$

where n is a constant that is greater than unity. Its exact value depends on the material and the direction of the crystal that is studied.

In addition to temperature dependence, some ordered organic molecular solids also show a dependence of the charge drift mobility on the applied electric field, if the electric field strength is high. This dependence is described by a model of Shockley where charge carriers are assumed to scatter from the crystal potential which is deformed by the longitudinal lattice vibrations. The relationship is given by [52]

$$\mu(E) = \mu_0\sqrt{2}\left\{1 + \left[1 + \frac{3\pi}{8}\left(\frac{\mu_0 E}{c_L}\right)^2\right]^{1/2}\right\}^{-1/2} \tag{2.17}$$

where μ_0 is the low-field mobility and c_L is the speed of sound. Thus, the mobility shows a below-linear dependency on the electric field.

In contrast to ordered semiconductors, charge transport in strongly disordered semicon-

ductors is believed to be governed by hopping between sites [53, 54]. Changes in conformation at each site causes the energy levels of the transport states within the material to be inhomogeneously distributed and charges to be localized on the molecules. Charge carriers then need to hop between these states to move through the semiconductor. The energy difference between two transport states is overcome by the absorption or emission of a phonon. The hopping rate from a state j to a state i has been described by Miller and Abrahams and is given by [54]

$$w_{ij} = \nu_0 \exp(-2\Gamma R_{ij}) \begin{cases} \exp\left(-\frac{\epsilon_i - \epsilon_j}{k_B T}\right) & \epsilon_i > \epsilon_j \\ 1 & \epsilon_i < \epsilon_j \end{cases} \tag{2.18}$$

where ν_o is the phonon frequency, Γ the inverse localization length, R_{ij} the distance between the two localized states i and j, and ϵ_i is the energy at state i. Along with others, charge transport in disordered semiconductors was theoretically described by Bässler [55]. In this model, the energy distribution of the charge carrier transport states is assumed to be a Gaussian function G(E) of the density of states (DOS):

$$G(E) = \frac{1}{\sqrt{2\pi\sigma^2}} \exp\left(\frac{-E^2}{2\sigma^2}\right) \tag{2.19}$$

where σ is the width of the distribution. Additionally, disorder in position and a hopping rate according to Eqn. 2.18 is assumed. Application of this model in a Monte Carlo simulation showed a dependence of the mobility upon temperature in low electric fields according to

$$\mu = \mu_0 \exp\left[-\left(\frac{T_0}{T}\right)^2\right] \tag{2.20}$$

where μ_0 is the mobility of the disorder-free semiconductor at $T \to \infty$ and $T_0 = 2\sigma/3k$. This result shows an important consequence of the hopping mechanism in disordered organic semiconductors in contrast to ordered organic semiconductors: the mobility depends

inversely on the temperature. As charge transport requires phonon absorption or emission, an increase in phonons due to a higher temperature results in an increase of charge carrier mobility.

The electric field dependence of disordered organic solids has been determined in several experiments to generally follow the so-called Poole-Frenkel law [43]:

$$\mu(E) = \mu(E = 0) \exp(\beta\sqrt{E}) \tag{2.21}$$

where $\mu(E = 0)$ is the charge drift mobility in the absence of an electric field and β is the so-called field amplification factor. Both parameters generally exhibit a dependence on the temperature. The dependence on the temperature and electric field strength can be combined to form the following term:

$$\mu(E, T) = \mu_\infty \exp\left(-\frac{\Delta_0 - \beta_{PF}\sqrt{E}}{kT_{\text{eff}}}\right) \tag{2.22}$$

Here, μ_∞, Δ_0 and β_{PF} are constants. T_{eff} is given by

$$T_{\text{eff}}^{-1} = T^{-1} - (T')^{-1} \tag{2.23}$$

with $(T')^{-1}$ being a constant.

Additionally, the transients of disordered organic semiconductors show a different behaviour to those of ordered organic semiconductors. Disorder in position and energy of a material causes the charges to spread out over the whole sample. Eqn. 2.11 no longer holds true and the transport becomes dispersive [56].

In weakly disordered materials the transport mechanism generally lies in between the two limiting cases. Whether band or hopping transport is the predominant method needs to be determined in each case. In the band model the charge carriers become delocalized. Therefore, a description in terms of the band model can be used, if the diffusion length is

long compared to the lattice constant a_0 [43]:

$$\lambda \gg a_0 \tag{2.24}$$

If Eq. 2.24 does not hold true, hopping between sites best describes the charge transport. Generally, even weak disorder can considerably distort the conduction and valence band, and charge transport needs to be described in the context of a hopping model.

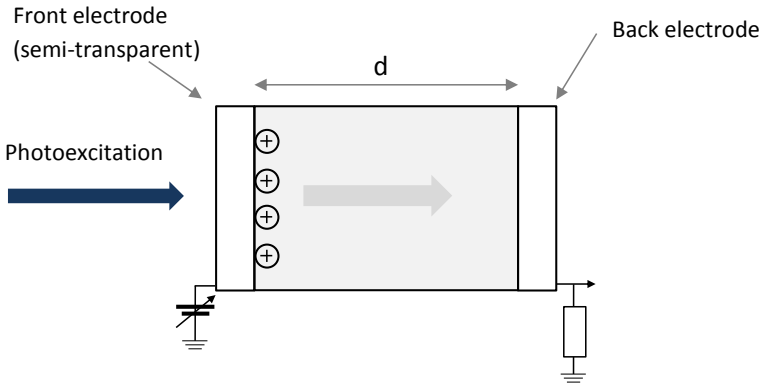

Figure 2.6: Schematic of a time-of-flight experiment measuring the hole drift mobility.

Experimentally, mobilities of charge carriers in organic semiconductors can be studied, along with other methods, in so-called time-of-flight (TOF) experiments [57, 58]. A schematic of the experimental setup is shown in Fig. 2.6. In these experiments, charge carriers are generated in the sample by photoexcitation. Two parallel metal electrodes, which have a voltage applied between them, are contacted to the sample. In the case of a positive applied voltage at the front electrode, the electrons are discharged immediately. The holes, which in the ideal case consist of a δ-shaped sheet, then drift from the front electrode to the back electrode and the current at the back electrode is recorded. In ordered materials, a sharp signal is recorded indicating the arrival of the holes. In contrast, in disordered organic semiconductors, due to the dispersive transport, the step in the transients indicating the arrival of the holes at the back electrode broadens significantly. The transit time can be used to estimate the charge mobility using the following relationship:

$$\mu = \frac{d^2}{t_\tau V} \tag{2.25}$$

For Eqn. 2.25 to hold true, the time duration of the optical excitation and the characteristic time constant RC of the circuit must be short compared to the transit time

2.2 Carbon Nanotubes

2.2.1 Introduction

Since their discovery by Iijima in 1991, carbon nanotubes have been the focus of considerable research attention [59]. They are long, cylindrical cage-like structures of carbon atoms and exhibit remarkable mechanical and electrical properties which are the consequences of their symmetric structure [60, 61]. Results have shown that carbon nanotubes display an extremely high elastic modulus, greater than 1 TPa, and strengths exceeding the strongest steel by a factor of 10-100 at a fraction of the weight [62]. Next to these mechanical and electrical properties, carbon nanotubes have an extraordinary thermal conductivity more than twice that of diamond, are stable up to 2800°C in vacuum, and have an exceptionally high electric-current-carrying capacity [62]. Due to these properties, carbon nanotubes are thought to be ideal for a wide variety of current and potential applications. Some of these include their use in structural reinforcement, in transistors [63] or as probes in scanning probe microscopy [64], but many more applications, such as optoelectronic devices as well as other mechanical, chemical and electronic applications, are considered viable.

This section will provide a short introduction to carbon nanotubes and a summary of the most important aspects relevant to this work, based on the book by Reich et al. [65].

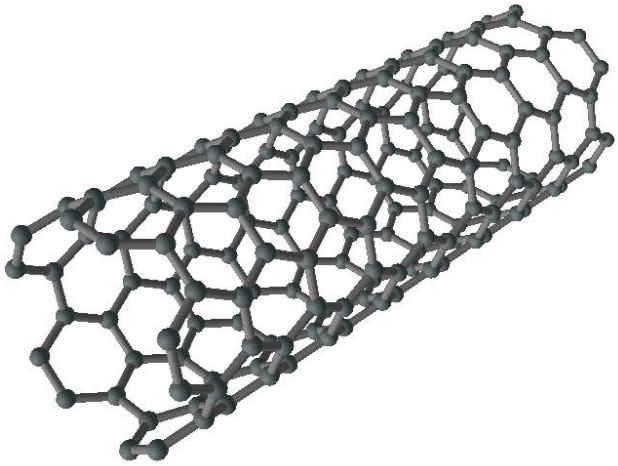

Figure 2.7: Structure of a (5,5) carbon nanotube.

2.2.2 Structure

A single-walled carbon nanotube (SWNT) can be considered as a single graphite layer rolled up into a hollow cylinder [65]. If the nanotube consists of several graphite layers which are held together by van der Waals bonding, it is referred to as a multi-walled carbon nanotube (MWNT). SWNTs typically have diameters in the range of 0.4-2.0 nm [66].

Due to their similarity to graphene, carbon nanotubes can be defined according to their graphene lattice vector. Two vectors $\mathbf{a}_1$ and $\mathbf{a}_2$, each with a length of 2.461 $\mathring{A}$, span the unit cell and form an angle of 60°. The unit cell contains two carbon atoms at the positions $\frac{1}{3}(\mathbf{a}_1 + \mathbf{a}_2)$ and $\frac{2}{3}(\mathbf{a}_1 + \mathbf{a}_2)$. A nanotube is then characterized by the chiral vector $\mathbf{c} = n_1\mathbf{a}_1 + n_2\mathbf{a}_2$, which becomes the circumference of the carbon nanotube. Based on this method it can be uniquely labeled as (n_1, n_2). Fig. 2.8 shows an example of this idea.

The chiral angle of a nanotube is defined as the angle between $\mathbf{a_1}$ and $\mathbf{c}$ and is given by

$$\cos\theta = \frac{\mathbf{a_1} \cdot \mathbf{c}}{|\mathbf{a_1}||\mathbf{c}|} = \frac{n + m/2}{\sqrt{n^2 + nm + m^2}}. \tag{2.26}$$

Due to the six-fold rotational symmetry of graphene, for any chiral vector an equivalent vector with $\theta \leq 60°$ can be found. Thus, one can restrict itself to the cases $n_1 \geq n_2 \geq 0$ or $0° \leq \theta \leq 30°$. Nanotubes are then categorized as either chiral or achiral tubes. Achiral

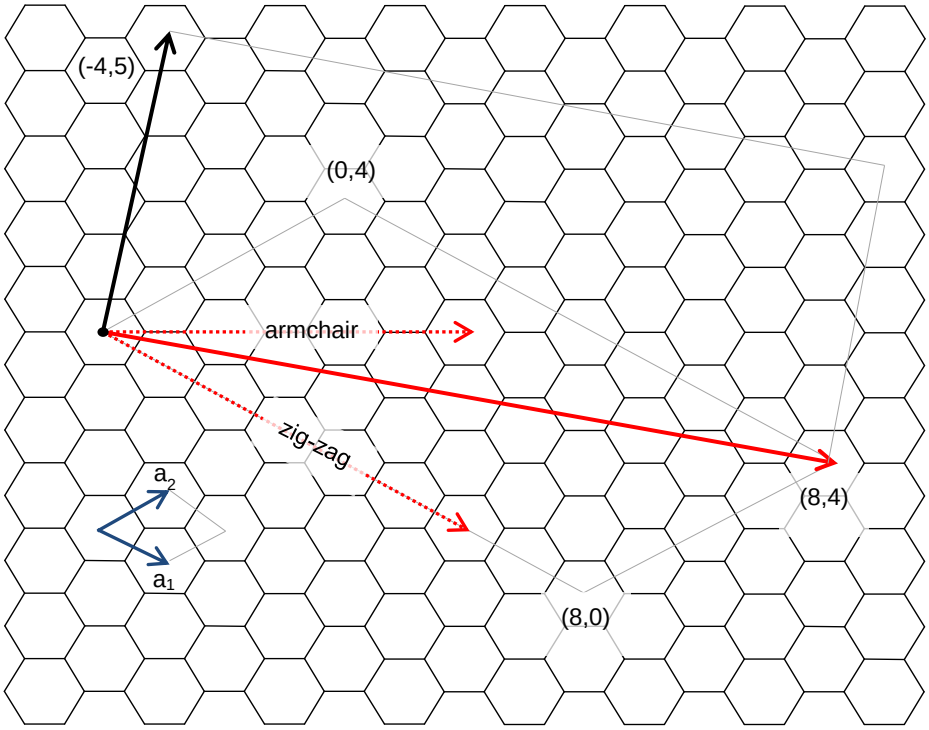

Figure 2.8: Graphene honeycomb lattice. After [65].

tubes are made up of zig-zag tubes which are of the type (n,0), and of armchair tubes which are of the type (n, n). All other tubes are categorized as chiral.

Using this characterization, the diameter of a nanotube is given by

$$d = \frac{|\mathbf{c}|}{\pi} = \frac{a_0}{\pi}\sqrt{n_1^2 + n_1 n_2 + n_2^2} \tag{2.27}$$

where a_0 is the length of the unit vector [65].

2.2.3 Electronic Properties

Two different bonds can be found in carbon nanotubes [65]. σ bonds form the hexagonal network along the cylinder wall. By contrast, π bonds are formed by the p_z orbitals, which are perpendicular to the graphene plane and are responsible for the weak van-der-Waals interaction between different carbon nanotubes. The p_z electrons can be treated independently from the σ electrons and are responsible for the electronic properties of carbon nanotubes.

While most carbon nanotubes are semiconducting, about a third are metallic [65]. The electrical properties are given by their structure. Armchair carbon nanotubes, which have an (n,n) index, are truly metallic. On the other hand, carbon nanotubes for which n - m is a multiple of 3 are actually semiconducting and have a very small band gap. All other types are moderate semiconductors. However, adjustments to this rule need to be made for small diameter carbon nanotubes due to the trigonal warping effect [67, 68].

2.2.4 Optical Properties

Optical Absorption

Due to their one-dimensional nature, carbon nanotubes show strongly structured optical spectra [65]. However, these spectra were not observed for a decade until methods to isolate single tubes and avoid bundling effects were established. The density of states (DOS) of such one-dimensional systems exhibit sharp discontinuous spikes, as shown in Fig. 2.9 [65], called Van Hove singularities. Due to the features of the DOS, carbon nanotubes have very narrow optical transitions, which result from the electronic transitions from the v_1 to the c_1 (E_{11}) and the v_2 to the c_2 E_{22}. The exact structure of the carbon nanotubes defines the energy levels of the Van Hove singularities.

Kataura Plot

A plot displaying the absorption energy for different (n,m) indices based on a theoretical model was first published by Kataura in 1999 to relate experimental findings of absorption of carbon nanotubes to their structure [69]. Since the difference between theoretical predictions and experimental findings was significant, the model was further improved by Popov et al. in 2004 using an extended tight-binding model [70]. In 2002, Bachilo proposed an empirical model, which was later refined by Weisman and Bachilo and is shown in Fig. 2.10 [71, 72].

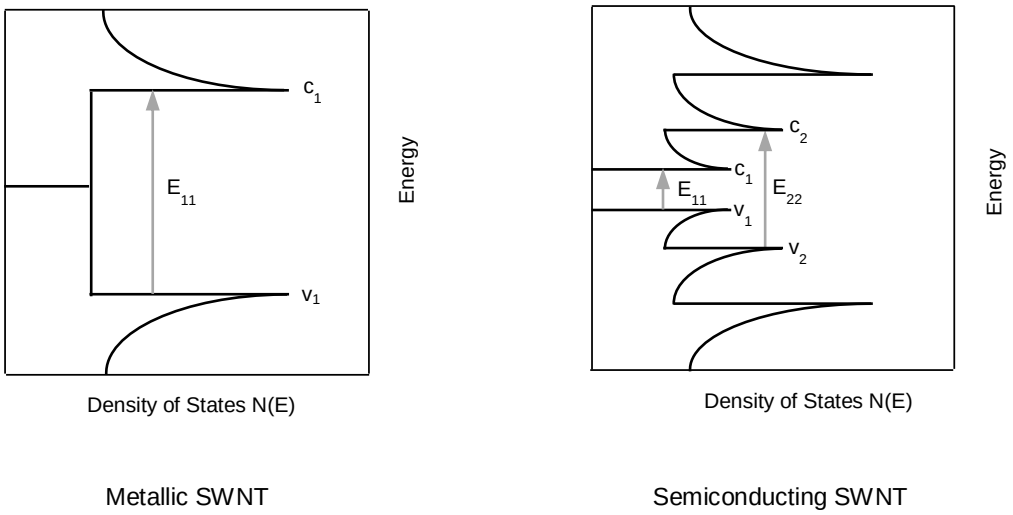

Figure 2.9: Schematic of the linear density of structure plot of metallic and semiconducting carbon nanotubes.

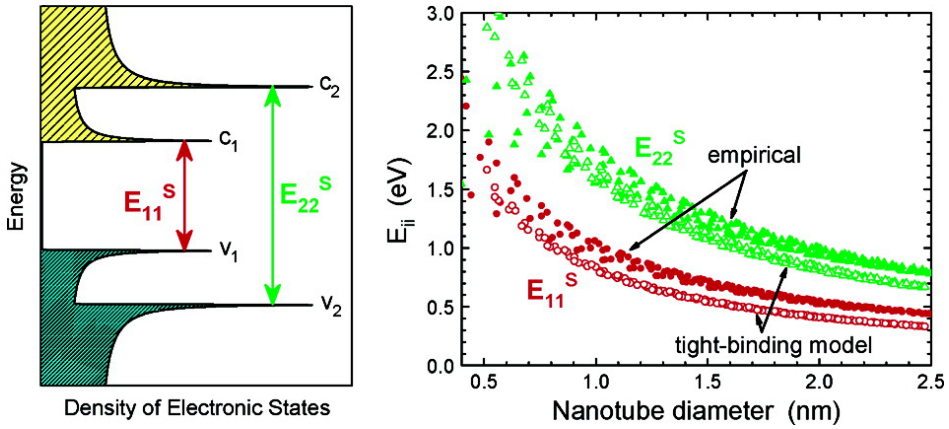

Figure 2.10: Left: Schematic of the density of states plot for a semiconducting SWCNT. Right: Comparison between values of optical transition energies for semiconducting SWNT determined by the tight-binding model (open symbols) and experimentally found by Weisman and Bachilo in 2003 (solid symbols). Reprinted with permission from R. Bruce Weisman and and Sergei M. Bachilo Dependence of Optical Transition Energies on Structure for Single-Walled Carbon Nanotubes in Aqueous Suspension: An Empirical Kataura Plot. *Nano Letters*, **3 (9)**:1235–1238, 2003. [72]. Copyright 2003 American Chemical Society.

Route to Practical Applications

In practical applications, photoluminescence (PL) measurements can be used to determine the carbon nanotube structure. To do this, the carbon nanotubes are first isolated using a chemical agent to avoid effects arising from bundled carbon nanotubes. Subsequently, they are excited with a range of different excitation wavelengths while at the same time the photoluminescence of the sample is measured. The resulting photoluminescence excitation/emission (PLE) map shows the E_{11} and E_{22} peaks of the carbon nanotubes which are then used to identify the (n,m) indices [72].

To make use of the semiconducting properties of carbon nanotubes in practical applications, a method for the separation of metallic and semiconducting tubes needs to be delevoped. While progress has been made over the last two decades, this problem remains outstanding [73].

2.3 Photovoltaic Cells

2.3.1 Introduction

A photovoltaic cell, or solar cell, is defined as a device that converts solar energy into electricity. The first solid-state solar cell was built in 1883 by Charles Fritts using selenium with a very thin layer of gold [74]. Since then, many different types of solar cells have been built with silicon-based solar cells being the most common one. However, alternative approaches based on organic materials have seen an increasing interest in the last decades.

Solar cells produce electricity based on the photovoltaic effect [75]. First, light which is incident on the solar cell is absorbed by the materials that form a junction generating bound or free charge carriers. Then, separation of the photo-generated charge carriers occurs before they are collected at the terminals of the junction. A vast amount of literature on the theory of solar cells is available nowadays [75–77]. Thus, in this chapter, only a short introduction on the general theory of a solar cell based on these sources will be given. This will be followed

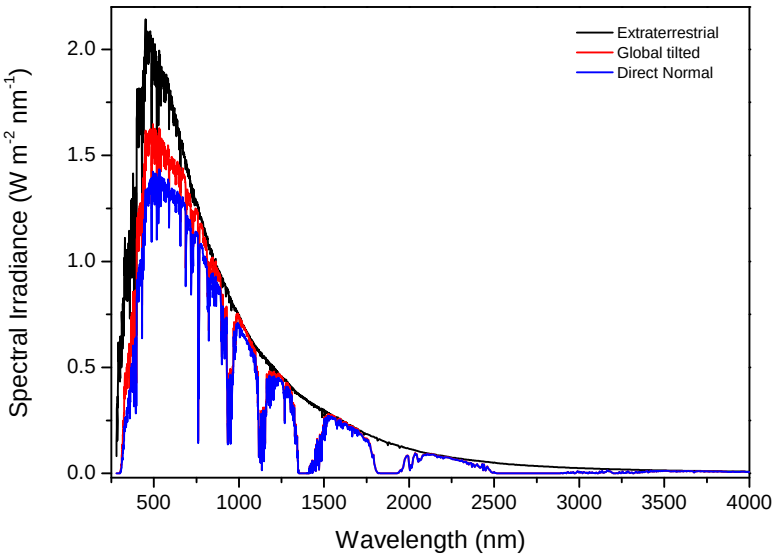

Figure 2.11: AM0 (extraterrestrial) and AM1.5 (global tilted and direct normal) American Society for Testing and Materials (ASTM) reference solar spectra used for characterisation of solar cells [78].

by a more detailed discussion of organic and dye-sensitized solar cells.

2.3.2 Light Absorption and Photocurrent Generation

The photocurrent generated by a solar cell at short-circuit is determined by the incident solar spectrum and the quantum efficiency of the device. The exact solar spectrum depends on time and location, hence a standardised spectrum is usually used. Fig. 2.11 shows the solar spectrum Air Mass 1.5 (AM1.5) as determined by the American Society for Testing and Materials. This solar spectrum corresponds to 1.5 atmosphere thickness giving a good estimate for the average mid-latitudes over the course of the year in the major areas where solar cells are employed. Hence, it is commonly used for device characterizations under laboratory conditions to allow for easier comparability of different devices.

The external quantum efficiency (EQE) of a device is defined as the probability that an incident photon is converted into electric current. The photocurrent at short-circuit is then given by

$$I_{sc} = q \int b_s(E) EQE(E) dE \tag{2.28}$$

where q is the electronic charge, b_s is the photon flux density of the solar spectrum, and E is the energy of the photon [76]. The internal quantum efficiency (IQE) is a second metric commonly used. It is defined as the probability that an absorbed photon is converted into electric current and is calculated from the EQE and the absorption spectrum of the solar cell.

2.3.3 Current-Voltage Characteristic

When a load is applied to a solar cell, a potential difference is generated between the terminals of the junction. This potential difference generates a current, called the dark current, which flows in the opposite direction of the photocurrent. Since solar cells typically have the same behaviour as an ideal diode in the dark, the dark-current density is given by the dark-current density of an ideal diode:

$$I_{dark} = I_0(e^{qV/k_bT} - 1) \tag{2.29}$$

where I_0 is the dark saturation current, i.e. the leakage current density in the absence of light, V is the applied voltage, k_b is Boltzmann's constant and T is the temperature [76].

In the previous equation it was assumed that the behaviour of the solar cell can be perfectly matched by an ideal diode. However, this is not always the case. To quantify the deviation, the ideality factor n is introduced which describes how closely the behaviour is matched by that of an ideal diode. The dark current density is then given by

$$I_{dark} = I_0(e^{qV/nk_bT} - 1). \tag{2.30}$$

The ideality factor typically varies between 1 and 2, with 1 being the case for an ideal

diode. For classical p-n junction solar cells a value greater than 1 for n is explained by recombination of electrons in trapping sites with free electron holes [79, 80]. A value of 2 is reached for n once recombination is fully trap-assisted. Deviations from the ideal diode in organic photovoltaics have been explained by trap-assisted recombination as well [81–83]. More recently though, it was explained by deeply trapped carriers in the transport-dominating constituent of the organic blend [84].

A solar cell can be considered as a device which conducts similar to a diode in the dark and generates a photovoltage once light is incident upon the device [76]. Thus, to approximate the overall current-voltage characteristic of the solar cell, the short-circuit current and the dark current are combined:

$$I = I_{sc} - I_0(e^{qV/nk_bT} - 1) \tag{2.31}$$

When the contacts of the solar are isolated, the potential difference reaches its maximum and is called the open-circuit voltage V_{oc}. It is given by

$$V_{oc} = \frac{nk_bT}{q} \ln\left(\frac{I_{sc}}{I_0} + 1\right) \tag{2.32}$$

2.3.4 Equivalent Circuit of a Photovoltaic Cell

Solar cells can be modeled by an electrically equivalent circuit allowing for a better understanding of the electronic behaviour. For an ideal solar cell, this is done by modeling a current source in parallel with a diode, as seen in Fig. 2.12.

In practice, however, power losses occur through leakage currents around the sides of the device and resistance of the contacts [76]. In the equivalent circuit of a photovoltaic cell, this is identical to a series resistance and a parallel resistance, called shunt resistance. Fig. 2.13 shows the equivalent circuit of a solar cell which includes both of these resistances.

Taking series resistance R_s and shunt resistance R_{sh} into account, eq. 2.31 changes to

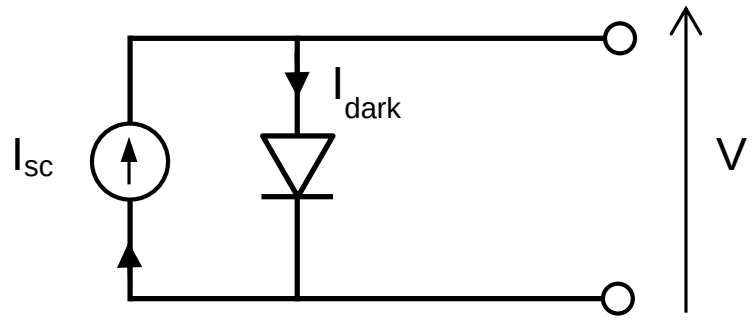

Figure 2.12: Equivalent circuit of an ideal solar cell.

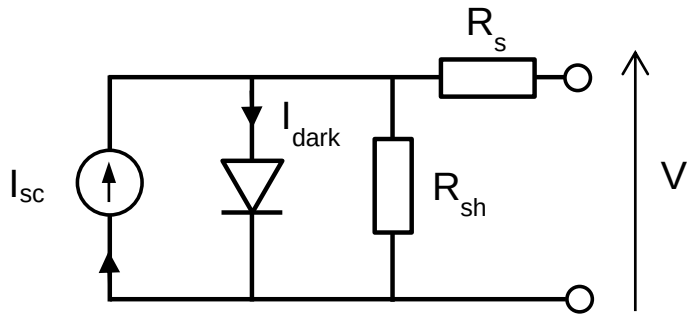

Figure 2.13: Equivalent circuit of a real solar cell which includes series and shunt resistance.

$$I = I_{sc} - I_0(e^{q(V+IR_s)/nk_bT} - 1) - \frac{V + IR_s}{R_{sh}}. \tag{2.33}$$

A minimal series resistance and a maximal shunt resistance is therefore desired for optimal device performance.

2.3.5 Power-Conversion Efficiency

The electrical power output of a solar cell is given by the product of current and voltage:

$$P = I \cdot V \tag{2.34}$$

At one point, defined as the maximum power point, on the current-voltage characteristic curve the electrical power reaches a maximum:

$$P_{max} = V_{mpp} \cdot I_{mpp} \tag{2.35}$$

where V_{mpp} and I_{mpp} are the voltage and the current at the maximum power point as shown in Fig. 2.14.

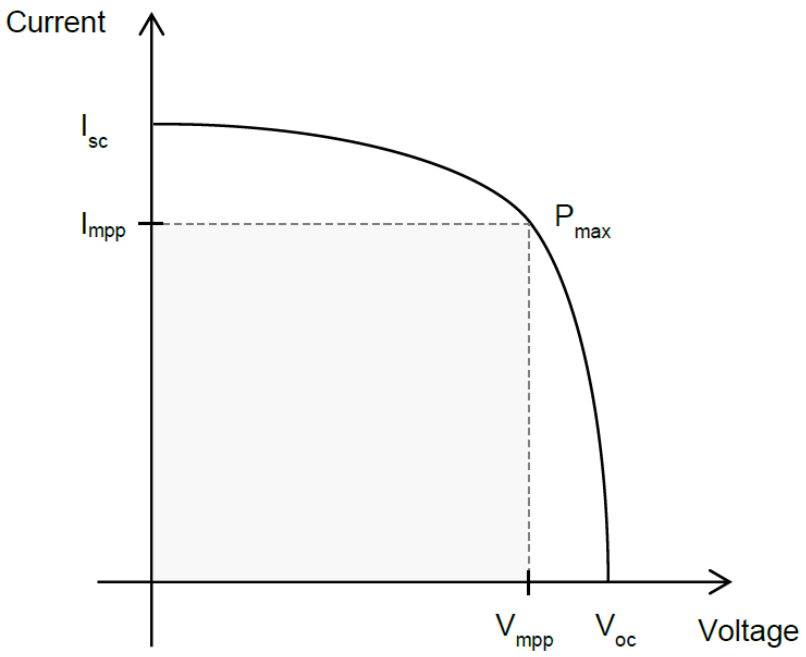

Figure 2.14: Current-voltage characteristics of a solar cell.

The power-conversion efficiency η of a photovoltaic device is then given by the ratio of the maximum electrical power output P_{max} to the incident power P_{in}:

$$\eta = \frac{P_{max}}{P_{in}} = \frac{V_{mpp} \cdot I_{mpp}}{P_{in}} \tag{2.36}$$

To relate the power-conversion efficiency to the open-circuit voltage and short-circuit current, the fill factor FF is introduced. It is defined as the ratio of the maximum electrical power output to the product of the open-circuit voltage and short-circuit current:

$$FF = \frac{V_{mpp} \cdot I_{mpp}}{J_{sc} \cdot V_{oc}} \tag{2.37}$$

It is commonly described as measuring the "squareness" of the current-voltage characteristics. The fill factor is influenced by series and shunt resistance. A high fill factor indicates a low series resistance and a high shunt resistance whereas for low fill factors the opposite is the case.

Using the definition of the fill factor FF, the power-conversion efficiency can be related to the open-circuit voltage V_{oc} and the short-circuit current I_{sc} by

$$\eta = \frac{P_{max}}{P_{in}} = \frac{V_{oc} \cdot I_{sc} \cdot FF}{P_{in}} \tag{2.38}$$

2.3.6 Efficiency Limitations

To improve the efficiency of photovoltaic devices, it is important to understand the maximum achievable limits and the reasons for the current deviation from this limit. The conversion of light from the sun into electricity is limited by the Carnot efficiency limit for conversion of heat energy. The band gap of the absorbing material puts another limit on the power-conversion efficiency. Photons with energies below the band gap are mostly not absorbed and if they are absorbed, their energy is often converted into heat. On the other hand, photons with an energy above the band gap thermalise to the band edge and convert the excess energy into heat. Only the remaining energy is converted into electric current. This effect can be partly compensated by using multiple absorbers with different band gaps. As described in the introduction, the maximum theoretical power-conversion efficiency for single-junction solar cells is just over 30% given by the Shockley-Queisser limit [13].

For solar cells where the absorption of a photon produces an exciton and not a free electron-hole pair, the Coulomb binding energy on the order of 0.3 to 1.2 eV [85–87] further limits the maximum attainable power-conversion efficiency. For donor-acceptor heterojunction solar cells with a typical driving force for charge transfer ΔG_{CT} in the range 0.3 to 0.5 eV the maximum efficiency decreases to 27% and 22%, respectively [88].

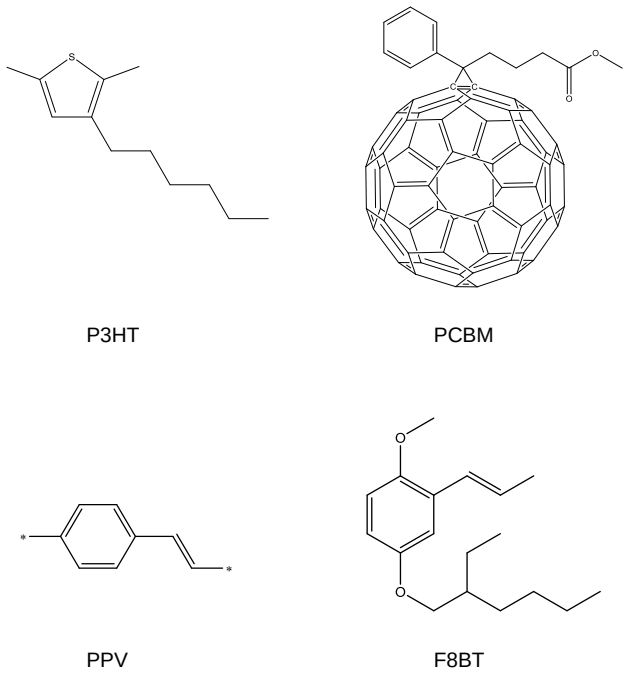

Figure 2.15: Chemical structures of commonly employed organic materials.

2.4 Organic Photovoltaics

2.4.1 Introduction

Organic photovoltaics (OPV), sometimes alternatively called excitonic photovoltaics, is the class of solar cells that uses π-conjugated organic molecules, oligomers and polymers. While reports of organic photovoltaics date back as far as 1959 [89], efficiencies had stayed well below 1% until 1985, when the use of a bilayer structure in OPVs was first reported by Tang et al. [90]. Since then, and especially due to rapid improvements over the last couple of years, power-conversion efficiencies have increased to values exceeding 8% [91]. Some of the commonly employed materials include poly(3-hexylthiophene) (P3HT), phenyl-C61-butyric acid methyl ester (PCBM), poly(p-phenylene vinylene) (PPV), and poly[(9,9-di-n-octylfluorenyl-2,7-diyl)-alt-(benzo[2,1,3]thiadiazol-4,8-diyl)] (F8BT). Fig. 2.15 shows the chemical structures of these materials.

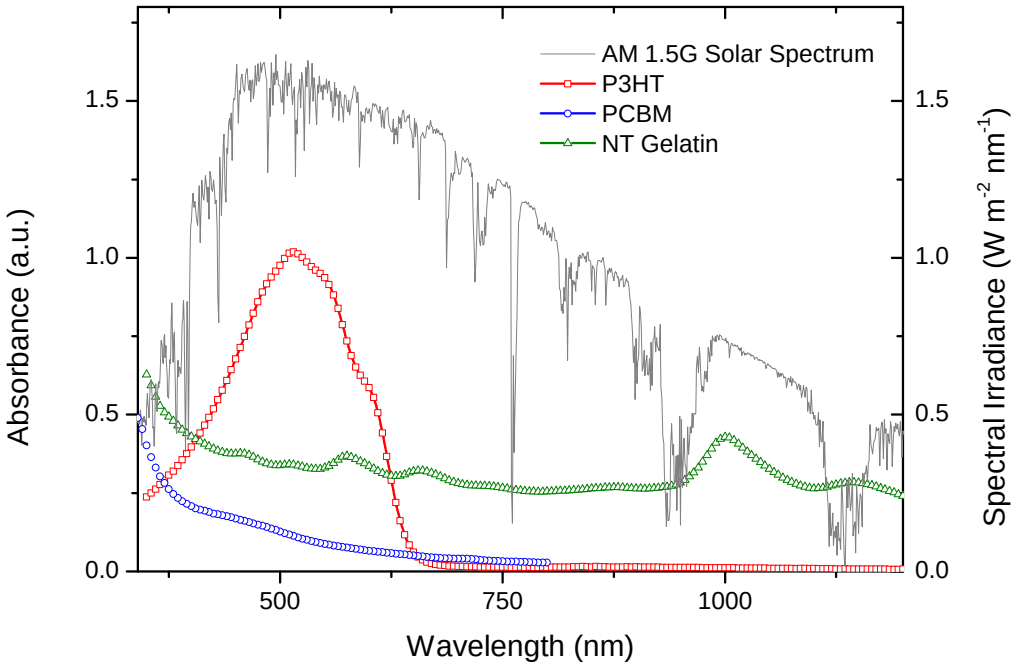

Figure 2.16: UV-VIS absorption spectra of organic materials P3HT (red squares), PCBM (blue circles), and NT gelatin (green triangles) on quartz substrates which were used in this thesis as detailed in Chapter 6. Additional, the AM1.5G solar spectrum is shown as a comparison. Measurements were performed by Sam D. Stranks and Christopher Menelaou.

2.4.2 Light Absorption

OPVs commonly have a high absorption coefficient [92]. Thus, thicknesses of only a few hundred nanometers are required for the active layer to absorb most of the light at the absorption peak. In contrast, energy gaps tend to be large and absorption spectra tend to be relatively narrow resulting in the absorption of only a small fraction of the solar spectrum [92]. In addition, the absorption peak of most polymers is at smaller wavelengths in comparison to the solar spectrum. To broaden the absorbed spectrum, two strategies, the use of low bandgap polymers and the extension of existing polymers with conjugated chromophores have been used [93–95]. In Fig. 2.16, the UV-VIS absorption spectra of organic materials used in this thesis for the application in OPVs, namely P3HT, PCBM and carbon nanotubes, are shown.

2.4.3 Charge Dissociation and Recombination

One of the main differences between organic and inorganic photovoltaics is that in inorganic solar cells the charge carriers are generated in the bulk of the material and are not tightly bound [96]. In contrast, in solar cells employing organic material, due to the low dielectric constant on the order of 3-5 and due to weak non-covalent electronic interaction between organic molecules, the charge carriers are tightly bound in the form of an exciton. Given an exciton radius of approximately 1 nm and a binding energy of approximately 250 meV, an electric field exceeding 10^6 V cm^{-1} would be required to separate the charges [96–98]. As a result, the charge-separation yield tends to be low in pristine materials and dissociation of most excitons into electron and hole occurs at an interface such as the electrodes or the interface between a donor and an acceptor material. However, for this process to be efficient, the interface needs to have a large enough driving force as well as a close enough distance to the exciton in order for it to reach the interface before recombination occurs.

Due to the lack of such an interface, organic photovoltaics using a single active layer achieved power-conversion efficiencies of only 0.1% [92]. Accordingly, the introduction of a bilayer OPV improved power-conversion efficiencies tremendously [90]. However, to reach this interface, most excitons still need to diffuse through the material [99] and exciton lifetimes in organic materials are on the order of 1 ns with a diffusion coefficient on the order of 10^{-3} cm^{-2}/s [100, 101]. Using the definition of the exciton diffusion length,

$$L_{ex} = \sqrt{D_{ex}\tau_{ex}} \tag{2.39}$$

a value of only approximately 10 nm is calculated. In contrast, the absorption depth of commonly used organic materials is on the order of a few hundred nanometers. A significant number of excitons in a bilayer OPV can therefore not reach the interface before recombination occurs requiring a trade-off in the film thickness between absorption and recombination.

A second method is to create a bulk heterojunction [102–105]. In this method, two materials are mixed, as shown in Fig. 2.17, each forming a self-assembled continuous in-

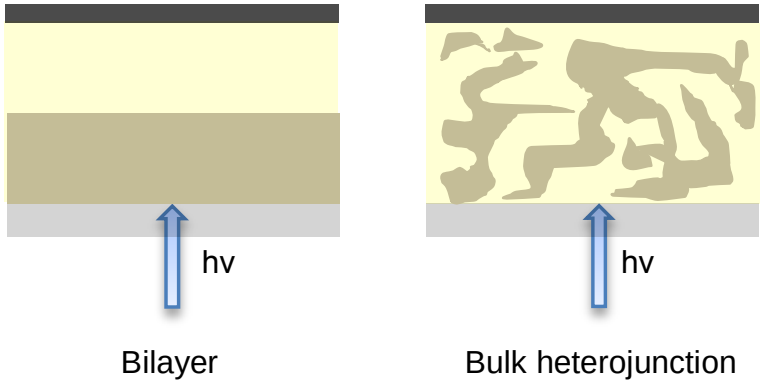

Figure 2.17: Left: Sketch of a bilayer organic photovoltaic cell. Right: Sketch of a bulk heterojunction organic photovoltaic cell.

terpenetrating network with the effect of reducing the average distance an exciton needs to diffuse until reaching an interface. This method allows for thicker film thickness and thus higher absorption factors while at the same time achieving good charge-separation efficiencies.

The exact mechanism for charge dissociation and recombination in OPVs is, despite intense research, still under debate. After excitation of an electron from the ground state (GS) into an excited state, several pathways from the excited state into a charge-separated (CS) state are possible, as schematically shown in Fig. 2.18 [106–109]. An exciton can be quenched forming a hot charge-transfer (CT) state and relaxing very quickly on a timescale of 100 fs to its electronic and vibrational ground level (CT_1) [109]. Following relaxation and on a timescale of a few nanoseconds, hopping of the charge pair causes it to either become spatially separated with a rate k_{CS} or results in geminate recombination with rate k_f.

Alternatively, charges are separated from hot charge-transfer states with rate k^*_{CS} before relaxation can occur [109]. The mechanism of separation has been proposed to be driven by the excess energy of the exciton quenching being converted into kinetic energy of electron and hole [110]. In another explanation, the greater separation of electrons and holes in the wave function of the charge-transfer state causes separated charges [107]. Since the thermal relaxation of the hot charge-transfer state occurs on a timescale of a few hundred nanoseconds, the charge separation needs to occur faster than this.

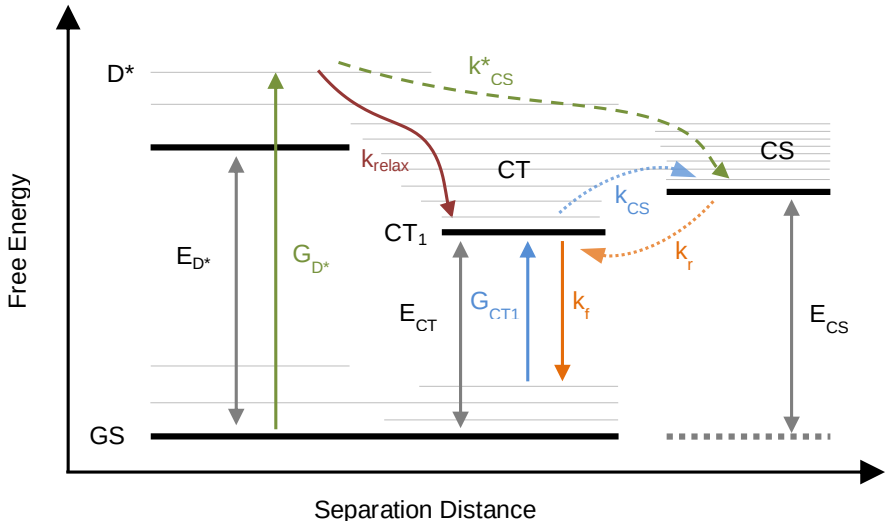

Figure 2.18: Energy states at a donor/acceptor interface [106]. An absorbed photon with energy larger than E_{D*} excites an electron from the ground-state (GS) into the excited donor state D* at a rate G_{D*}. Transfer from the excited state into the charge-separated (CS) state can occur by either bypassing the lowest charge-transfer state (CT1) with a rate k^*_{CS} or first relaxing into CT_1 with rate k_{relax}. CT_1 can either dissociate at rate k_{CS} or decay radiatively at rate k_f. Inversely, population of CT_1 from CS can occur at a rate k_r.

For charge recombination, three processes are relevant [109]. In the first process, geminate recombination, an electron and hole that were both generated by the dissociation of the same exciton recombine [111, 112]. It is a monomolecular loss and therefore depends linearly on the illumination intensity. The second case is the recombination of two free charges. The recombination rate depends on the charge density in the OPV and has been experimentally observed to be on the order of 2 with respect to the charge density [113, 114]. The process therefore has a nonlinear dependence on the illumination intensity. In the third process, a carrier in an immobile trap state recombines with a free carrier causing trap-assisted recombination [109]. This process can have density-dependent or density-independent characteristics.

2.5 Dye-Sensitized Solar Cells

2.5.1 Introduction

Dye-sensitized solar cells (DSSC) are considered to be a promising alternative to conventional silicon-based photovoltaic systems due to their low production cost and low construction energy [9]. Since their invention in 1990, DSSC have gained much attention. Originally having a power-conversion efficiency of approximately 7%, subsequent improvements over the years have resulted in values over 12% [9, 115]. Further improvements in the near future are expected to increase the efficiency beyond 15% [6]. These advances have made the goal of reaching grid parity versus conventional fossil fuel more achievable.

2.5.2 Architecture and Operation Principles

The most studied dye-sensitized solar cell consists of a mesoporous metal-oxide electrode, in most cases TiO_2, which is coated on a transparent conducting glass (fluorine-doped tin oxide, SnO2:F). The thickness of the electrode lies at about 10 μm and is sensitized with a monolayer of dye molecules [32]. This technique highly enhances the surface area per micrometer thickness which ensures high light absorption. The pores are filled with an iodide/triiodide-based electrolyte which is bounded by a platinum counter electrode [9]. Fig. 2.19 shows a schematic of the architecture.

In contrast to conventional semiconductor devices, dye-sensitized cells separate the function of light absorption from charge carrier transport. Fig. 2.20 shows a schematic energy diagram of the process. In the first step, light is absorbed by a dye. Although many different types of dyes can be employed, such as porphyrins [117], pentacene [118], squaraines [119], etc., usually a metallorganic Ruthenium complex is used. The absorption onset of these dyes lies at around 1.72 eV [120]. Two of the most commonly used dyes are cis-RuLL'(SCN)2 (L = 4,4'-dicarboxylic acid-2,2'-bipyridine, L' = 4,4'-dinonyl-2,2'-bipyridine) (Z907) and NaRu(4,4'-bis(5-(hexylthio)thiophen-2-yl)-2,2'-bipyridine)(4-carboxylic acid-4'-carboxylate-

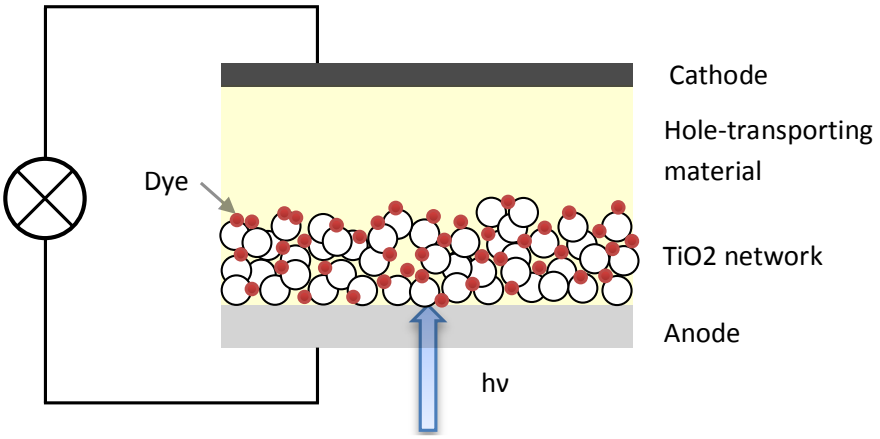

Figure 2.19: Schematic of a dye-sensitized solar cell [116].

2,2'-bipyridine)(NCS)2 (C106) [120, 121]. These exhibit relatively good stability and, hence, tend to be used as workhorses in experiments. However, the molar extinction coefficients of Ruthenium based dyes is relatively low, in the range of 10,000-20,000 $M^{-1}cm^{-1}$ [122]. Additionally, the high cost and limited supply of Ruthenium, which would limit the scale of DSSCs to 19 GW per year, require the search for alternatives [6, 123]. Organic donor-π-acceptor dyes are usually presented as an alternative as they exhibit higher molar extinction coefficients in the range of 50,000-200,000 $M^{-1}cm^{-1}$, but their absorption range tends to be much smaller, on the order of 100-250 nm, in comparison to Ruthenium based dyes [6]. Efforts have also gone into developing dyes that absorb in the near-infrared or infrared region to be used in conjunction with dyes absorbing in the visible region therefore enhancing the light absorption region [124–126].

To increase the low absorption, the dye is sensitized on a mesoporous TiO_2 network. Although TiO_2 is currently the most commonly used material, alternatives such as SnO_2, ZnO, Nb_2O_5 and WO_3 have been employed [127–129]. The TiO_2 particles have an average size of about 20 nm creating a network which highly enhances the surface area per micrometer thickness by a factor of about 1000 and, thus, dramatically increasing the light absorption for a given thickness of the device [9].

Charge separation occurs by the transfer of electrons from the excited states of the dye into the conduction band of the TiO_2. This process occurs over different phases with

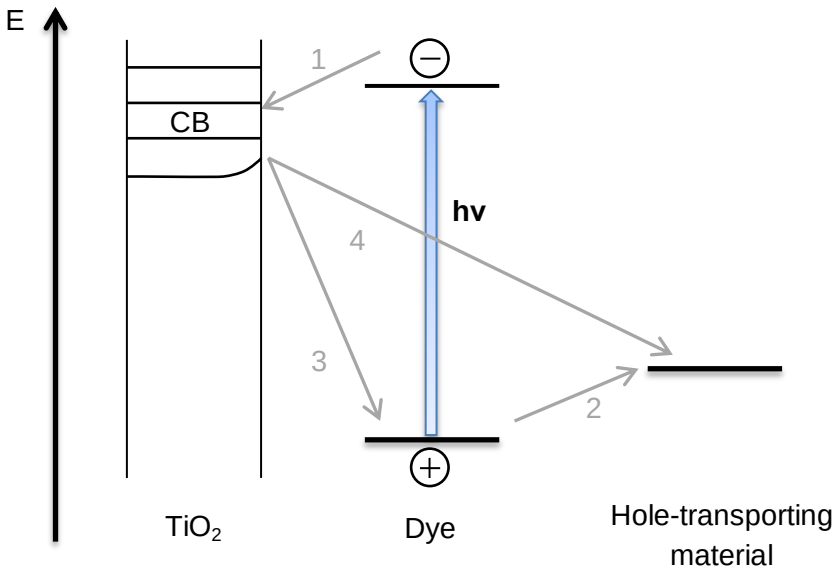

Figure 2.20: Schematic energy diagram of a dye-sensitized solar cell [116]. Light is absorbed in the dye, followed by electron transfer into the conduction band of the TiO_2 (1) and hole transfer to the hole-transporting material (2). The electron is then either transported to the contact or recombines with the hole on the dye (3). Similarly, the hole is either transported to the contact, but can also recombine with the electron in the TiO_2 (4).

the earliest on a scale of 1 picosecond or faster and the slowest on the order of a few nanoseconds [130–134]. The electrons then diffuse through the TiO_2 film to the anode.

The iodide redox couple regenerates the dye molecules by hole transfer which is then transported through the electrolyte until it reaches the platinum counter electrode. The regeneration process occurs in two steps [135]. In the first step, an I_2^- is created,

$$D^+ + 2I^- \rightarrow D + I_2^- \tag{2.40}$$

where D is the dye, and I is the electrolyte. In the second step, the intermediate product is dismutated:

$$2I_2^- \rightarrow I_3^- + I^- \tag{2.41}$$

The loss-in-potential incurred by the first process is given by the difference between the

Z907

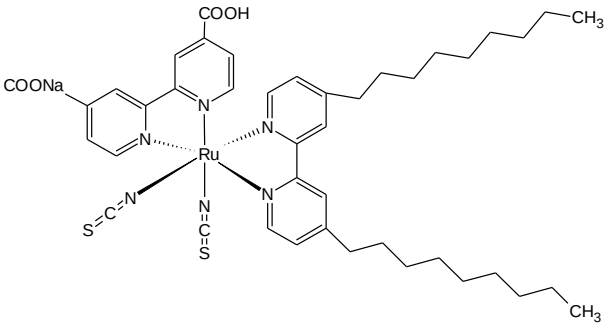

C106

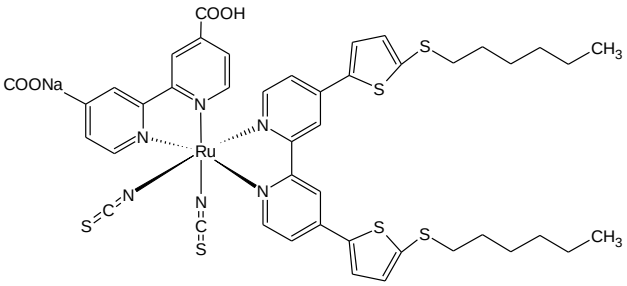

Figure 2.21: Two dyes used in dye-sensitized solar cells. Top: cis-RuLL'(SCN)2 (L = 4,4'-dicarboxylic acid-2,2'-bipyridine, L' = 4,4'-dinonyl-2,2'-bipyridine) (Z907) [120]. Bottom: NaRu(4,4'-bis(5-(hexylthio)thiophen-2-yl)-2,2'-bipyridine)(4-carboxylic acid-4'-carboxylate-2,2'-bipyridine)(NCS)2 (C106) [121].

HOMO level of the dye and the I_2^-/I^- potential, whereas the loss-in-potential by the second process is given by the difference between the I_2^-/I^- and the I_3^-/I^- potential [135].

These processes are in competition with the charge recombination processes between the electrons in the TiO_2 and the oxidized dye molecules, as well as the electrons in the TiO_2 and the holes in the hole-transporting material (HTM). The first recombination process occurs on the order of a few hundred microseconds [136], whereas recombination between electrons in the TiO_2 and the holes in the liquid electrolyte occur on the micro- to millisecond timescale [137–139]. This relatively long timescale is caused by the two-step recombination process since the intermediate I_2^- needs to find another I_2^- before it can recombine with an electron in the TiO_2.

2.5.3 Solid-state Hole-Transporting Materials

One of the main concerns over liquid-electrolyte based dye-sensitized solar cells is the solvent leakage and corrosion from the iodide/triiodide redox couple [140, 141]. To overcome these, several attempts have been made to substitute the liquid-electrolyte with either cobalt complex redox mediators or solid-state hole-transporting materials [6, 142–145]. The first and still most successful organic solid-state hole transporting-material is 2,2',7,7'-tetrakis(N,N-di-p-methoxyphenylamine)-9,9'-spirobifluorene (spiro-OMeTAD, see Fig. 2.22) [16]. In contrast to liquid-electrolyte hole transporters, hole injection into the solid-state hole transporter has been shown to occur over a broad time range from picoseconds to nanoseconds [146], several orders of magnitude faster than the competing recombination process of dye cation and electron in the TiO_2 which, as previously discussed, occurs on the micro- to millisecond timescale [137–139].

In the beginning, the efficiencies of DSSCs with spiro-OMeTAD failed to exceed values of 1% [16]. However, further research led to improvements of the efficiency with a maximum achieved value of 7.2% [17], but the efficiencies of 12% for dye-sensitized solar cells employing cobalt complex redox mediators have not been reached to date [115]. The difference in efficiency is believed to be mainly due to the low light absorption of solid-state DSSCs.

Optimized devices have a thickness of only 2 μm which is much less than what is required to absorb the majority of the incoming light [147]. For Ruthenium-based dyes a device thickness of about 10 μm is necessary to reach an absorption of 90% over a wide spectral region [116]. The optimized thickness is a trade-off between light absorption and other limiting factors. Lower charge collection and an incomplete filling of the pores have been suggested to be those factors [15, 116, 148].

The low mobility of spiro-OMeTAD on the order of $10^{-4} cm^2 V^{-1} s^{-1}$ has been proposed to be the cause for lower internal quantum efficiencies [149]. However, attempts to replace spiro-OMeTAD with higher-mobility hole-transporting materials have not resulted in devices with higher power-conversion efficiencies [150–152]. For further efficiency improvements Schmidt-Mende *et al.* compared different hole-transporting materials, namely AV-DM and AV-OM, to spiro-OMeTAD [148]. These hole-transporting materials exhibit higher mobilities which should lead to faster and more efficient charge collection. This is caused by the fact that fewer charges will recombine due to faster transportation of the charges to the electrodes and, thus, thicker cells can be made, which increases the amount of absorbed light [149, 153]. The efficiency of all studied materials, however, stayed below that of spiro-OMeTAD, which is believed to be due to a less complete filling of the mesoporous TiO_2 network compared to spiro-OMeTAD.

The incomplete filling of the mesoporous TiO_2 pores with the hole-transporting material has been proposed to be another factor causing lower performance [15, 148]. For efficient solar cell operation, a high pore-filling fraction (PFF), defined as the fraction of pores in the TiO_2 network that are filled with the hole-transporting material, is required to regenerate the dye by hole transfer to the hole-transporting material. Additionally, a higher pore-filling fraction reduces the percolation path of holes to the cathode and increases the charge collection efficiency. A good understanding of the influence of the pore-filling fraction on both the hole injection into the hole-transporting material and charge collection are therefore important.

In order to do this, the mechanism of film formation needs to be considered. A model

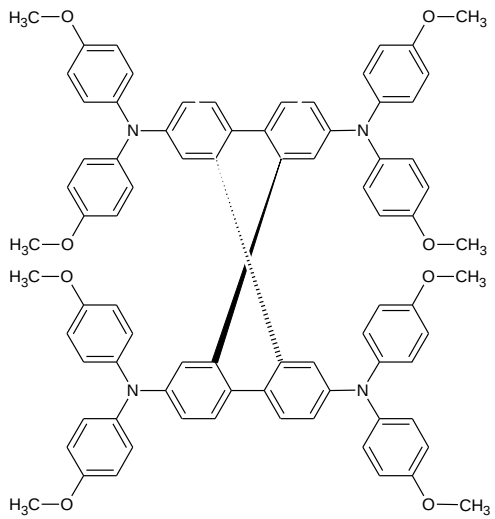

Figure 2.22: Chemical structure of 2,2',7,7'-tetrakis(N,N-di-p-methoxyphenylamine)-9,9'-spirobifluorene (spiro-OMeTAD), the most researched solid-state hole-transporting material for DSSCs.

has been proposed by Snaith *et al.* and is illustrated in Fig. 2.23 [154]. First, a solution with a sufficiently high concentration of the hole-transporting material is deposited on top of the mesoporous TiO_2 network. For optimized devices with a thickness of approximately 2 μm, a solution concentration of about 10%-15% is usually used. The pores are then considered to be wet by the solution and a layer with the excess solution is left on top of the device. In the next step, the device is spin-coated. During this process part of the excess solution is removed leaving a uniform film. The thickness of the film is independent of the original quantity of solution dispensed on the device, but it depends on the viscosity of the material. The film thickness has been measured to be approximately 6.7 μm for spiro-OMeTAD [154]. In another study, a value of 6.9 ± 0.5 μm has been found which is within the experimental error of the previous estimate [155]. While the spin-coating continues, the solvent evaporates from the surface of the excess solution creating a higher concentration in the top layer compared to the concentration in the pores. Diffusion and convection is then believed to drive more of the hole-transporting material from the top layer into the pores. This causes the pore-filling fraction to be much higher than the initial solution concentration [154]. At some point, however, the solution gels and no further increases of the pore-filling fraction are achieved.

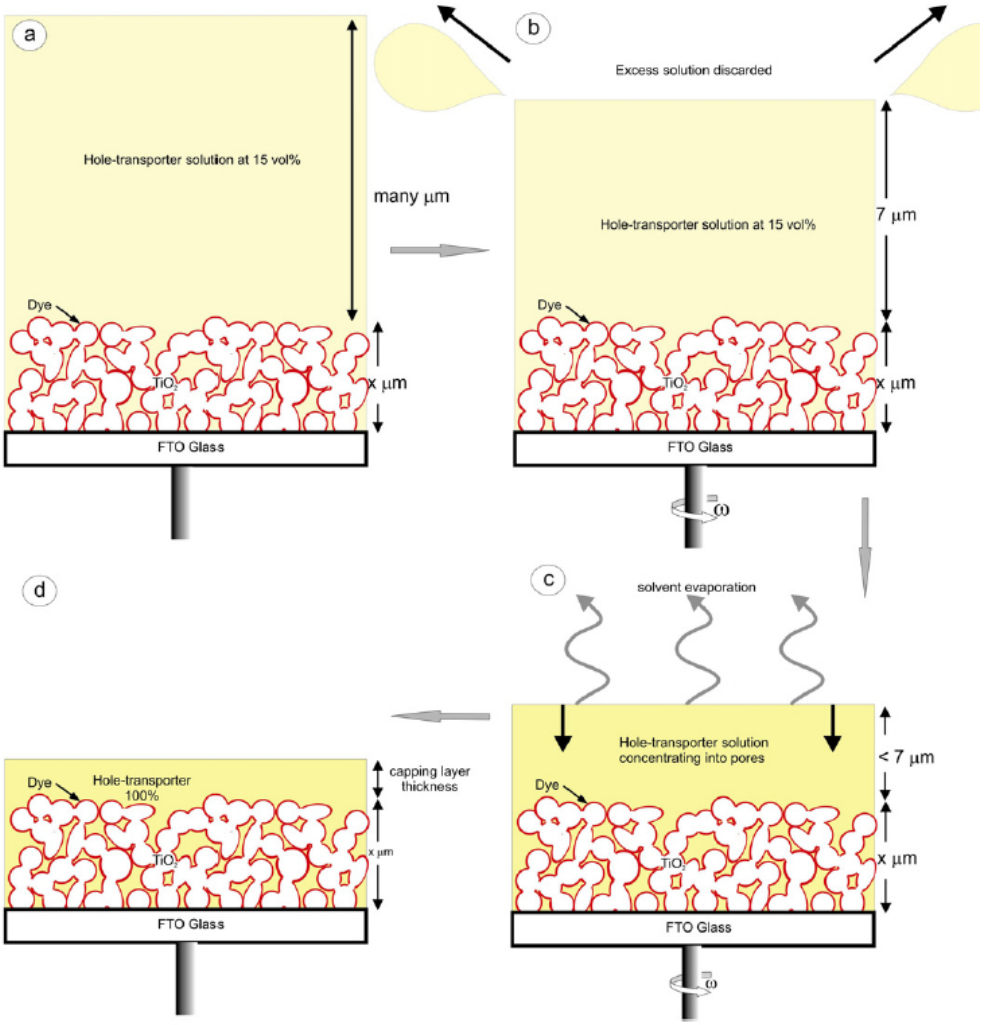

Figure 2.23: Schematic illustration of the pore-filling process of the hole-transporting material during spin-coating. Reproduced with permission from [154].

Further drying of the solvent leaves gaps in the TiO_2. Additionally, any hole-transporting material that has not propagated from the excess solution on top of the device into the pores forms a capping layer. Fig. 2.24 shows an SEM image of a solid-state DSSC where a capping layer (top layer) is clearly visible.

Based on this mechanism, the pore-filling fraction can be quantified. The amount of hole-transporting material in the pores is calculated by adding the concentration in the pores before spin-coating, given by the initial solution concentration c and shown in step a in Fig. 2.23, to the increase in concentration which occurs due to infiltration of HTM into the pores after spin-coating. The latter is estimated by subtracting the amount left on top of the device after spin-coating, i.e. the capping layer as shown in step d in Fig. 2.23, from

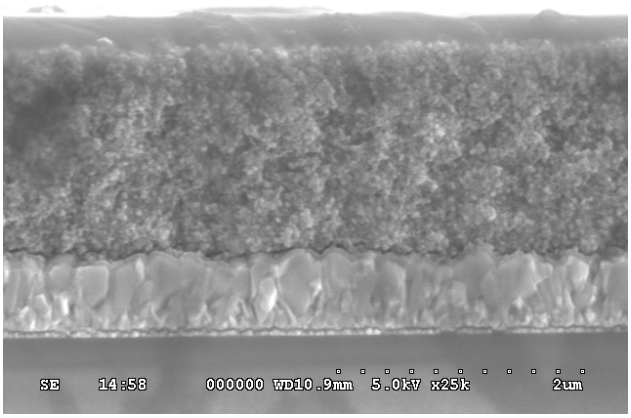

Figure 2.24: SEM image of a solid-state dye-sensitized solar cell with a clearly visible capping layer (top layer) on top of the TiO_2 network.

the initial amount of hole-transporting material on top of the device, i.e the $\sim 7\mu m$ solution layer as shown in step b in Fig. 2.23. This amount is then divided by the volume of the pores in the network. The pore-filling fraction is thus given by

$$PFF = c + \frac{d_{sol}c - d_{cl}}{dp} \tag{2.42}$$

where c is the initial solution concentration, d_{sol} is the thickness of the initial solution after spin-coating, d_{cl} is the capping layer thickness, d is the thickness of TiO_2 network and p is its porosity [154].

Several other techniques have been suggested to quantitatively and qualitatively analyze pore filling. Using photoinduced absorption (PIA) spectroscopy, the uniformity of the pore filling can be measured by comparing the results of the device illuminated from the front to the results of the device illuminated from the back [156]. If the infiltration process is too slow and the solvent evaporates before the hole-transporting material can completely penetrate the material, a density gradient of the hole-transporting material establishes throughout the device resulting in a weaker PIA signal when the device is illuminated from the front than the back. In another technique, the effective refractive index is measured using UV-VIS absorption spectroscopy [155]. The average effective refractive index is determined by measuring the number of observed maxima in the spectral region where none of the

constituent components absorb. It is given by

$$n_{\text{av,eff}} = \frac{N}{2d_{TiO_2}\left(\frac{1}{\lambda_1} - \frac{1}{\lambda_2}\right)} \tag{2.43}$$

where N is the number of observed maxima, λ_1 and λ_2 are the beginning and end wavelength of the spectral region, and d_{TiO_2} is the thickness of the TiO_2 network. The average effective refractive index is then correlated to the pore-filling fraction. Going further, the study estimated that while a 60% pore-filling fraction is required to achieved maximum performance, optimized devices usually have pore-filling fractions of up to 80%. The study also showed that the pore-filling fractions in films with up to 5 μm thickness can achieve 60% and is therefore high enough to not limit the device performance [155].

To achieve maximum performance, two processes, the transfer of holes from the dye to the hole-transporting material and the collection of the holes, need to be maximized. Using transient absorption spectroscopy, the hole-transfer yield for optimized devices employing spiro-OMeTAD has been estimated to be approximately 90-100% [15, 146, 157]. Since these devices have pore-filling fractions of up to 80%, smaller values might be sufficient to reach hole-transfer yields close to unity and the limiting factor for device performance might be caused by charge collection. A good theory on this relationship has not been established yet. To do so is one of the motivations for the work here.

Besides spiro-OMeTAD, significant progress has been made in the recent past with alternative hole-transporting materials such as conjugated polymers. This class of organic semiconductors are considered to be favourable hole-transporting materials due to their low cost and tailorability. Additionally, a polymer can function in two ways in a device. First, it can act as the hole-transporting material regenerating the dye and second, due to its absorption spectrum, as a sensitizer. In the latter process, the absorption of a photon generates an exciton which is subsequently dissociated at the metal-oxide interface and transported to the contacts. However, for a long time, polymer-based hole-transporting materials only reached very poor efficiencies [143, 158–161]. Two main issues are considered responsible

for this. The infiltration of the polymer into a mesoporous network has proven to be difficult [162] and the charge transport within the polymer is believed to be ineffective due to un-oriented and non-crystalline polymer chains [163]. Due to advancements in processing technique and the successful application of new materials in the recent years, the efficiency has improved to approximately 2.8% [164]. The contribution of the polymer as a sensitizer can be experimentally estimated by comparing the power-conversion efficiency of the device in absence to the one in presence of the sensitizer dye.

2.5.4 Ionic Additives

Both, liquid-electrolyte and solid-state dye-sensitized solar cells, are known to show a substantial enhancement of the power-conversion efficiency after addition of ionic additives such as lithium bis(trifluoromethylsulfonyl)imide salt (Li-TSFI) and 4-tert-Butylpyridine (tBP) [165, 166]. Fig. 2.25 shows the chemical structures of these additives. Despite this influence, the exact role of the additives is still under debate.

Lithium ions are believed to shift the TiO_2 conduction-band edge to more positive potentials [167, 168]. Using microsecond transient absorption spectroscopy, Krüger *et al.* showed that additives can increase the charge recombination rate constant in solid-state dye-sensitized solar cells by up to one order of magnitude [166]. In another study, Li-TFSI has been shown to increase the mobility and conductivity of spiro-OMeTAD [169]. These effects are believed to be due to the electrostatic screening of the Coulomb attraction between the electrons in the TiO_2 and the holes in the spiro-OMeTAD as well as to the smoothing of the potential landscape of spiro-OMeTAD which facilitates intra-molecular charge transfer [169–172].

A recent study concludes, however, that the lithium salts are involved in a redox reaction p-doping the spiro-OMeTAD [173]. Spiro-OMeTAD forms a weakly bound donor-acceptor complex with an oxygen molecule. Photoexcitation can then lead to an effective electron transfer to the oxygen molecule, as shown in eq. 2.44.

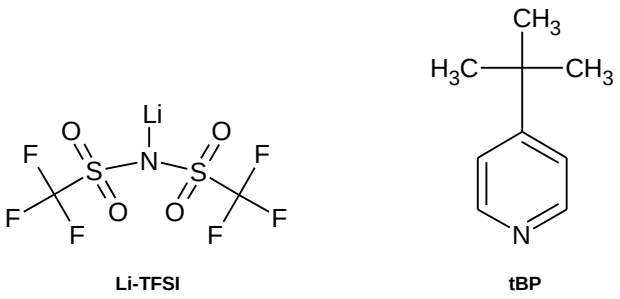

Figure 2.25: Chemical structures of lithium bis(trifluoromethylsulfonyl)imide salt (Li-TSFI) and 4-tert-Butylpyridine (tBP).

$$\text{Spiro-OMeTAD} + O_2 \leftrightarrow \text{Spiro-OMeTAD}^+ \, O_2^- \tag{2.44}$$

The concentration of Spiro-OMeTAD$^+$ was found to be low in devices. However, the addition of Li^+ leads to the consumption of O_2 as described in the following eq. 2.45 and, thus, increases the concentration of Spiro-OMeTAD$^+$.

$$\text{Spiro-OMeTAD}^+ \, O_2^- + \text{Li-TFSI} \rightarrow \text{Spiro-OMeTAD}^+ \, \text{TFSI}^- + Li_xO_y \tag{2.45}$$

Where Li_xO_y are lithium oxide complexes and were identified as Li_2O and Li_2O_2.

The Li-TFSI is therefore responsible for two effects. First, it facilitates charge generation and second, it reduces the series resistance by oxidation of the spiro-OMeTAD during which it is consumed. Since the first process requires the presence of the additives while the latter one consumes it, Li-TFSI was considered far from optimum for achieving the maximum possible power-conversion efficiency. Subsequently, the use of two different additives was suggested, one for enhancing the conductivity of spiro-OMeTAD and another one for improving charge generation at the interface.

Next to Li-TFSI and tBP, a recent study has introduced a new class of cobalt(III) complexes as p-type dopants for triarylamine-based hole-transporting materials which could be used as an alternative to the current additives [17]. Using these dopants in combination with an organic donor-π-acceptor dye, a record power-conversion efficiency of 7.2% was achieved.

Additionally, it was shown, that the new p-type dopant is not harmful for device stability.

2.6 Summary

- Organic Semiconductors (OS)
  - derive their properties from the carbon atom.
  - can be divided into two major classes, small molecules and polymers.
  - exhibit a low intrinsic charge carrier density. Next to (electro-)chemical and field-effect doping, charge carriers can be created either by injection from a contact or through photoexcitation.
  - show charge transport influenced by the disorder of the material with band and hopping transport as the two limiting cases.
- Single-Walled Carbon Nanotubes (SWNTs)
  - Single-walled carbon nanotubes can be defined according to their graphene lattice vector. SWNTs are either achiral, such as zig-zag $(n, 0)$ or armchair (n, n) tubes, or chiral. The chiral indices (n, m) dictate the tube's diameter d.
  - The electrical properties are given by their structure. Armchair carbon nanotubes, which have an (n,n) index, are metallic. Carbon nanotubes where $n - m$ is a multiple of 3 are semiconducting and have a small band gap. All other types are moderate semiconductors. Adjustments of this rule have to made for small diameter tubes.
  - Carbon nanotubes show strongly structured optical spectra due to sharp discontinuous spikes of their density of states. These are called Van Hove singularities and are conventionally labelled as E_{11}, E_{22} or S_{11}, S_{22}.
  - Photoluminescence excitation/emission (PLE) maps can show these peaks. Using a Kataura plot, the peaks can then be related to the structure of the nanotubes.

- Organic Photovoltaics (OPVs)
  - OPVs commonly have a high absorption coefficient, but band gaps tend to be large and absorption bands tend to be relatively narrow resulting in the absorption of only a small fraction of the solar spectrum.
  - The high Coulomb binding energy of excitons in organic materials requires a type-II heterojunction between a donor and acceptor blend in OPVs to separate excitons into electron and hole pair. The separated exciton first goes into a charge-transfer state before further charge separation into free polarons can occur. The exact mechanism is still under debate.
  - Due to the much smaller diffusion length of excitons in organic materials compared to their absorption depth, OPVs require a bulk heterojunction to efficiently separate excitons into free electron and hole pairs and avoid recombination of the excitons.
- Dye-Sensitized Solar Cells (DSSCs)
  - DSSCs separate the function of light absorption from charge carrier transport. Light is absorbed by a dye, followed by electron transfer into the conduction band of the TiO_2 and regeneration of the dye by hole transfer to the hole-transporting material.
  - Solid-state DSSCs provide an alternative to standard liquid-electrolyte based DSSCs which suffer from leakage and corrosion from the iodide/triiodide redox couple.
  - Optimization of light absorption, charge generation and transport, as well as pore filling are considered crucial for further enhancement of the performance of solid-state DSSCs.
  - While studies have shown the significance of pore filling on the device performance, the exact influence of the pore-filling fraction on the hole-transfer yield and charge collection is still unknown.

Chapter 3

Experimental Methods

3.1 Introduction

This chapter presents several different optical techniques such as UV-VIS absorption spectroscopy, scanning electron microscopy (SEM), as well as femto- and microsecond transient absorption spectroscopy which have been used in the studies discussed in chapter 4 to 6. Femtosecond transient absorption spectroscopy will be explained in greater detail compared to the other techniques since one of the goals of this thesis was to establish and optimise this particular system.

3.2 UV-VIS Absorption Spectroscopy

Ultraviolet and visible absorption spectroscopy (UV-VIS) measures the change in intensity of light of a specific wavelength after passing through a sample. The energy of light in the UV-VIS range is high enough to promote transitions of electrons in ions or molecules to higher energy levels. It is therefore a useful tool to probe the characteristics and composition of a variety of materials. In UV-VIS experiments, light with an intensity I_0 is sent through the sample and is partly absorbed leaving a transmitted beam with intensity I as shown in Fig. 3.1.

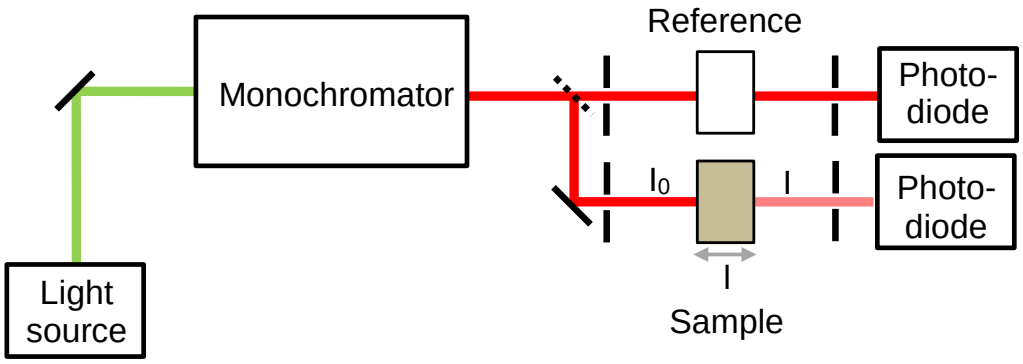

Figure 3.1: Sketch of a simple dual-beam UV-VIS absorption setup.

For solutions, the absorbance of a specific wavelength is determined by the thickness l, the concentration c and the molar absorptivity ϵ of the sample. Thus, knowing the thickness and the concentration, the molar absorptivity can be calculated using the Beer-Lambert law [174]

$$A = \log_{10}\left(\frac{I}{I_0}\right) = \epsilon c l \tag{3.1}$$

where A is the absorbance, sometimes also referred to as optical density OD, I_0 is the beam intensity before the sample and I is the beam intensity after the sample. For solid samples, the Beer-Lambert law is usually expressed in terms of the absorption coefficient α or as the product of the absorption cross section σ and the number density of absorbers N

$$A = \log_{10}\left(\frac{I}{I_0}\right) = \alpha l = \sigma N l \tag{3.2}$$

All UV-VIS absorption measurements in this thesis were carried out using a Perkin-Elmer Lambda 9 UV-VIS-NIR spectrophotometer. This commercial instrument uses a dual beam setup with a maximum detectable absorbance of 6. The obtainable wavelength range extends from 300 to 3199 nm. All thin film measurements were carried out using a small aperture

to avoid artifacts from spatial "wander" of the probe beam.

3.3 Femtosecond Transient Absorption Spectroscopy

3.3.1 Introduction

Many biological and chemical processes occur on time scales ranging from milliseconds to seconds. Experimental techniques such as time-of-flight experiments, impedance spectroscopy and others have been shown to be useful tools to study those processes [57, 175]. However, the long processes are the result of combinations of several very fast elementary processes ranging from femtoseconds to picoseconds. This generally is referred to as the ultrafast or ultrashort regime. In order to observe ultrafast processes, such as the translation or rotation of parts of a molecule, energy transfer, charge transport or the formation or breaking of a chemical bond, a measurement technique with a temporal resolution in the range of femtoseconds to picoseconds is required. Femtosecond transient absorption spectroscopy has been shown to be a powerful tool to observe such ultrafast processes [176]. In this experiment, the change in absorption of a sample is measured in dependence on the time after exciting it with a second laser pulse. The results allow for conclusion about the change in population of a specific particle species in the material.

3.3.2 Ultrashort Laser Pulses

Since the time resolution of transient absorption spectroscopy depends on the temporal width of the pump and probe pulse, ultrashort laser pulses are required to achieve a femtosecond resolution. To generate such short laser pulses, mode-locking is usually required [177]. A second requirement is a high pulse energy to make use of nonlinear effects in the setup. This can be achieved using regenerative amplifiers. However, ultrashort laser pulses reach very high peak powers which would lead to effects such as self-focusing and self-phase modulation in the amplifier and ultimately exceed the damage threshold of the materials involved in

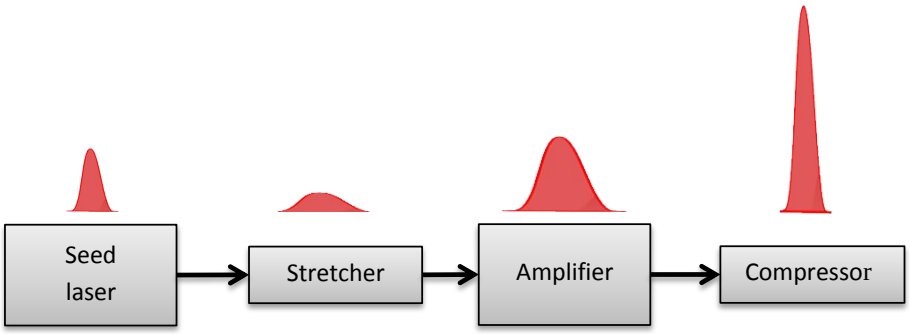

Figure 3.2: Schematic of the steps involved in chirped-pulse amplification: 1) Temporal broadening by a stretcher, 2) amplification, and 3) recompression.

the amplification process. To circumvent this problem, chirped-pulse amplification (CPA) is applied. Fig. 3.2 shows a sketch of this technique. It consists of three basic steps: First, the laser pulse is temporally broadened using a pulse stretcher which leads the pulse to reach a temporal duration of up to a nanosecond considerably reducing the initial high peak power. In the second step, the pulse can be safely amplified via a regenerative amplification technique. Initially, a high-energy nanosecond Q-switched seed laser pumps the gain medium. Then, the pulse is coupled into the amplifier cavity where it completes several round trips exhausting the population inversion of the gain medium and increasing the power of the laser pulse. At the point of completion, it is coupled out of the cavity. In the final step of chirped-pulse amplification, the laser pulse is temporally shortened again using a pulse compressor which is build on the same concept as a pulse stretcher, only reversed.

3.3.3 Pump-Probe Technique

For measurements on the femtosecond time scales, most electronic detectors are not fast enough to resolve a signal [178]. To overcome this, a pump-probe technique using a mechanical delay stage is employed. Fig. 3.3 shows a sketch of this technique. The output of an ultrafast laser is split into two pulses, a pump pulse which photoexcites the sample and a weaker probe pulse which is delayed by a mechanical delay stage and probes the sample. By changing the delay between pump and probe, the dynamics of the sample can be measured

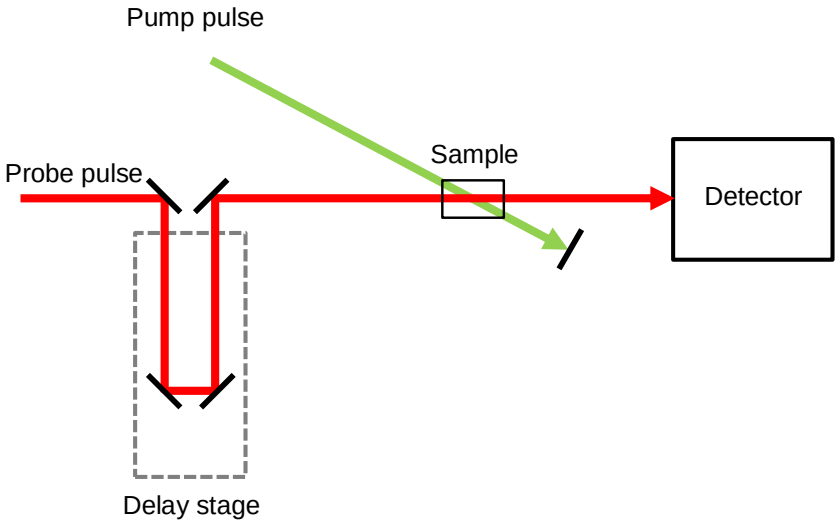

Figure 3.3: Sketch of the pump-probe technique.

on the ultrafast time scale.

The resolution of the experiment is determined by the duration of the pump and probe beam. The maximum time window, on the other hand, is given by the length l of the delay stage according to

$$t = \frac{2l}{c} = \frac{l}{0.015\text{cm}} ps \tag{3.3}$$

where c is the speed of light. Using a double-pass configuration, this time window can be increased by a factor of two. Fig. 3.4 shows a sketch of the idea. In the double-pass configuration, a retroreflector is placed on the delay stage. When the beam is reflected back on the retroreflector, it is displaced horizontally. After leaving the delay stage, the beam is then sent back again to the retroreflector using two mirrors. This time though, due to the properties of the retroreflector, the beam is shifted in the same amount horizontally, but in the opposite direction. As a result, the beam leaves the delay stage at the same height it entered it, assuming all mirror surfaces are aligned perpendicular to the delay stage, and traveled the delay stage four times.

Due to space constraints and alignment difficulties, the travel range of commercial delay

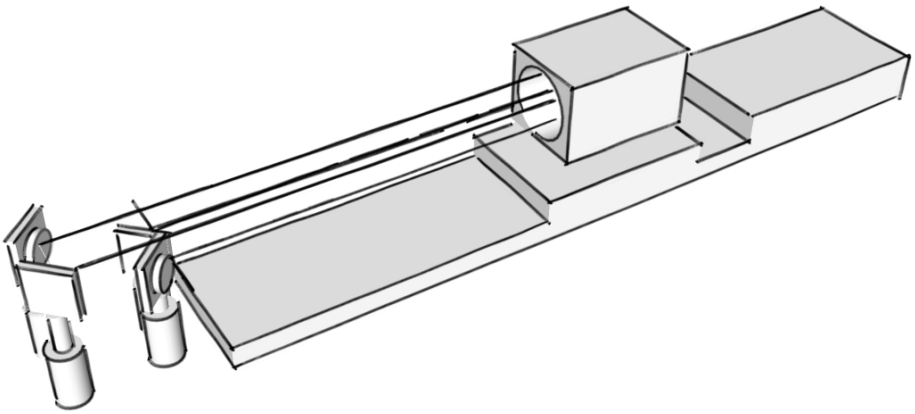

Figure 3.4: Double-pass delay-stage configuration

stages is usually limited to about 60 cm which converts to a 4ns time delay or a 8 ns time delay in the double-pass configuration. Commonly, though, time delays of only 1-2 ns are used.

3.3.4 Nonlinear Optics

Nonlinear optics is a sub-field of optics that studies situations where the dielectric polarization **P** of a medium does not depend linearly on the applied electric field **E**. This gives rise to a range of different optical phenomena, some of which are exploited in femtosecond transient absorption spectroscopy. However, the nonlinear dependence becomes relevant only at very high light intensities when the electric-field strength of the light is strong in comparison to the fields inside atoms and molecules [179]. Hence, the first observation of a nonlinear optical effect, second harmonic generation, was reported in 1961 after the invention of the laser [180, 181]. Several excellent sources on the theory of nonlinear effects exist [179, 182, 183]. Thus, only a short summary and only the nonlinear effects relevant for femtosecond transient absorption will be explained here based on these sources.

The optical properties of a dielectric medium through which light propagates can be described by a Taylor series expansion of the dielectric polarization **P** in terms of the applied electric field **E** [179]

$$\mathbf{P} = \epsilon_0(\chi^{(1)}\mathbf{E} + \chi^{(2)}\mathbf{E}^2 + \chi^{(3)}\mathbf{E}^3 + ...) \tag{3.4}$$

where $\chi^{(n)}$ is the n-th order electric susceptibility tensor. In linear optics only the first term is considered. If one of the higher order terms of the electric susceptibility is non-zero, the medium is said to be nonlinear. Nonlinear optics gives rise to several phenomena such as frequency mixing, four-wave mixing, cross-phase modulation and many more. Three of those effects, i.e. second harmonic generation, optical parametric amplification and supercontinuum generation are used in the femtosecond transient absorption setup and will be presented here in its very basic form.

3.3.5 Second Harmonic Generation (SHG)

Second harmonic generation (SHG) is a second-order nonlinear effect. When an electromagnetic wave is incident on an atom or molecule, the polarization induces new waves at frequencies [183]

$$\omega = \omega_1 \pm \omega_2 \tag{3.5}$$

which travel with a phase velocity of

$$\nu_{ph} = \omega/k = c/n(\omega). \tag{3.6}$$

To generate a macroscopic wave, the vectors of the phase velocities of the inducing waves incident on the material need to be properly matched. This is given by the phase matching condition [183]

$$\hbar\mathbf{k}(\omega_1 \pm \omega_2) = \hbar\mathbf{k}(\omega_1) + \hbar\mathbf{k}(\omega_2). \tag{3.7}$$

In second harmonic generation $\omega_1 = \omega_2 = \omega$, and Eq. 3.7 changes to

$$\hbar\mathbf{k}(2\omega) = 2\hbar\mathbf{k}(\omega) \tag{3.8}$$

A laser pulse with frequency ω incident on a second-order nonlinear medium thus generates a second pulse with frequency 2ω, twice the original frequency. Second-order nonlinear effects such as second harmonic generation, can be created, for instance, in non-centrosymmetric crystals such as ZnS, BBO, CdTe, GaAs, LiNbO, etc. [182]. In the case of this setup, the 800 nm output of a Ti:sapphire laser is converted into 400 nm using a β-barium borate (BBO) crystal.

3.3.6 Supercontinuum Generation (SCG)

The probe pulse of a femtosecond transient absorption setup should have a temporally high resolution and a spectrally broad profile to allow for the measurement of a wide wavelength region. Supercontinuum generation (SCG) has been proven to be an excellent source for the probe pulse due to its wavelength range extending over the visible and near-infrared when pumped with an 800 nm pulse and its low energy requirement for the seed pulse [184]. First demonstrated in 1970, in SCG a laser pulse is focused onto a transparent medium where it is converted by third-order nonlinear optical effects into a spectrally broad pulse [185]. Depending on the material, nonlinear effects such as self-phase modulation, phase matching and Raman scattering cause this broadband pulse [184–187]. The resulting pulse has a high spatial coherence and preserves in some cases its polarization direction [185, 188]. The threshold of supercontinuum generation generally coincides with the threshold for self-focusing [179]. A theoretical model of SCG has been proposed by Gaeta in 2000 [189]. Fig. 3.5 shows a schematic of a setup and a picture of a supercontinuum created with an ultrashort 800 nm laser pulse.

A supercontinuum pulse can be generated in a variety of different media such as water, fused silica, sapphire, and photonic crystal fiber [184, 190, 191]. Out of these, a sapphire plate

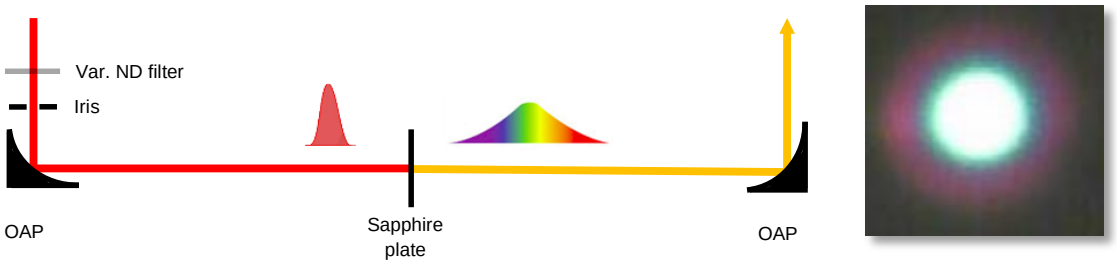

Figure 3.5: Left: Schematic of a supercontinuum generation setup using a sapphire plate. Right: Picture of supercontinuum generation in a Spec-B glass using an 800 nm ultrafast laser pulse.

with a thicknesses between 1 and 3 mm is the most common material used for the broadband probe pulse in femtosecond transient absorption setups. Using a wavelength of 800 nm for the seed pulse, the usable wavelength range of the supercontinuum extends approximately from 475 nm to 1500 nm [192]. This range can be extended further into the UV using calcium fluoride (CaF_2) or lithium fluoride (LiF) crystals [193, 194]. In contrast to sapphire crystals, CaF_2 needs to be under constant rotation or translation to prevent damage of the crystal [195, 196]. However, the rotation of the CaF_2 crystal causes intensity and polarization modulations in the generated supercontinuum pulse [197]. To mask the rotation of the crystal, the seed pulse can be circularly polarized resulting in intensity fluctuations of only 0.5% limited only by the laser stability. Fig. 3.6 shows a schematic employing this technique.

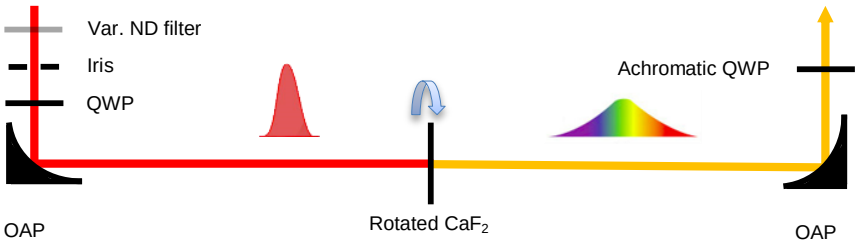

Figure 3.6: Schematic of a polarization- and intensity-maintaining supercontinuum generation setup in the UV using quarter-wave plates (QWP) and a rotating CaF_2 crystal [197].

3.3.7 Optical Parametric Amplification (OPA)

Optical parametric amplification (OPA) systems are widespread due to their ability to tune the wavelength of ultrashort laser pulses. An OPA relies on second-order and third-order nonlinear effects.

In an OPA, the signal pulse is sent through a nonlinear crystal together with a pump pulse. The pump pulse is then converted into two pulses, "signal" and "idler" which are determined by the initial wavelength of the pump pulse as well as the angle and symmetry axis of the crystal.

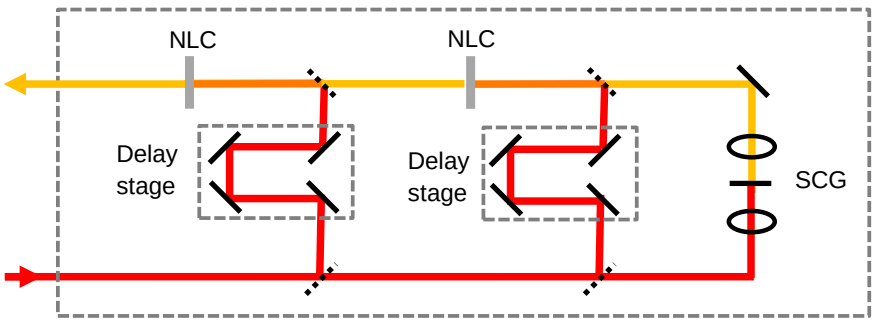

Figure 3.7: Schematic of a typical optical parametric amplifier (OPA). NLC: Nonlinear crystal, SCG: Supercontinuum generation. After [192].

Since many different OPA designs have been reported, only the general principle of a typical optical parametric amplifier will be described here [192]. Fig. 3.7 shows a sketch of such a typical system. An OPA is usually pumped by the output of an amplified femtosecond laser system using either the fundamental, in most cases 800 nm, or the second harmonic, 400 nm. In the first step, a seed beam is created using the principles of supercontinuum generation, as shown in the sketch here, or via parametric superfluorescence. The seed pulse is then overlapped with the pump pulse in a nonlinear crystal for the first parametric amplification stage. In order to achieve a temporal overlap between the two pulses, a delay stage is used in the beam path of the pump pulse. In the second amplification step, the beam is further amplified in a second nonlinear crystal.

3.3.8 Setup

Most organic materials show only very small changes in absorption, on the order of 10^{-4} to 10^{-5}, after excitation with a laser pulse of low fluence. To be able to measure these, the lock-in technique is applied. In this technique, a chopper is placed in the beam path of the pump and set to half the repetition rate of the pulse, thus, blocking every other pulse. This allows for the measurement of the probe transmission in presence of a pump excitation, followed by the measurement of the probe transmission in absence of a pump excitation. The so created oscillation with a peak-to-peak amplitude equal to the change in transmission can be detected by a lock-in amplifier allowing for good signal-to-noise ratios even for very small transmission changes. Fig. 3.8 shows a schematic of the idea.

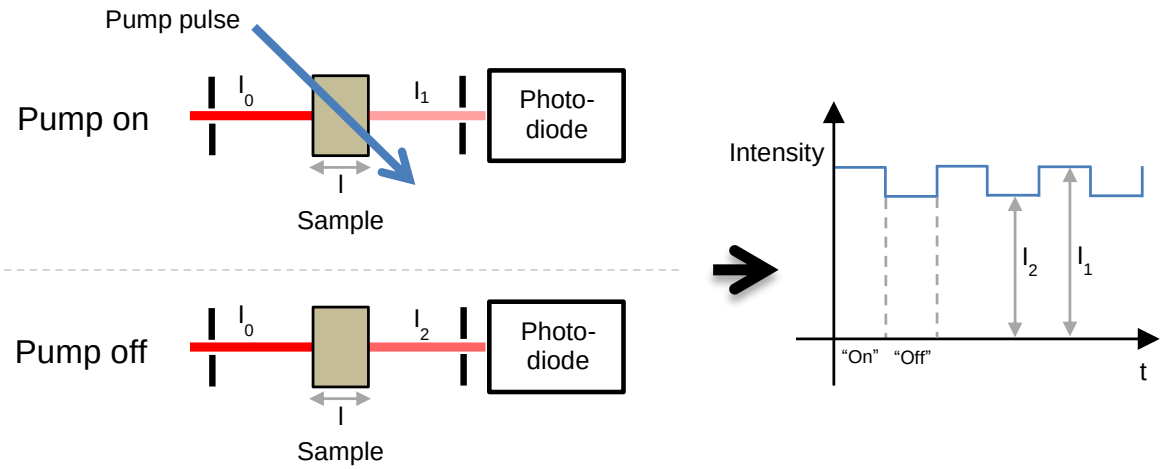

Figure 3.8: Schematic of the "pump-on", "pump-off" measuring technique for femtosecond transient absorption spectroscopy.

To extract the population density $N(t)$ from the measured change of transmission, the Beer-Lambert law is applied:

$$I(\lambda, t) = I_0(\lambda)\ 10^{-\sigma_\lambda N(t) l} \tag{3.9}$$

where $I_0(\lambda)$ is the spectral intensity of the incoming pulse, $I(\lambda, t)$ is the spectral intensity of the transmitted pulse, σ_λ is the absorption cross-section at the wavelength λ, and l is the

thickness of the sample. The relative change in transmission is then related to the change in population density $\Delta N(t)$ by

$$\begin{aligned} \frac{\Delta T}{T}(\lambda, t) &= \frac{I_1(\lambda, t) - I_2(\lambda)}{I_2(\lambda)} \\ &= 10^{-\sigma(N_1(t) - N_2(t))l} - 1 \\ &= 10^{-\sigma \Delta N(t) l} - 1 \end{aligned} \tag{3.10}$$

Or expressed in terms of change in population density:

$$\Delta N(t) = -\log_{10}\left(\frac{\Delta T}{T}(\lambda, t) + 1\right)/(\sigma l) \tag{3.11}$$

Often, the change in transmission is given in terms of the absorbance A or optical density OD as it is correlated linearly with the change in population density. It is related to the relative change in transmission by

$$\begin{aligned} \Delta OD &= \sigma \Delta N(\lambda, t) l \\ &= -\log_{10}\left(\frac{\Delta T}{T}(\lambda, t) + 1\right) \end{aligned} \tag{3.12}$$

Although, for very small changes in the population density, as it is often the case, the relative change in transmission is also linear to the population density due to the approximation $\log(1 + x) \approx x$ for small x

$$\Delta N(t) \approx -\frac{\Delta T}{T}(\lambda, t)/(\sigma l) \tag{3.13}$$

The transmitted signal can either be detected using a monochromator, which gives the optical density for a fixed probe wavelength at different delay times, or a multichannel

detector, which allows the detection of the optical density for the whole spectrum at a fixed time delay. Alternatively, an interference filter can be used.

Measurement of the signal from the sample is subject to several noise factors, such as laser beam fluctuations, sample emission, electronic and ambient noise [176]. To substantially eliminate laser beam fluctuations a two beam geometry can be used. The probe beam is split into two parts to create a reference beam that serves as a reference intensity.

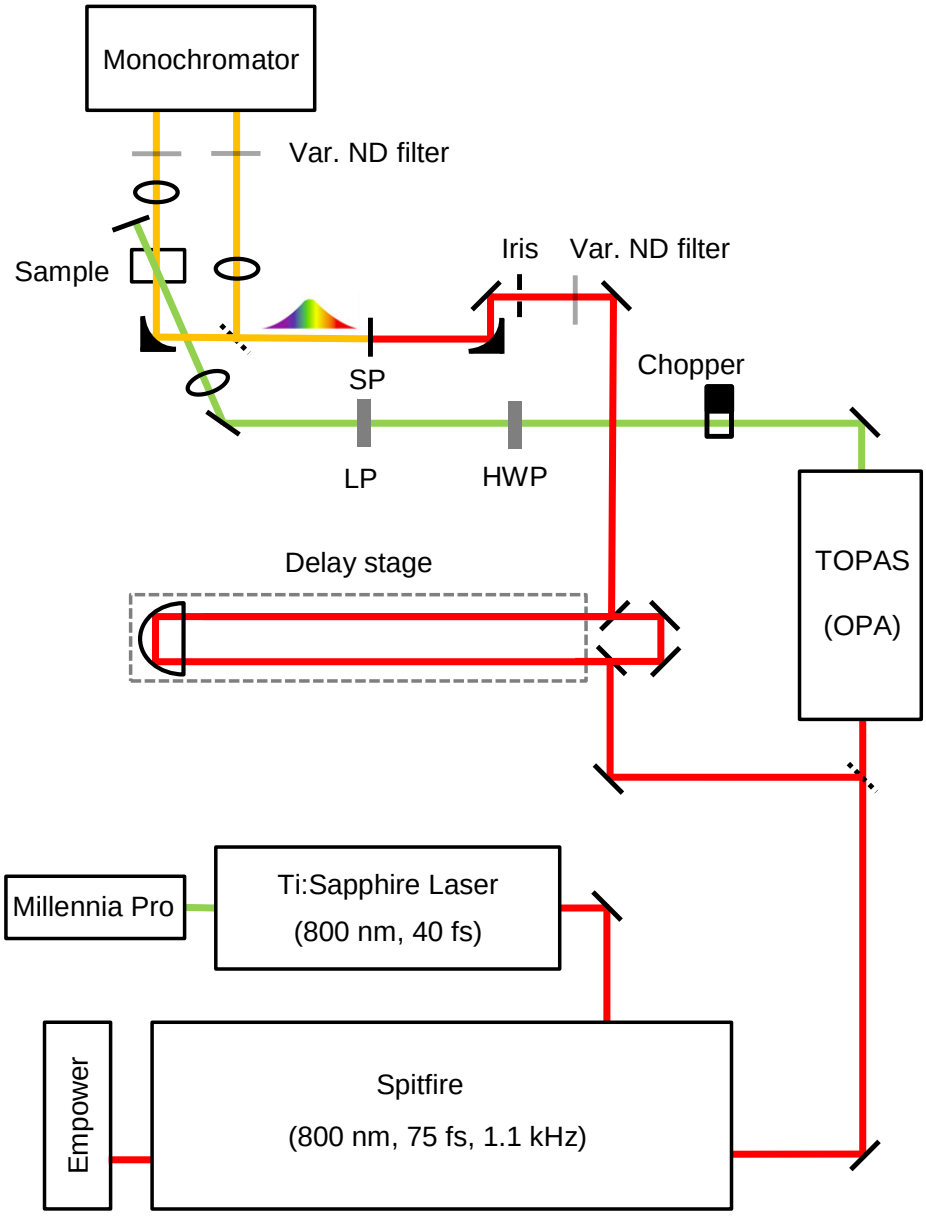

Figure 3.9: Sketch of the femtosecond transient absorption setup. SP: sapphire plate, HWP: half-wave plate, LP: linear polarizer

Fig. 3.9 shows a sketch of the complete femtosecond transient absorption setup. A Ti:Sapphire regenerative amplifier system (Tsunami, Spitfire) with a pulse duration of approximately 50 fs and a repetition rate of 1.1 kHz is used to generate a laser pulse with a wavelength of 800 nm and about 1 W power. The pulse is subsequently split into two parts, one is used as the pump pulse and fed either into an optical parametric amplifier (TOPAS) to tune the wavelength or alternatively frequency-doubled in a BBO crystal to generate a laser pulse with a wavelength of 400 nm. A chopper set to 550 Hz, half of the original frequency, is then used to create the "pump-on", "pump-off" signal. A half-wave plate (HWP) and a linear polarizer are used to set the polarization angle between pump and probe pulse to the "magic" angle of 54.7° [198]. At this angle, only the isotropic component of the signal is measured as the signal is equal to the sum of the signals when using parallel polarization ($\mathrm{OD}_{||}$) and twice the signal when using perpendicular polarization ($\mathrm{OD}_{\perp}$)

$$\mathrm{OD}_{\mathrm{iso}}(t) = \mathrm{OD}_{||}(t) + 2\mathrm{OD}_{\perp}(t) \tag{3.14}$$

If the anisotropic contribution is of interest, two separate measurements, i.e. for the pump and the probe pulse polarizations being parallel and perpendicular, need to be performed. The depolarization ratio is given by [198]

$$R(t) = \frac{\mathrm{OD}_{||}(t) - \mathrm{OD}_{\perp}(t)}{\mathrm{OD}_{||}(t) + 2\mathrm{OD}_{\perp}(t)} \tag{3.15}$$

where the denominator is equal to the measured signal in the case where polarizations are set to the "magic" angle.

The pump pulse is then focused onto the sample with the transmitted part being absorbed in a beam dump. The second part of the original beam is sent over a mechanical delay stage (Newport) in the double-pass configuration creating a maximum possible temporal delay between pump and probe pulse of approximately 2.2 ns. After attenuating the probe pulse with a variable neutral-density (ND) filter and an iris, a gold-coated off-axis parabolic mirror (OAP) is used to focus it onto a 2 mm thick z-cut quartz window (CVI Melles Griot) and

generate a supercontinuum pulse. Half of the pulse intensity is split off with a 50:50 beam splitter and used as a reference beam. The other half is focused onto a sample with a silver-coated OAP. In order to ensure a good spatial overlap between pump and probe pulse, the size of the pump is set to about five times the size of the probe. After passing the sample, the intensity of both probe and reference beam are adjusted by variable ND filters to reach the same values. This, however, is only done once at the beginning of the experiment. After the ND filters, probe and reference beam are either sent through an interference filter or a computer-controlled monochromator to select a specific wavelength before being detected by two Si/InGaAs photodiodes coupled to an integrator and a lock-in amplifier (Stanford SR830). The fluence of the pump pulse was set to 50 μJ/cm^2 for all measurements described in the following chapters.

3.3.9 Time Resolution

The resolution of the experiment can be measured via cross-correlation of the pump and the probe pulse in a BBO crystal. The sapphire plate is removed in the supercontinuum generation and the pump and the probe pulse are overlayed in the BBO crystal at different delay times. The cross-correlation of two functions is then given by

$$I_{cc}(\tau) = \int_{-\infty}^{+\infty} I_1(t) I_2(t-\tau) dt \tag{3.16}$$

where τ is the delay between pump and probe beam, $I_1(t)$ is the intensity of the pump and $I_2(t)$ the intensity of the probe. The resulting width of the function is related to the resolution by the deconvolution factor.

For two Gaussian beams

$$I_1(t) = I_{01} \ \exp\left(-2\frac{t^2}{\tau_1^2}\right) \tag{3.17}$$

$$I_2(t) = I_{02} \ \exp\left(-2\frac{t^2}{\tau_2^2}\right) \tag{3.18}$$

with τ_1 and τ_2 the $1/e^2$ pulse width for pump and probe beam, respectively, the cross-correlation function is given by

$$I_{cc}(\tau) = \frac{I_{01} I_{02} \sqrt{\frac{\pi}{2}}}{\sqrt{\frac{1}{\tau_1^2} + \frac{1}{\tau_2^2}}} \exp\left(-\frac{2t^2}{\tau_1^2 + \tau_2^2}\right) \tag{3.19}$$

The pulse duration of the cross-correlation function is therefore

$$\tau_{cc} = \sqrt{\tau_1^2 + \tau_2^2}. \tag{3.20}$$

For two identical beams, $I_1(t) = I_2(t)$, the equation reduces to

$$\tau_{cc} = \sqrt{2}\tau. \tag{3.21}$$

The deconvolution factor is therefore $\sqrt{2}$ for two identical Gaussian beams. For two hyperbolic secants (sech^2) the factor is 1.54.

It should be noted, that in femtosecond transient absorption spectroscopy it is preferential for the pump pulse to have a spectrally narrow profile to enable the selection of specific excitations of an optical transition. The same is true for the probe pulse where the selection of specific states can be important. However, the time-bandwidth product (or uncertainty principle) sets a lower limit on the product of temporal duration and spectral width of a pulse according to

$$\Delta t \Delta \nu \approx 0.44 \tag{3.22}$$

for Gaussian-shaped pulses. This reduces to 0.315 hyperbolic secants (sech^2). For instance, an 800 nm pulse with a pulse-width of 50 fs has a spectral bandwidth of approximately 19 nm at full-width at half maximum (FWHM). A compromise between temporal and spatial resolution is therefore required.

3.3.10 Artifacts

Femtosecond transient absorption experiments are subject to several artifacts, such as group velocity dispersion, polarization of pump and probe pulse and misalignment of the delay stage. These artifacts need to be taken into account when designing a set-up in order to determine the optical density with a high degree of accuracy.

Group velocity dispersion (GVD) arises when broadband pulsed lasers travel through dispersive optical materials. Different frequencies travel at different speeds through optical material and thus arrive at different times at the sample with red wavelengths leading blue ones. This can cause a change of the shape in the measured spectrum when the probe and the pump beam partly overlap and decrease temporal resolution. To avoid group velocity dispersion only reflective optics should be used. Additionally, a prism or grating based pulse compressor can be used for compensation [199–201]. Practical application of this method, however, is rather difficult [176]. Instead of a pulse compressor, group velocity dispersion can be compensated by correcting the spectra numerically. A numerical correction requires exact knowledge of the group velocity dispersion. Several methods can be used for measurement, such as measuring two-photon interaction [202], frequency mixing in a nonlinear crystal [203] or using the electronic optical Kerr effect [204]. The results can then be compared to a theoretical calculation based on the material and its thickness the beam is travelling through. The wavelength dependent refractive index can be calculated using Sellmeier's equation [205]

$$n(\lambda) = 1 + \frac{B_1\lambda^2}{-C_1 + \lambda^2} + \frac{B_2\lambda^2}{-C_2 + \lambda^2} + \frac{B_3\lambda^2}{-C_3 + \lambda^2} \tag{3.23}$$

where B_1, B_2, B_3 and C_1, C_2, and C_3 are the material constants. The values for different relevant materials are given in Table 3.1.

The relative time delay for a specific wavelength is then given by

$$t(\lambda) = \frac{l\ n(\lambda)}{c} \tag{3.24}$$

Material	B_1	B_2	B_3	C_1	C_2	C_3
Fused Silica	0.69617	0.40794	0.89748	0.004679	0.013512	97.93400
BK7	1.039612	0.231792	1.010469	0.006001	0.020018	103.560653

Table 3.1: Schott material constants of borosilicate crown glass (BK7) and Fused Silica for Sellmeier's equation [206].

where l is the thickness of the material.

The polarization of the pump and probe pulse is the second artifact that needs to be considered. With the use of linearly polarized light, as it is employed in most experiments, absorbing atoms or molecules with a transient moment oriented along the polarization detection will be perturbed preferentially causing an anisotropic perturbation in dipole orientation. Additionally, rotational diffusion of the molecules can take place and affect measurements. To measure only the population kinetics and avoid effects of rotational diffusion the polarizations of the pump and the probe pulse need to be set to the "magic" angle of 54.7° [198]. If the reorientation time is of interest, two separate measurements, i.e. for the pump and the probe pulse polarizations being parallel and perpendicular, need to be performed.

Another artifact is cross-phase modulation which describes the situation when the strong pump pulse changes the real part of the refractive index of the medium in time. For small time delays between pump and probe pulses, this change leads to a time-dependent modulation of its phase which alters the transmission spectrum.

Finally, misalignments of the delay stage can cause the biggest artifacts. A beam that is slight non-parallel to the delay stage causes a walk-off at the sample position and therefore a change in the pump-probe overlap. This changes the position of the spot measured as well as the fluence, if the misalignment is big enough. Non-physical features in the curve of the pump-probe measurement are the result. It is therefore crucial to constantly ensure a very good alignment. A retroreflector as the reflective optics on the delay stage is recommended as it reduces the degrees of freedom and therefore simplifies the alignment procedure and reduces the probability of misalignment.

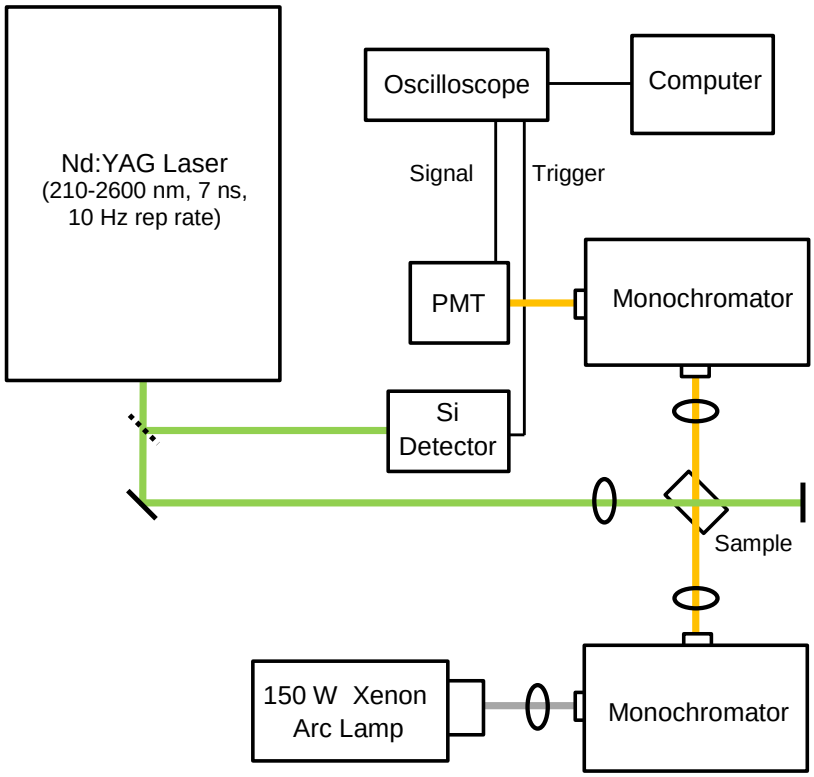

Figure 3.10: Sketch of the microsecond transient absorption setup. PMT: photomultiplier tube

3.4 Microsecond Transient Absorption Spectroscopy

3.4.1 Introduction

Whereas femtosecond transient absorption spectroscopy allows to monitor the initial charge generation and charge separation in the range of femto- and nanoseconds, microsecond transient absorption spectroscopy extends this time window from several hundred nanoseconds to a few milliseconds to observe recombination dynamics of generated charges.

3.4.2 Setup

In the microsecond transient absorption setup, an Nd:YAG laser (EKSPLA, NT340) with a 7 ns pulse duration, a 10 Hz repetition rate and a tunable wavelength from 210-2600 nm is used as the pump pulse. Part of the beam is split off by a beamsplitter and sent

into a silicon photodetector (Thorlabs DET10A/M) acting as a trigger for the oscilloscope. The remaining part is focused onto the sample. A beam dump terminates the transmitted beam. The probe beam is produced by the output from a 150 W continuous wave xenon arc lamp and sent through the sample after passing through a monochromator (Acton Research, SpectraPro 2150i). Before being detected by a fast photomultiplier tube module biased with 750 V (Hamamatsu, R9110), the transmitted probe beam is passed through a second monochromator (Acton Research, SpectraPro-2300i). Due to its longer time scale in comparison to femtosecond transient absorption spectroscopy, microsecond transient absorption spectroscopy does not need to apply the pump-probe technique. Instead, the time-dependent absorption are recorded on an oscilloscope (Tektronix, DPO3054).

3.5 Photoluminescence Upconversion Spectroscopy

3.5.1 Introduction

Photoluminescence Upconversion (PLUC) Spectroscopy is a technique used to measure the time-resolved photoluminescence of materials. The basic principle relies on a pulsed laser which is split into two parts, one being used as a pump pulse exciting the sample and the second one for optical gating in a non-linear crystal. To achieve a time-resolved measurement, the second pulse is delayed on a mechanical delay stage.

3.5.2 Setup

In the photoluminescence upconversion setup, a Millenia VIs frequency-doubled Nd:YAG laser (4W, 532 nm) is used pumped to pump a Tsunami Ti:Sapphire laser (Spectra-Physics) producing laser pulses with a duration of approximately 75 fs and a tunable centre wavelength range from 695-1060 nm. The laser pulse is split into two components using a half-wave plate and a polarising cube beam splitter. The first component is used as the excitation pulse. The second component is used to optically gate the photoluminescence at different time delays

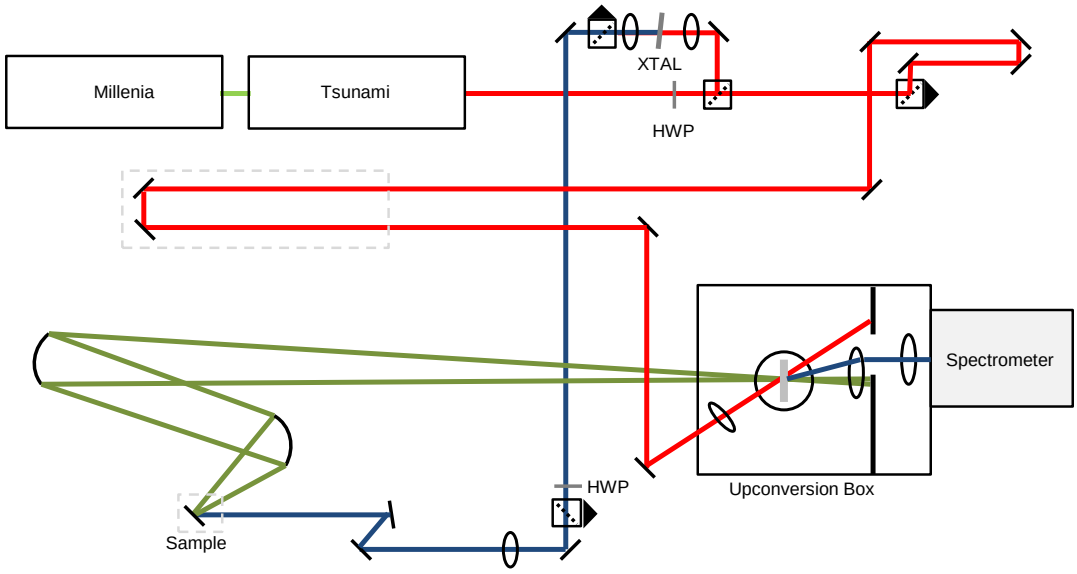

Figure 3.11: Sketch of the photoluminescence upconversion spectroscopy setup.

relative to the excitation. Following the gate beam path, the laser light is first being passed through a half-wave plate and a polarising beam splitter to rotate it back to its original orientation. Then, a computer-controlled mechanical delay stage is used to adjust the time delay between excitation and gate beam. Following the delay stage, the beam is directed into the upconversion box. Following the excitation beam path, a lens is used to focus the laser light onto a second-harmonic generating BBO crystal and collimated with a second lens. To remove the fundamental beam, the laser is directed through a Glen Thompson polarising prism with a beam dump attached to it. The beam is then passed through a half-wave plate and a Glen Thompson pair in order to set the polarisation state and the transmitted power of the laser beam. Following the Glen Thompson pair, the beam is focused onto the sample which resides in a vacuum chamber at a pressure of 10^{-7} mbar. The resulting photoluminescence is collimated and collected using an off-axis parabolic mirror. A second off-axis parabolic mirror is used to focus the light onto the crystal inside the upconversion box. In the crystal, the photoluminescence overlaps with the gate beam at a semi-angle of 6°, also known as the "mixing" angle, creating an up-converted light. Using a lens, this light is collected and directed through an aperture in order to remove the gate beam

and photoluminescence. Using a second lens and after passing through a band-pass filter further removing gate beam and photoluminescence residuals, the light is focused onto a spectrometer.

3.6 Time-Correlated Single Photon Counting (TCSPC)

Time-Correlated Single Photon Counting (TCSPC) is an experimental technique similar to Photoluminescence Upconversion Spectroscopy (PLUC). While PLUC uses optical gating, TCSPC uses electronic gating. This results on one hand in a lower time resolution, on the order of ∼100 ps, while on the other hand it allows for a higher sensitivity [207].

TCSPC experiments are performed on the same experimental setup as PLUC experiments which is shown in Fig. 3.11. Electronic gating is achieved by introducing a mirror into the gate beam which directs the laser pulse onto a Si-PIN diode acting as a trigger pulse to define the start of the measurement period. The measurement period ends either after the detection of a photoluminescence photon or the arrival of the next laser pulse. Integration of the detection signal over many measurements results in a time-dependent histogram of the sample photoluminescence.

3.7 Scanning Electron Microscopy (SEM)

An electron microscope uses an electron beam to interact with the surface of a specimen and create a strongly magnified image. Electron microscopes can achieve resolutions on the scale of 1 nm and were invented to increase the imaging resolution beyond those of optical microscopes which is approximately 200 nm. The improved resolution allows for the study of compositions and measurements of the thickness of layers in organic and dye-sensitized solar cells which will be employed in this work. Since these solar cells are too thick to transmit electron beams, a scanning electron microscope (SEM) is used. This kind of electron microscope sequentially scans the surface of the specimen and uses secondary and

back-scattered electrons to create an image displaying properties such as texture, crystalline structure, and composition. Secondary electrons are electrons of the specimen which are ejected during inelastic scattering of the energetic beam. Back-scattered electrons, on the other hand, are electrons that are reflected from the specimen by elastic scattering.

3.8 Monte Carlo Simulations of Pore Infiltration

3.8.1 Introduction

Next to the experimental techniques described above, in Chapter 4, Monte Carlo simulations were employed to verify and explain several results where analytical models were not obtainable. A simplistic model is used to simulate the filling of a pore with HTM molecules within a TiO_2 network of a dye-sensitized solar cell. The resulting molecule distribution is then used to simulate the diffusion of an exciton within the HTM molecule network as well as the to simulate the transfer of a dye cation from the dye network onto an HTM molecule.

3.8.2 Pore Filling Simulation

In the first step, the volume of the pore is split into equally-sized cubic cells each equivalent to the volume an HTM molecule would occupy within the pore. The volume of the pore is given by

$$V_{\text{pore}} = \frac{4}{3}\pi \left(\frac{d_{\text{pore}}}{2}\right)^3 \tag{3.25}$$

where d_{pore} is the diameter of the pore. The volume of an HTM molecule, and thus one cubic cell, is given by

$$V_{\text{htm}} = \frac{m_{\text{htm}}}{\rho_{\text{htm}}} = \frac{M_{\text{htm}} N_A^{-1}}{\rho_{\text{htm}}} \tag{3.26}$$

where M_{htm} is the molecular weight of the HTM, N_A^{-1} is the Avogadro constant and ρ_{htm} is the density of the HTM. The total number of HTM positions within the pore is then given by

$$n_{\mathrm{tot}} = \frac{V_{\mathrm{pore}}}{V_{\mathrm{htm}}} \tag{3.27}$$

where the number is rounded down to the nearest integer. The number of HTM layers within the pore can be calculated using

$$n_{\mathrm{layers}} = \frac{d_{\mathrm{pore}}/2}{l_{\mathrm{htm}}} = \frac{d_{\mathrm{pore}}/2}{V_{\mathrm{htm}}^{1/3}} \tag{3.28}$$

where the result is rounded up to the next integer. To calculate the number of positions in each individual layer, algorithm 1 is used.

Algorithm 1 Calculate number of positions in each layer

$n_{remaining} \leftarrow n_{tot}$
$i \leftarrow n_{layers} - 1$
for $i >= 0$ **do**
    if $d_{pore} < (2i+1) \cdot l_{htm}$ **then**
        $n[i] \leftarrow 0$
    else if $i = 0$ **then**
        $n[i] \leftarrow n_{remaining}$
    else
        $n[i] \leftarrow int(4.19 \cdot (((d_{\mathrm{pore}}/2) - i \cdot l_{\mathrm{htm}})^3 - ((d_{pore}/2) - (i+1) \cdot l_{\mathrm{spiro}})^3)/v_{\mathrm{pore}} \cdot n_{\mathrm{tot}} + 0.5)$
    end if
    $n_{remaining} \leftarrow n_{remaining} - n[i]$
    $i \leftarrow i - 1$
end for

In the next step, HTM molecules are placed onto a random position on the lowest layer of the pore. Random numbers for this process are created using the Mersenne Twister algorithm [208]. If the random position is already occupied by another molecule, then the new position depends on the type of coating simulated. For the random placement coating model, the molecule is simply placed one layer higher onto the existing molecule or, if that position is already occupied, two levels higher, etc. If conformal coating is simulated, the molecule is placed onto a random adjacent position to the original one. As each successive

layer contains fewer positions than the previous one and a direct mapping between layers is thus not possible, it is assumed that the number of available surface sites in each layer above the first layer is given by the difference between the number of infiltrated molecules in the previous layer and the number of already infiltrated molecules in this layer. If the number of infiltrated molecules in the previous layer exceeds the maximum possible number of molecules in the current layer, it is given by the difference between the maximum possible number of molecules in the current layer and the number of already infiltrated molecules in this layer.

Using the results of this simulation, the percentage $p(\mathrm{PFF})$ of dye surface covered with HTM molecules can be calculated by dividing the number of molecules in the lowest layer by the number of positions in the layer.

3.8.3 Exciton Diffusion Simulation

The resulting HTM molecule network from the previous simulation can also be used to simulate the diffusion of excitons generated within the HTM network. This is done using typical assumptions [209–211]: In the first step, excitons are placed on random spiro-OMeTAD molecules within the network. Migration is then modeled using a random walk to one of the neighbouring molecules. If an interface between dye and spiro-OMeTAD is reached, perfect quenching is assumed. In contrast, if the exciton reaches a non-quenching interface, perfect reflection occurs. To account for the natural recombination life time of excitons, the simulated results can be multiplied with the fitted decay response of a sample containing only spiro-OMeTAD.

3.8.4 Hole-Transfer Simulation

Furthermore, hole transfer from a monolayer of dye surrounding the pore to an HTM molecule can be simulated using the calculated HTM network structure. To do this, a dye cation is randomly placed within the dye monolayer. If the dye molecule is adjacent

to an HTM molecule in the lowest layer of the pore, transfer occurs. Otherwise, the cation transfers to a randomly selected and adjacent dye molecule. The hole-transfer yield can then be determined depending on the number of dye-to-dye hopping steps the cation can undergo before recombining with an electron.

3.9 Sample Preparation Techniques

The following procedure was performed by Derek Hollman for devices used in measurements in Chapters 4: Fluorine doped tin oxide (FTO) glass (15 Ω/sq , Pilkington) was etched for the appropriate electrode pattern with Zn powder and HCl (2 M). Substrates were cleaned sequentially with 2% Hellmanex, ethanol, and deionized water (water repeated three times). The substrates were cleaned in a plasma etcher for 10 minutes with oxygen as the source gas. A compact TiO2 (100 nm) layer was deposited via spray pyrolysis; for approximately each 100 cm^2 of substrate, titanium diisopropoxide bis(acetylacetonate) (20 mL of 100 mM, Sigma-Aldrich, 75 wt% in isopropanol) diluted in anyhydrous ethanol was sprayed, with oxygen as the carrier gas, onto the substrate held at 275 °C. A mesoporous layer of TiO2 paste (1.7 μm thick, Dyesol 18NR-T) was deposited by screen printing, and the substrates were sintered at 500 °C for 30 minutes following a 3 hour ramping. The substrates were treated in a $TiCl_4$ bath (15 mM) incubated at 70 C for 1 hour. After rinsing in deionized water, the substrates were re-sintered at 500 °C as before. The substrates were cooled to and held at 70 °C, after which the devices were immersed in a bath of C106 dye (150 μM, Organica) dissolved in 1:1 t-BuOH:ACN by volume. After approximately 18 hours, the devices were rinsed in an ACN bath and dried in air. A hole transport matrix solution was made from stock solutions (160 mM spiro-OMeTAD in chlorobenzene, 0.5 M lithium bis(trifluoromethylsulfonyl) imide (Li-TFSI) in ACN, and 2 M t-butyl pyridine (tBP) in chlorobenzene) diluted to the desired concentration of each component with chlorobenzene. The hole transport matrix was deposited by spincoating 25 μL of solution per 2 cm^2 of substrate at 1000 RPM for 60 s following a 10 s soak time. After drying in air, in dark, overnight, 200 nm thick silver electrodes were deposited on devices by thermal evaporation

at a pressure of ∼10-6 Torr with a shadow mask. Samples for spectroscopic measurements were prepared in the same way in parallel to samples for device measurements. However, the concentration of tBP and Li-TFSI was varied to verify its dependence on observed trends. In addition, FTO was replaced by a quartz substrate and deposition of silver electrodes onto the sample was omitted. Spectroscopy samples were stored in a glovebox, in dark, until one hour prior to measurement.

For measurements in Chapter 5, the following procedure was performed by Michael Lee: Fluorine doped tin oxide (FTO) coated glass (Pilkington TEC 15) 15 Ω/sq was patterned by etching with zinc powder and 2 M HCl diluted in Milli-Q water. The etched substrate was then cleaned with 2% Hellmanex detergent diluted in Milli-Q water, rinsed with Milli-Q water, acetone and ethanol and finally dried with clean dry air. The substrate underwent an oxygen plasma treatment for 5 minutes prior to spray pyrolysis of compact titanium dioxide, TiO_2. A thin layer of compact TiO_2 of roughly 100 nm was formed through spray pyrolysis of titanium diisopropoxide bis(acetylacetonate) diluted in anhydrous ethanol at a volumetric ratio of 1:10 using air as a carrier gas. Prior to the formation of the titania mesostructure, the substrate underwent an oxygen plasma treatment for 1 minute. 1 μm thick TiO_2 was formed by spin coating TiO_2 paste (DSL 18-NRT, Dyesol) diluted in anhydrous ethanol at 1.5:1 by weight at 2000 RPM (spin coating was preferred to screen printing or doctor blading due to greater control of mesostructure thickness). The freshly cast layer was then sintered in air at 550 °C. The substrates were immersed in a bath of $TiCl_4$ at a concentration of 15 mM for 1 hour at 70 °C, followed by rinsing in Milli-Q water and heating to 550 °C and cooled to 70 °C. Once substrates reached 70 °C, they were immersed in solution of Z907 dye for 18 hours. Z907 dye was mixed at a concentration of 0.3 mM and dissolved in a solution of acetonitrile anhydrous to tert-butyl alcohol at equal volumetric ratio. For devices with ionic additives, the HTM spiro-OMeTAD (Lumtec) as well as HTMs 1-3 (BASF) were dissolved in chlorobenzene at 0.17 mM, 4-*tert*-butyl pyridine [166] (Sigma Aldrich), and 0.21 mM of lithium bis(trifluoromethylsulfonyl)imide salt [169] (Sigma Aldrich) dissolved in anhydrous acetonitrile at 170 mg/mL mixed in a N_2 glovebox. Prior to spin coating, sensitized substrates were rinsed in a bath of acetonitrile, 25 μL of the hole-transporting material solution was

cast onto the sensitized substrate and spun at a rate of 2000 RPM for 45 seconds. Cells were left in the dark in air overnight. To complete the device, 200 nm Ag electrodes were thermally evaporated. Samples for spectroscopic measurements were prepared in the same way in parallel to samples for device measurements. FTO was replaced by a quartz substrate and deposition of silver electrodes onto the sample was omitted. Spectroscopy samples were stored in a glovebox, in dark, until one hour prior to measurement.

3.10 Summary

In this Chapter, the following experimental methods used in this thesis are summarised:

- UV-VIS Absorption spectroscopy measures the transmission of light through a sample. The change in light intensity can then be related to the molar absorptivity ϵ using the Beer-Lambert Law. This can be used to characterise materials.
- Femtosecond transient absorption spectroscopy measures the change of transmission on very short timescales, from femtoseconds to nanoseconds. However, it is prone to artifacts such as group velocity dispersion, cross-phase modulation, polarization of the pump and probe pulse, and misalignment of the delay stage which need to be considered carefully when doing experiments.
- Microsecond transient absorption spectroscopy expands the time window of femtosecond transient absorption spectroscopy to a range from a couple hundred nanoseconds to a few milliseconds. It can be used to study longer lifetime and recombination dynamics of charges in organic and dye-sensitized solar cells.
- Scanning Electron Microscopy (SEM) is a high-resolution imaging technique that uses an electron beam to interact with the surface of a specimen and create a strongly magnified image. SEM is used in this work to measure the thickness of different layers in dye-sensitized solar cells.
- Monte Carlo Simulations of Pore Filling

Chapter 4

Dependence of Dye Regeneration and Charge Collection on the Pore-Filling Fraction in Solid-State Dye-Sensitized Solar Cells

The work presented in this chapter has been published in:

C. T. Weisspfennig, D. J. Hollman, C. Menelaou, S. D. Stranks, H. J. Joyce, M. B. Johnston, H. J. Snaith and L. M. Herz Dependence of Dye Regeneration and Charge Collection on the Pore-Filling Fraction in Solid-State Dye-Sensitized Solar Cells. *Advanced Functional Materials*, **24** (5), 1616–3028, 2014.

4.1 Introduction

Dye-sensitized solar cells (DSSCs) offer a promising route towards production of cost-effective photovoltaic systems with low construction energy requirements [6, 9]. As detailed in Chapter 2, a dye sensitizer absorbs incident sun light, followed by electron injection into a mesoporous metal-oxide electrode and dye regeneration. For the latter step, DSSCs have conventionally incorporated an iodide/triiodide(I^-/I_3^-) liquid electrolyte as a redox mediator [212]. However, the possibility of solvent leakage and corrosion and the low redox

potential of I^-/I_3^- have limited further efficiency improvements of DSSCs [140, 141]. To overcome these issues, cobalt complex redox mediators have recently been demonstrated which achieve power-conversion efficiencies of up to 12% [115]. In an alternative approach, a solid-state hole-transporting material (HTM) is employed to replace the liquid electrolyte. Here, the most commonly and successfully used HTM has been 2,2',7,7'-tetrakis(N,N-di-p-methoxyphenylamine)-9,9'-spirobifluorene (spiro-OMeTAD) [16]. However, despite significant improvements over the last two decades, the performance of solid-state DSSCs using spiro-OMeTAD has not surpassed a power-conversion efficiency of 7.2% which is lower than that of the best cells employing liquid-electrolytes [17]. The main reason for this discrepancy is that solid-state DSSCs show optimized performance at relatively low layer thickness of only $\sim 2\,\mu$m, which limits light harvesting efficiencies [147]. It has been proposed that crucial limitations to layer thicknesses are the intrinsically low mobility of spiro-OMeTAD [149] and incomplete filling of the mesoporous TiO_2 pores with the HTM [15, 116, 148]. Conceptually, a high pore-filling fraction (PFF) should be required to allow both efficient dye regeneration by hole transfer to the HTM, and to offer percolation pathways for holes to the cathode for effective charge collection.

Filling of the pores is commonly achieved by deposition of a solution of spiro-OMeTAD on top of the mesoporous TiO_2 network layer followed by spin coating. During this process, the solution can initially penetrate into the pores and achieve a PFF proportional to the initial volume concentration of the solution. However, once the solvent begins to evaporate, the remaining solution on top of the TiO_2 can act as a reservoir and increase the spiro-OMeTAD concentration in the pores by filling the space previously occupied by the evaporated solvent. Thus, PFFs higher than the initial volume concentration of the solution can be achieved, [154] although in reality a value of 100% is unattainable because some vacant space will be left in the pores as the solvent evaporates [154, 213].

Despite the clear importance of pore filling on the device efficiency, its precise influence on the hole-injection and charge-collection efficiency is not well understood. Initial studies suggested that for optimized devices, hole transfer from the dye to the HTM occurs with

efficiencies of near unity, even though pore filling is not fully complete [15, 146]. These findings agree with a suggestion that complete hole transfer should be possible once the entire TiO_2 surface is covered with at least a single layer of spiro-OMeTAD [213] which does not require full filling of the pore. However, lower PFFs might still achieve close to complete hole-transfer yields, if holes can diffuse through the dye network before transferring to the HTM [214]. In addition, a sufficiently high PFF is required to ensure optimized charge collection towards the electrodes. Device studies suggest that for these reasons, a PFF of at least 60% is necessary to achieve optimized device performance [215]. However, the overall picture of how the hole-transporting material arranges inside the pores upon solvent evaporation, and the subsequent effect on charge migration, are still a matter of debate.

Here, a complementary spectroscopic and device investigation into the effect of pore-filling fraction on solid-state DSSCs incorporating a TiO_2 mesoporous electrode sensitized with a Ruthenium dye, and spiro-OMeTAD as the HTM is presented. First, a combination of microsecond transient absorption and femtosecond photoluminescence (PL) spectroscopies is applied. From these measurements crucial insights into both the yield of hole transfer from the dye to the HTM, and the mode of arrangement of the HTM in the pore can be gained. The hole-transfer yield is found to improve rapidly with increasing PFF and reaches a maximum at a value of only $\sim$30%, in agreement with hole diffusion within the dye network preceding hole transfer to the HTM. Moreover, information on the HTM layer arrangement within the pore is found by applying simple Monte Carlo techniques to replicate the observed transfer of charges at the dye:HTM interface, and the movement of excitations through the HTM material. These combined spectroscopic studies reveal that HTM filling of the pore can be modeled through successive layer build-up of molecules assuming random positions on the pore wall. Subsequently, these findings are correlated with performance data for a matching set of full DSSCs. A series of sharp onsets in both device photocurrent and efficiency with increasing pore-filling fraction is observed. By applying percolation theory, it is shown that these onset points have excellent correspondence with the formation of complete charge collection pathways in successive layers of such randomly positioned hole-transporting molecules on the pore wall. While the formation of a full charge percolation pathway in

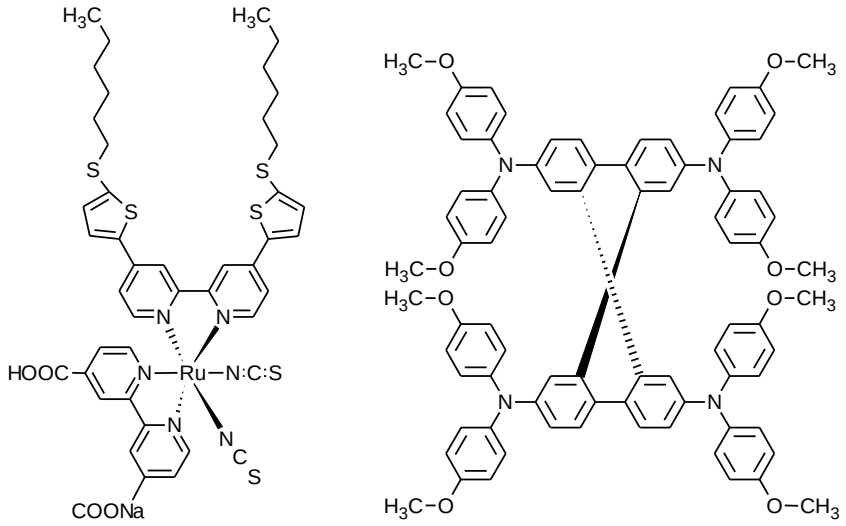

Figure 4.1: Chemical structures of the dye sensitizer NaRu(4,4'-bis(5-(hexylthio)thiophen-2-yl)-2,2'-bipyridine)(4-carboxylic acid-4'-carboxylate-2,2'-bipyridine)(NCS)2, known as C106, and the hole-transporting material 2,2',7,7'-tetrakis(N,N-di-p-methoxyphenylamine)-9,9'-spirobifluorene (spiro-OMeTAD) employed in the DSSCs investigated in this study.

the first HTM monolayer is clearly essential for extraction of any photocurrent, pathway completion in subsequent layers may give further step-change in photocurrent because these offer shorter routes located further away from an interface at which charge recombination losses can occur. By modelling such pathway completion predictions from percolation theory can be made on how pore-filling fractions must be tailored for optimized device performance.

4.2 Results and Discussion

Fig. 4.1 shows the chemical structures of the molecular materials incorporated in the investigated DSSC devices. NaRu(4,4'-bis(5-(hexylthio)thiophen-2-yl)-2,2'-bipyridine)(4-carboxylic acid-4'-carboxylate-2,2'-bipyridine)(NCS)2, known as C106 [121], is used as a dye sensitizer forming a monolayer on a TiO_2 network with pores of average diameter d_{pore} ∼20 nm [216] that are partially infiltrated with spiro-OMeTAD as the hole-transporting material. Two sets of samples with varying PFF were prepared in parallel by Derek J. Hollman, one for spectroscopic measurements and another for device measurements. The sample sets only

differed in that for those used in spectroscopy, quartz substrates were used (instead of FTO) and the deposition of silver electrodes was omitted. Samples were prepared for 14 different volume concentrations of spiro-OMeTAD in solution ranging from 0% to 20% to cover the maximum accessible range of PFFs. The actual PFF resulting from these solution concentrations can be quantified by one of several techniques [154, 213, 215]. In the method chosen here, the PFF is calculated from the sum of the spiro-OMeTAD volume concentration present in the pores before solvent evaporation, and the increase in concentration due to further infiltration during evaporation [154]. The former is equal to the volume concentration c of spiro-OMeTAD in the initial solution while the latter is inferred from the difference in the amount of spiro-OMeTAD on top of the TiO_2 before and after evaporation, divided by the volume of the pores. Here, the amount of spiro-OMeTAD before evaporation can be calculated from the product of the thickness d_{sol} of the deposited solution layer on top of the TiO_2 and the solution concentration c. The amount of HTM present after evaporation is given by the thickness of the resulting solid capping layer d_{cl}. The volume of the pores is determined by the product of porosity p and thickness d of the TiO_2 mesoporous network layer. The PFF can thus be calculated using [154]

$$\mathrm{PFF} = \mathrm{c} + \frac{\mathrm{d_{sol}c} - \mathrm{d_{cl}}}{\mathrm{d\,p}}. \tag{4.1}$$

For these calculations, the thickness d_{sol} and the porosity p were taken to be $6.9 \pm 0.5\,\mu$m and $49 \pm 1\%$, respectively [215]. The thickness d of the TiO_2 network and the capping layer d_{cl} were measured for each sample through cross-sectional SEM imaging, as shown in Fig. 4.2. Using this method, pore-filling fractions ranging from 0–67% were accessible in this study.

As a first assessment, it was spectroscopically investigated how the pore-filling fraction affects the efficiency of hole transfer from the dye sensitizer to the hole-transporting material. Primary electron transfer from the photoexcited dye into the TiO_2 occurs on the femto- to pico-second time scale [130, 133]. The subsequent hole transfer from the dye onto the HTM has been shown to cover a broad time range from pico- to nano-seconds [146]. As required, hole injection is hence several orders of magnitude faster than the competing recombination

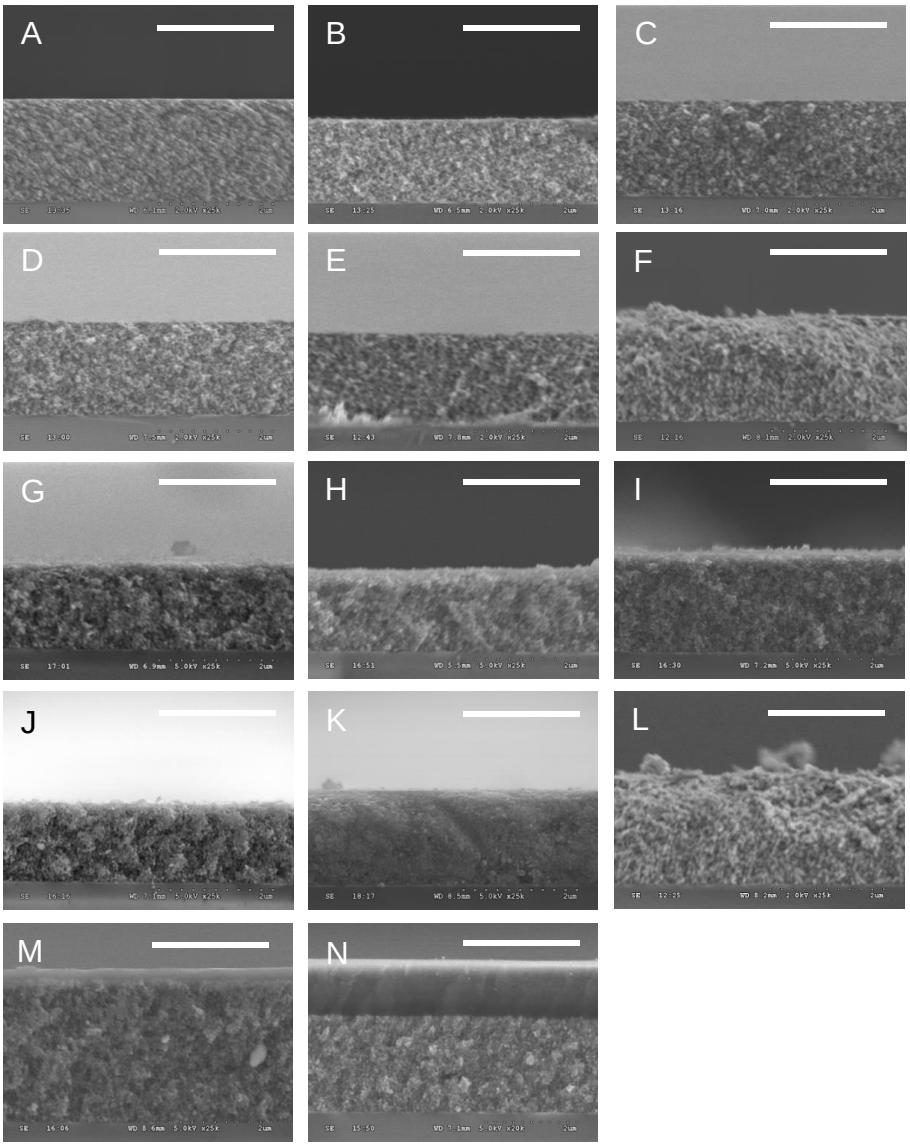

Figure 4.2: Cross-sectional SEM images of TiO_2/C106/spiro-OMeTAD samples prepared with varying volume concentrations of spiro-OMeTAD in the initial solution: (A) 0%, (B) 0.5%, (C) 1.0%, (D) 1.5%, (E) 2.0%, (F) 2.5%, (G) 3.0%, (H) 3.5%, (I) 4.0%, (J) 4.5%, (K) 5%, (L) 7.5%, (M) 10%, (N) 20%. The scale bars are 2 μm long. The SEM images were taken together with Dr. Sam D. Stranks.

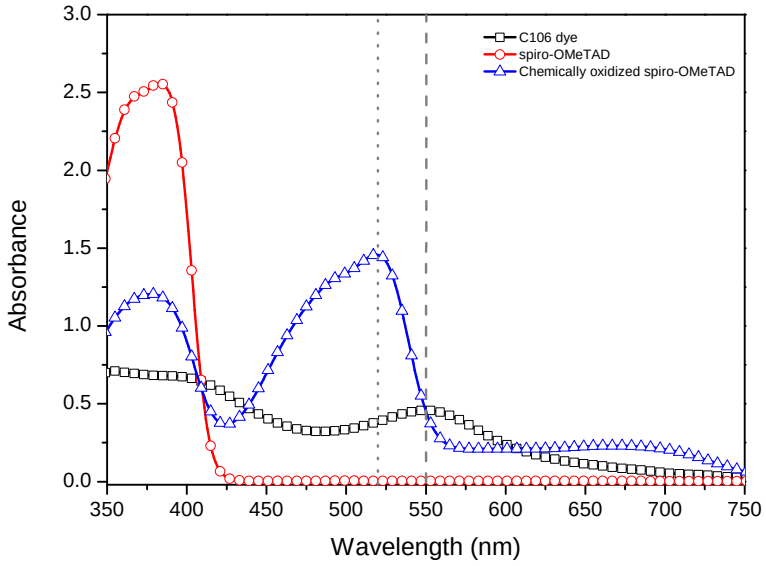

Figure 4.3: UV-VIS absorption measurements of the dye C106 (black squares), spiro-OMeTAD (red circles), and chemically oxidized spiro-OMeTAD (blue triangles). The grey dashed line shows the excitation wavelength of 550 nm used in the microsecond transient absorption experiments, while the grey dotted line shows the detection wavelength of 520 nm.

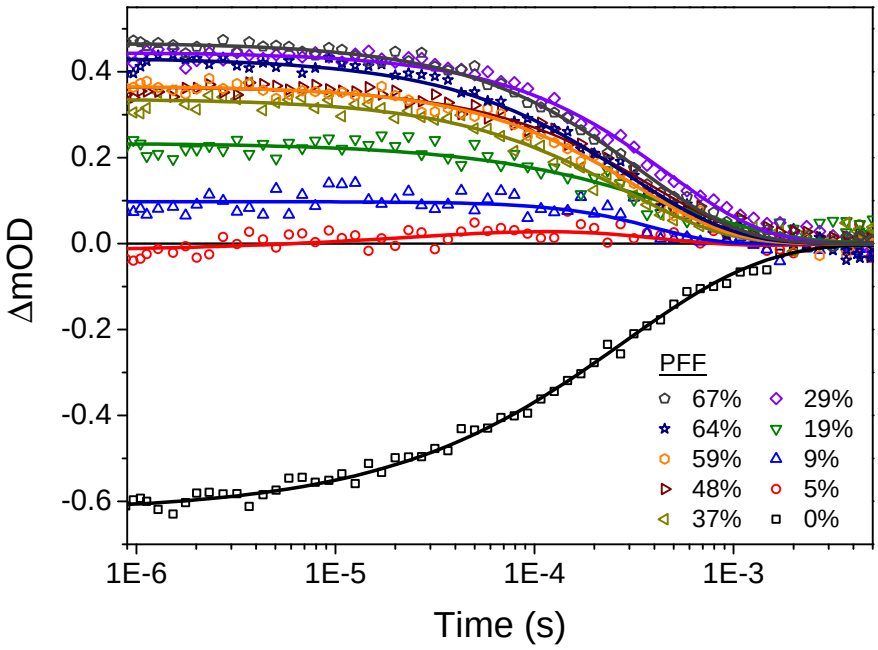

Figure 4.4: Microsecond transient absorption dynamics of TiO_2/C106/spiro-OMeTAD samples with varying pore-filling fractions measured at a probe wavelength of 520 nm. The samples were excited at 550 nm with a fluence of 50 μJ cm^{-2}. Results are averaged over those obtained from two samples with identical pore-filling fraction. For the transients displayed, no ionic tBP or Li-TFSI salts had been added to the materials. The solid lines are guides to the eye.

process between the dye cation and an electron present in TiO_2, which occurs on the micro- to millisecond timescale [137–139]. Microsecond transient absorption spectroscopy therefore provides an excellent tool to quantify hole-injection efficiencies as well as the subsequent recombination dynamics [157, 166] by probing for the presence or absence of absorption features associated with the neutral or charged states of the dye or HTM.

For measurements presented here, samples were photoexcited at a wavelength of 550 nm as this coincides with an absorption peak of C106 as well as an absence of absorption from spiro-OMeTAD, as shown in Fig. 4.3. At the employed probe wavelength of 520 nm two main contributions to the signal arise, which are photoinduced absorption (PA) from the spiro-OMeTAD radical cation [146, 217] and photobleaching (PB) of the ground-state absorption of the dye [218] caused by the presence of neutral or charged species on the dye. Fig. 4.4 displays microsecond absorption spectroscopy transients for samples with a range of different pore-filling fractions. At early times within the observation window (1-2 μs) the signal is relatively constant and it hence reflects the period after which any charge exchange at the TiO_2:dye:HTM interface will have occurred, but before any subsequent recombination has become evident. For the sample containing no HTM (i.e. 0% PFF) the negative signal arises solely from PB of the dye cations, while for samples with non-zero PFF, the signal is a combination of negative PB from dye cations for which hole transfer has not been feasible, and positive PA from HTM molecules that have received a hole. Hence, the hole-transfer yield can be determined as a function of the pore-filling fraction by referencing the initial (1-2 μs) change in optical density ΔOD for a sample of given PFF against $\Delta\mathrm{OD}_{\mathrm{dye}}$ for the sample containing no HTM: [18, 146, 157]

$$\begin{aligned}
\mathrm{Yield(t)} &= c_{\mathrm{HTM^+}}(t)/c_{\mathrm{dye^+,noHTM}}(t) && (4.2)\\
&= \left(\frac{\Delta\mathrm{OD(t)} - \Delta\mathrm{OD_{dye}(t)}}{\epsilon_{\mathrm{HTM^+}} + (\epsilon_{\mathrm{dye^+}} - \epsilon_{\mathrm{dye^0}})}\right) / \left(\frac{-\Delta\mathrm{OD_{dye}(t)}}{\epsilon_{\mathrm{dye^+}} - \epsilon_{\mathrm{dye^0}}}\right) && (4.3)\\
&= \left(1 - \frac{\Delta\mathrm{OD(t)}}{\Delta\mathrm{OD_{dye}(t)}}\right)\left(1 + \frac{\epsilon_{\mathrm{HTM^+}}}{\epsilon_{\mathrm{dye^+}} - \epsilon_{\mathrm{dye^0}}}\right)^{-1} && (4.4)
\end{aligned}$$

Here, $c_{\mathrm{HTM^+}}$ is the concentration of HTM cations in a sample containing HTM and $c_{\mathrm{dye^+,noHTM}}$

is the concentration of dye cations in a sample containing no HTM. $\epsilon_{\mathrm{HTM^+}}$ is the extinction coefficient of cations in the HTM, and $\epsilon_{\mathrm{dye^+}} - \epsilon_{\mathrm{dye^0}}$ is the difference between the extinction coefficients of cations and the ground-state of the dye. Qualitative inspection of the early-time transient absorption signal (Fig. 4.4) shows that the hole-injection yield into the HTM initially rises rapidly but then saturates with increasing PFF. The subsequent decay dynamics of the transient absorption signal are dominated by charge recombination across the interface. For the sample containing no HTM, the observed reduction of dye cation PB is attributed to recombination with electrons in the TiO_2. The half-reaction time is extracted as $\sim$160 μs, which is similar to lifetimes reported for use of the alternative dyes cis-Bis(isothiocyanato)(2,2'-bipyridyl-4,4'-dicarboxylato)(4,4'-di-nonyl-2'-bipyridyl)ruthenium(II) (Z907) and Ru^{II}(2,2'-bipyridyl-4,4'-dicarboxylate)$_2$(NCS)$_2$ (N3) [120, 219]. For samples with high PFF the observed dynamics similarly reflect charge recombination across the TiO_2:dye:HTM interface. Here, half-reaction times appear to be quite similar to those observed in the absence of HTM, which is because in the absence of ionic additives, cations in spiro-OMeTAD tend to remain localized close to the charge-generating surface [220]. It should be noted that in order to determine the fundamental properties of the hole-injection process all of the measured samples were prepared without ionic additives. However, both liquid-electrolyte and solid-state dye-sensitized solar cells are known to show a substantial enhancement of the power-conversion efficiency after addition of ionic additives such as lithium bis(trifluoromethylsulfonyl)imide salt (Li-TSFI) and 4-tert-Butylpyridine (tBP) [165, 166, 221–223]. Thus, to determine the influence of additives on the hole-transfer yield, the same transient absorption experiment were performed with samples containing varying concentrations of tBP and Li-TFSI and varying PFFs. While a change in decay dynamics is visible, as shown in Fig. 4.5, no significant dependence of the hole-transfer yield on the concentration of tBP and Li-TFSI were observed, within the experimental error. It is hence concluded that while charge recombination dynamics are, as expected, affected by ionic additives, hole-transfer yields appear to be largely independent and these effects will therefore be ignored for the remainder of the discussion.

Fig. 4.6 shows the yields of hole transfer from dye to HTM as a function of pore-filling

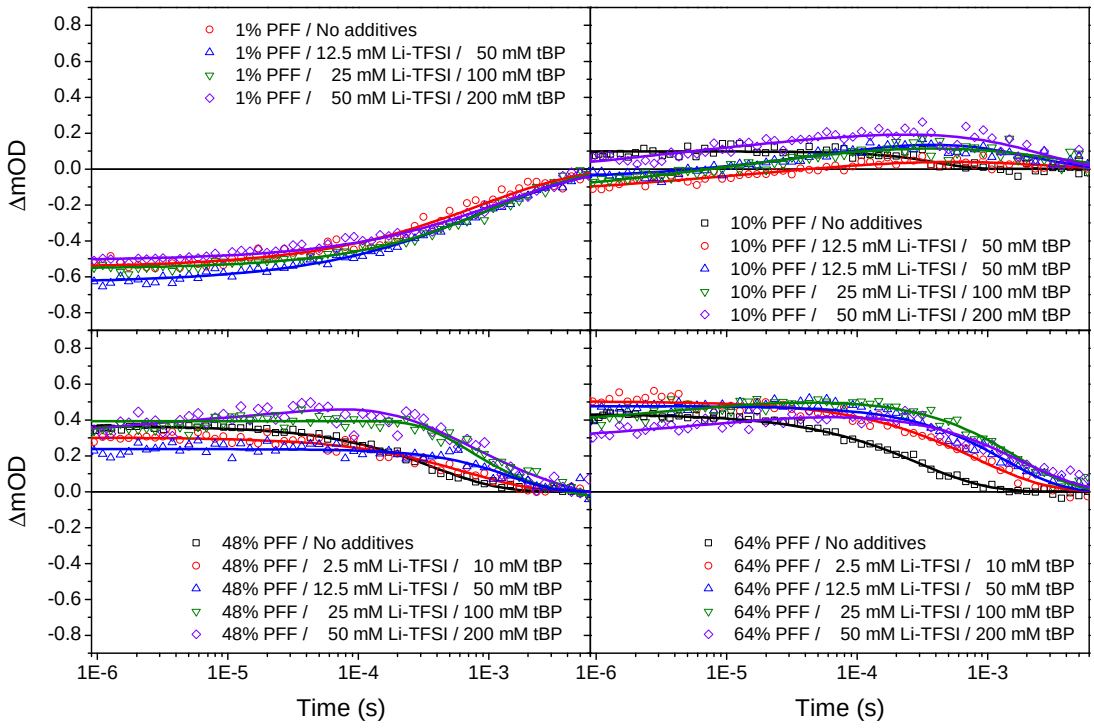

Figure 4.5: Microsecond transient absorption dynamics of TiO_2/C106/spiro-OMeTAD samples with a pore-filling fraction of 1%, 10%, 48%, and 64%, and varying concentrations of the standard additives Li-TFSI and tBP. All samples were measured at a probe wavelength of 520 nm and were excited at 550 nm with a fluence of 50 μJ/cm^2. Results are averages over data obtained from two samples with identical pore-filling fraction. The solid lines are a guide to the eye.

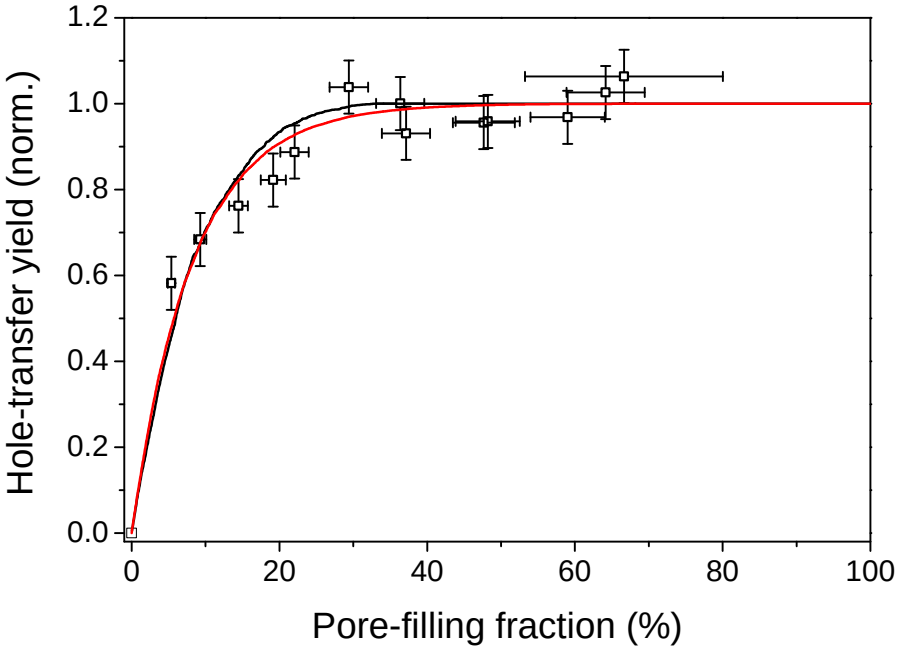

Figure 4.6: Normalized yield of hole transfer from dye cation to spiro-OMeTAD obtained by applying Eq. 4.2 to the data displayed in Fig. 4.4 averaged over the time interval of 1-2 μs. The solid lines are a fit to the data using a simple infiltration model assuming conformal coating (black) and random placement (red) of spiro-OMeTAD molecules onto the pore walls and the possibility for lateral "dye-hopping" of the hole prior to transfer to spiro-OMeTAD.

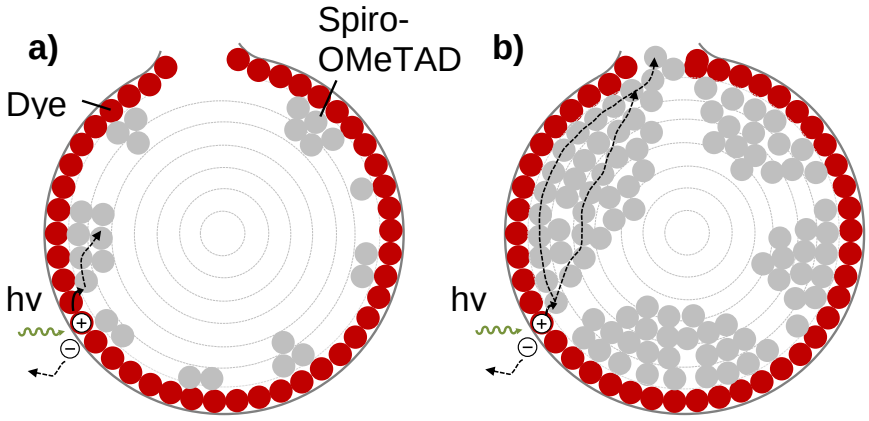

Figure 4.7: Cross-sectional sketch of an idealized pore within the TiO_2 network containing a monolayer of dye (red circles) and randomly distributed spiro-OMeTAD molecules (grey circles) attached to the surface. The grey dashed lines indicate the different layers of spiro-OMeTAD while the black dashed lines mark possible diffusion pathways of the photogenerated hole. a) Low pore-filling fraction: A complete pathway does not exist and the hole is thus not able to escape out of the pore. b) High pore-filling fraction: a sufficient number of spiro-OMeTAD molecules have infiltrated into the pore to form a percolation path allowing the hole to escape. The diffusion path length depends on the number of layers that have reached percolation threshold. Due to the shape of the pore, higher layers will provide a shorter pathway and subsequently increase the probability of the hole to escape before recombination occurs.

fraction, as extracted from the early-time transient absorption signals using Eq. 4.2. For very low PFFs, a rapid increase of the hole-transfer yield is visible, however, beyond a PFF of 30% no further significant changes are observed. This trend can be understood by considering the infiltration process of spiro-OMeTAD into an idealized pore of the TiO_2 network coated by a monolayer of dye, as schematically shown in Fig. 4.7. It is reasonable to assume that for the yield of hole transfer from the dye to the infiltrated HTM, only the surface coverage provided by the first monolayer of HTM will matter. The fraction of HTM molecules contained in this first layer for a completely filled pore (100% PFF) is calculated to be 33%, using a spiro-OMeTAD density [154, 215] of $1.02\,\mathrm{g\,cm^{-3}}$ and an average TiO_2 pore diameter d_{pore} of 20 nm [216]. In this simple model, the HTM takes up a cubic cell of volume $2\,\mathrm{nm^3}$ with a side length of 1.26 nm. The projected area of the dye is assumed to be $1.7\,\mathrm{nm^2}$, identical to that of the very similar dye Z907 [224]. Two main factors will determine how the hole-transfer yield depends on PFF, which are the HTM layer morphology created as the pores are filled, and the extent to which lateral hole-hopping from one dye molecule to another occurs prior to hole transfer to the HTM. The very simplest model in terms of analytical effort would assume conformal coating (i.e. each HTM layer is completed before the next one is allowed to form) and absent lateral dye-to-dye hole-hopping. In accordance with the presented calculation above, this case would require a PFF of 33% to achieve complete hole transfer, which happens to be in close agreement with the experimentally observed yield saturation at ∼30% PFF. However, given that significant diffusion within such dye sensitizer monolayer has in fact been observed, [214] and considering the amorphous nature of spiro-OMeTAD [225, 226] this model seems to be somewhat too simplistic and diffusion within the dye before hole transfer occurs will need to be taken into account.

The exact film formation of spiro-OMeTAD within a TiO_2 pore is unknown, hence the aim is to approximate reality by the use of three simplified model scenarios which can be compared against each other for their effectiveness in reproducing the experimental data sets. These cases rely on the relative effects of surface tension and surface energy minimization at the wall of a nanopore. In the first case, HTM molecules are free to move around after initial attachment to the pore wall until an overall potential minimum has been found; in

addition, a HTM molecule prefers to stick to itself more than to the pore wall - as a result, spheres or pseudo spheres form. In the second case, HTM molecules are again free to move around after initial attachment to the pore wall, however the HTM prefers to stick to the pore wall more than to itself; conformal coating results. For the third case, HTM molecules do not move around significantly after initial attachment to the pore wall, i.e. HTMs enter the pore and stick somewhere random. The first case can be ruled out on the basis of a previous study, showing that surface tension of solution-dropped spiro-OMeTAD on a TiO_2 surface is low [148]. The experimentally observed hole-transfer yields for the remaining two cases have been followed as follows. For the case of conformal coating, molecules will coat the inner surface of the pore first. Once the entire surface is covered with spiro-OMeTAD, the subsequent molecules settle in the second layer on top of the first one. This process is repeated until the pore is filled completely, and simulated through a Monte Carlo approach. Random infiltration, on the other hand, leads to simultaneous filling of several layers, which is modeled by molecules assuming a random position available at the surface. This position may hence be directly at the dye monolayer, or, in case that this specific surface position is already covered by a spiro-OMeTAD molecule, on top of the existing molecule to contribute to a second, third or subsequent layer, as shown in Fig. 4.7. A Monte Carlo simulation is proposed for each case to estimate the resulting percentage p(PFF) of the dye surface covered with spiro-OMeTAD molecules for different PFFs: A spiro-OMeTAD hole-transporter molecule settles inside the pore by assuming a randomly selected position at the inner surface sites. In the case of conformal coating, it settles in the lowest layer which is not completely filled yet. If this position is already occupied with another spiro-OMeTAD molecule, the molecule diffuses to a random adjacent position until a free position is found and settles there. The Monte Carlo simulation based on these assumptions is run to fill successive sites up to the point where a certain fraction of total available sites in the pore is filled, which corresponds to the pore-filling fraction (PFF). For this given simulated distribution of spiro-OMeTAD, the fractional occupancy of each spiro-OMeTAD layer can then be directly calculated, as shown in 4.8. The fractional dye coverage in spiro-OMeTAD, p(PFF), as used to describe the hole transfer yield from dye to spiro-OMeTAD, here corresponds to the result obtained

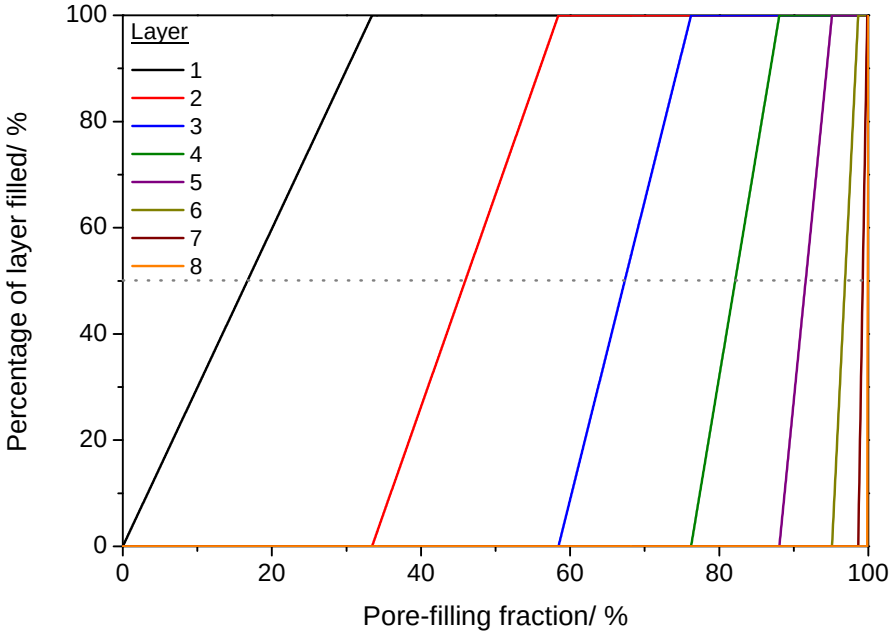

Figure 4.8: Simulated fractional occupancy of each spiro-OMeTAD layer in a pore with a 20 nm diameter assuming conformal coating. The dotted grey line indicates the pore-filling fraction at which 50% of layer is filled with spiro-OMeTAD.

for Layer 1.

For the case of random placement, the initial position of the molecule may be directly at the dye monolayer, or, in case that this specific surface position is already covered by a spiro-OMeTAD molecule, on top of the existing molecule to contribute to a second, third or subsequent layer. As each successive layer contains fewer positions than the previous one and a direct mapping between layers is thus not possible, it is assumed that the number of available surface sites in each layer above the first layer is given by the difference between the number of infiltrated molecules in the previous layer and the number of already infiltrated molecules in this layer. If the number of infiltrated molecules in the previous layer exceeds the maximum possible number of molecules in the current layer, it is given by the difference between the maximum possible number of molecules in the current layer and the number of already infiltrated molecules in this layer. The fractional occupancy of each spiro-OMeTAD layer for this model can then be seen in 4.9.

In case of absent lateral hole-hopping, the hole-transfer yield would be equal to the simulated surface coverage. However, lateral dye hole-hopping is likely to be particularly

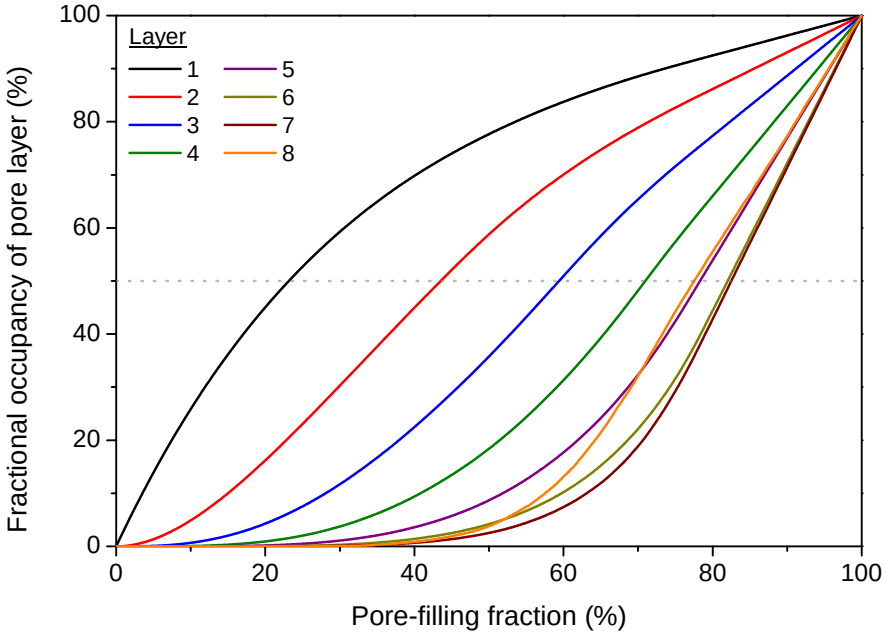

Figure 4.9: Simulated fractional occupancy of each spiro-OMeTAD layer in a pore with a 20 nm diameter assuming random placement of the molecules. The dotted grey line indicates the pore-filling fraction at which 50% of layer is filled with spiro-OMeTAD.

significant for devices with very low PFFs and can be taken into account by considering the average number $n(t)$ of distinct dye molecules a hole is able to visit within a given time t between its creation and transfer to the HTM. In the case of the random placement model, from a simple statistical consideration of the hole hopping process (see Appendix A.1) it is hence found that the expected hole-transfer yield η_{ht} depends on $p(\mathrm{PFF})$ and $n(t)$ through

$$\eta_{\mathrm{ht}}(\mathrm{PFF}) = 1 - [1 - \mathrm{p(PFF)}]^{\mathrm{n(t)+1}}. \tag{4.5}$$

where it is assumed that $n(t)$ is much smaller than the number of possible spiro-OMeTAD molecules in the surface layer. Since the fractional dye coverage in HTM ($p(\mathrm{PFF})$) is already determined from the Monte Carlo simulation, the number $n(t)$ of dye molecules visited by the hole can be extracted by fitting Eq. 4.5 to the experimental data shown in Fig. 4.6. For the conformal coating model the hole-transfer yields have to be extracted from a Monte Carlo simulation. Taking these assumptions, it is found that the best fits are achieved for both models using a value of n=3. This results in a mean-squared displacement of approximately $5.5 \times 10^{-14}\,\mathrm{cm}^2$ for a random hole walk. Using the equation $<\mathrm{r}^2> = 4Dt$, a diffusion

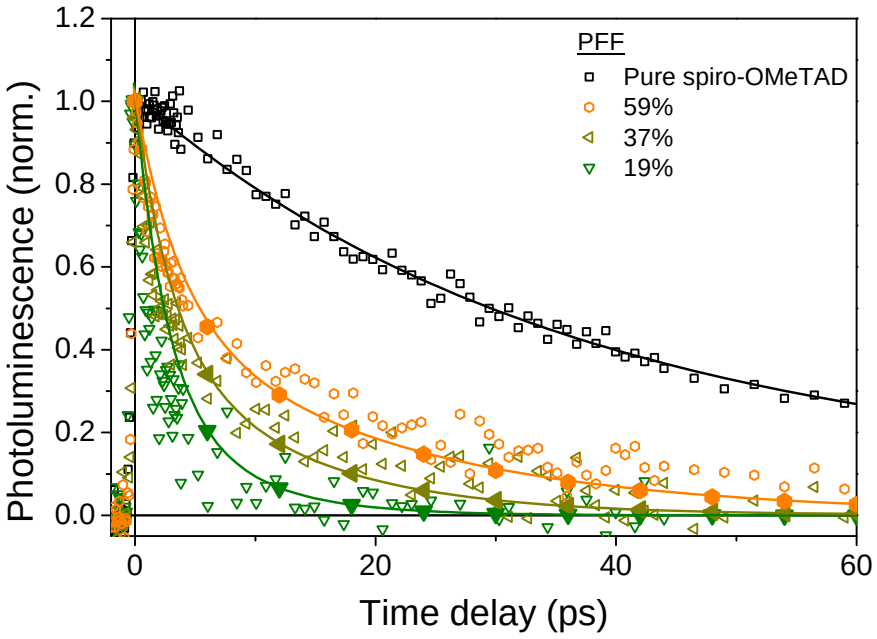

Figure 4.10: Femtosecond photoluminescence upconversion dynamics (hollow symbols) of TiO_2/C106/spiro-OMeTAD samples with varying pore-filling fractions at a detection wavelength of 430 nm (spiro-OMeTAD emission). An excitation wavelength of 400 nm with a fluence of 30 nJ cm^{-2} was used preferentially exciting the spiro-OMeTAD molecules. The solid symbols show the results of a Monte Carlo simulation using random placement of spiro-OMeTAD molecules as described in the text, with the connecting solid lines as a guide to the eye. The measurements were taken by Christopher Menelaou.

coefficient D of 6.8×10^{-9} cm^2/s is derived. This value is in very reasonable agreement with a comparison value [214] of 4.1×10^{-9} cm^2/s from previous studies of hole diffusion through a layer of Z907, a dye very similar to C106. Comparing the resulting simulated dependencies of the hole-transfer yield on PFF (Fig. 4.6) it is found that only small differences are visible between the two infiltration models. Hence the simulation indicates that the resulting hole-transfer yield and the extracted extent of dye-dye hopping appear to be robust with respect to the exact choice of infiltration process. These results and simulations suggest that because of dye-dye hole-hopping, hole transfer to the HTM can be completed even for low PFFs within only a few μs, which is several times faster than the competing half-reaction time of the recombination process ($\sim$160 μs). For even lower PFF, complete hole transfer might still be possible, if the required time for hole hopping on the dye is sufficiently shorter than $\sim$160 μs. It is noted here that inter-dye hole-hopping is likely to play a critical role in polymer HTM based DSSCs, where good operation with PFFs as low as 7% have been observed [145].

While simulations of the hole-transfer yield were relatively unrevealing of spiro-OMeTAD morphology onto the surface of the pore, an alternative set of spectroscopic measurements was performed by Christopher Menelaou to be analysed here which is directly sensitive not only to the arrangement of the first HTM monolayer on the dye, but also probes the presence of higher layers. In these femtosecond photoluminescence upconversion (PLUC) experiments, excitons are uniformly photo-excited in the spiro-OMeTAD molecules and diffuse through the network until they either recombine or come in proximity to the dye surface where they undergo energy or charge transfer. The lifetime of the photogenerated excitons will therefore depend on the structure of the spiro-OMeTAD network and can be compared to determine whether a conformal coating or a random infiltration model is more appropriate. For low PFFs, excitons will be generated close to the surface and thus be quenched quickly. In contrast, for high PFFs the average distance from exciton position to dye network will be larger, resulting in a longer lifetime.

Fig. 4.10 shows the photoluminescence emitted from pore-infiltrated spiro-OMeTAD following its preferential excitation at 400 nm. A clear dependence of the exciton recombination lifetime in spiro-OMeTAD on the PFF can be seen. Also shown are the results of a Monte Carlo simulation based on the previously introduced model of random infiltration providing the structure of the spiro-OMeTAD network. Exciton dynamics are simulated using typical assumptions [209–211]: In the first step, excitons are placed on random spiro-OMeTAD molecules within the network. Migration is then modeled using a random walk to one of the neighbouring molecules. If an interface between dye and spiro-OMeTAD is reached, perfect quenching is assumed. In contrast, if the exciton reaches a non-quenching interface, perfect reflection occurs. To account for the natural recombination life time of excitons, the simulated results were multiplied with the fitted decay response of a sample containing only spiro-OMeTAD. Using these assumptions and a hopping rate of 6 ps between two spiro-OMeTAD molecules, the simulated PL decay curves for the random placement model show excellent correspondence with the experimentally measured exciton population dynamics. In the case of a conformal coating model, however, all samples with a PFF below 33%, i.e. the PFF at which the surface layer is fully covered and higher layers would just begin to fill up,

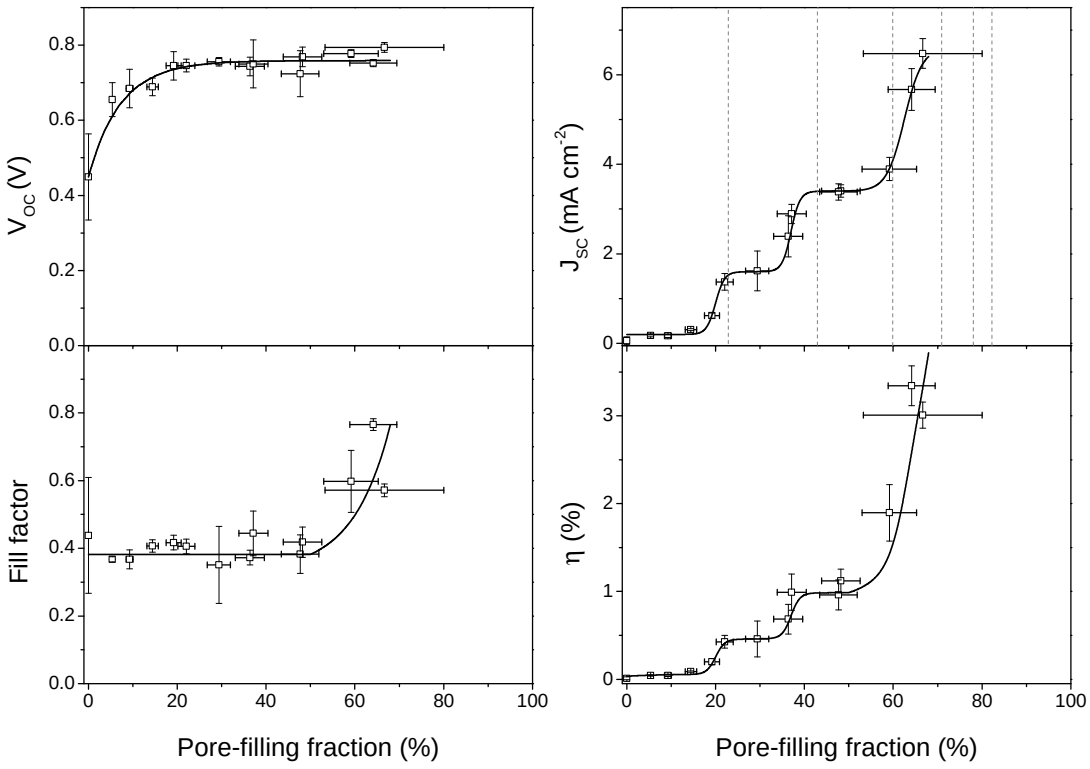

Figure 4.11: Characterization data for complete sDSSC devices as a function of pore-filling fractions. Top left: Open-circuit voltage (V_{oc}). Top right: Short-circuit current (J_{sc}). Bottom left: Fill factor. Bottom right: Power-conversion efficiency (η). The solid lines are guides to the eye. The dashed lines in the figure showing the short-circuit current indicate the expected positions of the onsets of the increases in short-circuit current as predicted by percolation theory. Results are averaged over 5-6 devices and error bars for V_{oc}, J_{sc}, fill factor, and η reflect the standard deviation. These devices contain additives tBP and Li-TFSI, whose concentration was held constant in the solution, rather than with respect to the spiro-OMeTAD concentration, in order to ensure constant charge injection across all devices.[169–172] All device measurements were taken by Derek J. Hollman.

are expected to show the same dynamics. This lies in contrast to the experimentally found dynamics and suggests that a substantial amount of spiro-OMeTAD molecules is present in higher layers before the surface layer is fully covered. These experiments suggest that the model of random successive site selection of spiro-OMeTAD molecules entering the pore is the more suitable model of the two extreme examined cases. This tends to suggest that while in reality some molecular re-arrangement may well occur, minimization of the overall energy associated with the HTM arrangement appears to be incomplete in these nanopores. We hence conclude that while the reality may lie between the two extreme cases of random HTM placement and conformal coating, the former describes the available data much better.

With such knowledge gained from spectroscopic insights on the HTM distribution it is now highly interesting to determine the effects on photovoltaic device performance. Fig. 4.11 shows the dependence on PPF of the open-circuit voltage (V_{oc}), short-circuit current (J_{sc}), fill factor (FF), and power-conversion efficiency (η) for DSSCs matching the sets used for the spectroscopic investigations. As discussed earlier, the two main mechanisms influenced by the fraction of pore filling with HTM are the yield of hole transfer from the dye and the subsequent hole extraction through the HTM to the electrode. It is found that the open-circuit voltage V_{oc} shows the same dependence on the PFF as the hole-transfer yield (Fig. 4.6) suggesting a clear correlation between charge build-up in the HTM and increasing open-circuit voltage in the device. The fill factor, short-circuit current and power-conversion efficiency on the other hand, show different trends, including sharp increases at higher pore-filling fractions. The fill factor is constant up to a PFF of ∼60% and shows a sharp rise beyond this value. Interestingly, the short-circuit current and power-conversion efficiency display steps of superlinear increases with distinct onsets at PFFs of ∼20%, ∼37%, and ∼63%. These may be explained by considering that short-circuit current generation relies on efficient hole extraction, which requires a complete pathway through the spiro-OMeTAD network to the counter electrode. At low PFFs, isolated spiro-OMeTAD molecules as well as isolated clusters will exist preventing holes on these molecules from being extracted. Once higher PFFs are achieved spiro-OMeTAD molecules will be in close enough proximity to enable diffusion of the holes to the counter electrode as illustrated schematically in Fig. 4.7.

The step-like increases of photocurrent with PFF can be understood from percolation theory [227] considering a network where each position is randomly filled with a molecule according to a certain probability. Here, a "critical probability" p_c or ratio of unfilled to filled positions exists, beyond which diffusion through the entire network is possible from almost any molecule within the network and below which such percolation becomes almost impossible. Thus, at PFFs below p_c negligible short-circuit current is expected, whereas beyond p_c the value of the short-circuit current should display a sharp photocurrent onset as observed. The occurrence of several such onsets, as seen in Fig. 4.11, can be explained by considering the specific random infiltration process that leads to successive layer build-up.

For holes to have the possibility to diffuse out of the pore, only the surface layer needs to reach the critical ratio p_c since it will then offer a complete path from each starting position to the counter electrode. Due to the random infiltration process, p_c is first reached in this surface layer and hence the first onset with PFF will originate from this layer. Once the second layer reaches p_c, an additional sharp onset in photocurrent ought to be expected because this layer offers a better pathway to holes than the first, for two reasons. First, the holes migrating through higher layers will spend more time further away from the TiO_2:dye surface which reduces their probability of recombination with electrons in the TiO_2, and second, due to the curved shape of the pore the path length to the counter electrode will be reduced for such higher layers, as indicated in Fig. 4.7. For analogous reasons, onsets are expected to occur every time the critical ratio p_c is reached in a forming, higher-lying layer.

The experimental observations of photocurrent onsets show that up to the achieved PFF of 67% three successive layers of spiro-OMeTAD reach percolation threshold. The observed photocurrent onsets can be compared with theoretical expectations from percolation theory assuming that completely occupied spiro-OMeTAD layers can be approximated by a 2-dimensional lattice in which each molecule is surrounded by six adjacent molecules to which a hole can be transferred to. For this case the critical ratio p_c can analytically be found [228] to be 0.5, i.e. 50% of the positions in a layer would need to be filled with spiro-OMeTAD to create sufficient percolation pathways for holes. The PFFs for which these thresholds are reached can be determined from the results of the Monte Carlo simulation of layer build-up through placement of molecules at random positions, as discussed earlier and shown in Supporting Information. It is found that for the given pore size of 20 nm, percolation pathway completions should theoretically occur at 23%, 43% and 60% for the first (surface), second and third layer away from the dye interface, respectively. These values are in good agreement with the experimentally found onsets of the photocurrent at ∼20% ∼37% and ∼63% PFF. Deviations from the experimental data may be caused by non-idealized shapes and diameters of the pores, systematic errors of the PFF measurement, and deviations of the actual spiro-OMeTAD arrangement from the idealized assumptions of entirely random infiltration. Formation of pathways between previously isolated pores or clusters of pores

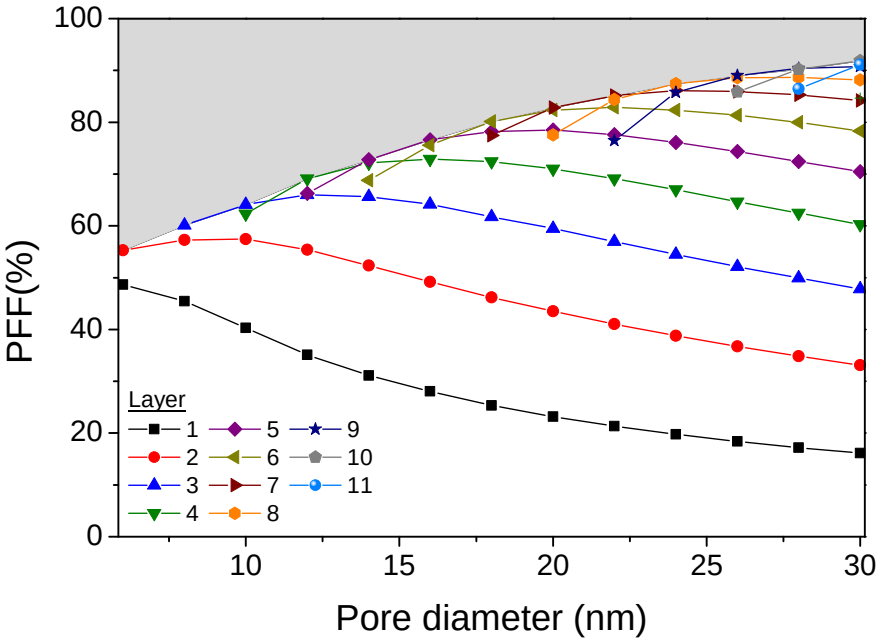

Figure 4.12: Simulated pore-filling fractions at which an onset of the short-circuit current is expected, as derived from percolation theory predicting pathway formation when 50% of a layer is occupied with spiro-OMeTAD molecules. The solid lines are a guide to the eye. The shaded area indicates the PFF range for which no further improvement of the short-circuit current is expected because the percolation threshold for the highest available layer in the pore has already been reached.

within the TiO_2 network might also influence charge collection.

Given the good agreement of photocurrent onsets with predictions from percolation theory, the theoretical predictions that may be gained from this simple model may now be explored. For example, while higher PFFs than ∼67% could not be accessed experimentally here, additional onsets are expected at 71%, 78%, 82% and 83% PFF. Thus, beyond 83% PFF, no further significant increases of the short-circuit current would be expected, as this represents the threshold at which the last layer fitting into the pore reaches percolation threshold. Interestingly, changing the pore size in the TiO_2 network would be expected to change the position of these photocurrent onsets. This effect can be simulated by again using the simple Monte Carlo simulation of random successive positioning of HTM on the pore surface. Fig. 4.12 shows the calculated PFF required to reach a 50% occupancy of available positions in a given layer as a function of pore diameter. Within this description, each line is expected to contribute to a rise in associated photocurrent for a given pore size and hence the

highest available layer envelope will define the PFF beyond which no further photocurrent increases are to be expected. Fig. 4.12 demonstrates that for pores with a 30 nm diameter the last onset in photocurrent is expected at 92% PFF, while for a 10 nm size pore the last onset would occur at 64% PFF. Conceptually, the increase in the highest percolation threshold onset with increasing pore size can be understood considering that for a small pore fitting just one monolayer of HTM, a 50% PFF would be sufficient to reach the envelope line. For a pore fitting two layers on the other hand, the second layer would have 50% coverage which, by the successive infiltration process, would yield a first layer with coverage higher than 50% and hence the total PFF required for the second onset would be higher than 50%. For these reasons, the PFF at which the highest percolation threshold occurs will generally increase with pore size. Due to the possibility of non-random infiltration at higher layers or non-idealized pore shapes, however, the absolute value of the overall PFF required to reach percolation threshold in all layers might in reality deviate slightly from the model. The simple model hence predicts that tuning the pore size may be an important tool to achieve optimized short-circuit current in cases where the PFF is limited, such as for devices with higher TiO_2 layer thicknesses.

4.3 Conclusion

In conclusion, the dependence of dye regeneration and charge collection on the pore-filling fraction (PFF) in dye-sensitized solar cells was studied by a combined approach employing spectroscopic and device performance measurements. Using microsecond transient absorption spectroscopy, it was found that the yield of hole transfer from the dye sensitizer to spiro-OMeTAD hole transporter increases rapidly with increasing pore-filling fractions but saturates at ∼30% PFF. Simple models were proposed to describe filling of the dye-sensitized TiO_2 pores with focus on the two extreme cases. It was simulated (i) successive build-up of spiro-OMeTAD molecules that attach to random positions on the pore wall or an already attached spiro-OMeTAD molecule, if present and (ii) conformal coating in which the lowest layer is always filled first. It was shown that for both coating types for the pore walls in

spiro-OMeTAD, the experimentally determined hole-transfer yield suggest that holes located on dye molecules must undergo lateral hole-hopping, visiting on average 3 dye molecules before transferring to spiro-OMeTAD. As a result, only a relatively small pore-filling fraction is required to achieve efficient hole transfer from dye sensitizer to spiro-OMeTAD hole transporter. The validity of both pore-infiltration models were further experimentally examined by using femtosecond photoluminescence transient spectroscopy in which spiro-OMeTAD is directly excited and the quenching of its re-emission caused by charge or energy transfer to the dye is observed. This technique is highly sensitive to the layer build-up of HTM inside the pore as it determines the time scales on which excitations generated in a random spiro-OMeTAD molecule can diffuse to the dye:spiro-OMeTAD interface. Applying a simple Monte Carlo approach to simulating such excitation transfer based on the random infiltration model gives excellent agreement with data. The conformal coating model, on the other hand, is incompatible with the observed slowing of the PL transients at a low PFF threshold, for which it does not predict the presence of secondary layers. These experiment suggest that the HTM molecular build-up on the pore walls is relatively random and HTM molecules may not have the facility to move until the overall positioning energy is minimized. The findings obtained from spectroscopic measurements were subsequently correlated with performance data for complete solar cell devices. It was found that the open-circuit voltage saturates around ∼30% PFF, closely following the dependence of hole-transfer yield on the PFF and suggesting a correlation between charge build-up in the HTM and increasing open-circuit voltage. In contrast, the short-circuit current and power-conversion efficiency show steps of super-linear increases with distinct onsets at PFFs of ∼20%, ∼37%, and ∼63%. It was demonstrated that these thresholds correspond to PFF values at which formation of percolation pathways would theoretically be expected to occur for the lowest three layers of spiro-OMeTAD coating the pore walls in the way described by the proposed random infiltration model. Percolation theory for a two-dimensional lattice of molecules in triangular arrangement predicts relatively sudden formation of continuous pathways at 50% occupancy hence explaining the onset of photocurrent at the observed PFFs. The observation of multiple onsets in the photocurrent also demonstrates that layers further away from the dye:TiO_2

must offer better charge routes out of the pore, possibly because they are shorter by geometry, but also because they offer routes further away from an interface at which charge recombination may occur. The proposed simple model of random pore filling predicts that the PFF required for a complete percolation pathway in the outermost layer of spiro-OMeTAD, and hence the PFF beyond which no further enhancement in photocurrent is to be expected, should increase with increasing pore diameter. These findings offer a new level of understanding of the pore infiltration mechanism in solid-state dye sensitized solar cells and its effect on the overall performance of these devices through both sensitizer regeneration and charge transport towards the electrodes.

Chapter 5

Optimizing the Energy Offset Between Dye and Hole-Transporting Material in Solid-State Dye-Sensitized Solar Cells

The work presented in this chapter has been published in:

C. T. Weisspfennig, M. M. Lee, J. Teuscher, P. Docampo, S. D. Stranks, H. J. Joyce, H. Bergmann, I. Bruder, D. V. Kondratuk, M. B. Johnston, H. J. Snaith, and L. M. Herz Optimizing the Energy Offset Between Dye and Hole-Transporting Material in Solid-State Dye-Sensitized Solar Cells *The Journal of Physical Chemistry C*, **117** (39), 19850–19858, 2013.

5.1 Introduction

As discussed in Chapter 4, dye-sensitized solar cells (DSSCs) employing cobalt complex redox mediators have achieved power-conversion efficiencies in excess of 12% [115]. In contrast, solid-stated DSSCs have only reached values of up to 7.2% [16, 17]. It has been proposed that incomplete filling of the pores and the low charge carrier mobility of spiro-OMeTAD on the order of $10^{-4}\,\mathrm{cm}^2\,\mathrm{V}^{-1}\mathrm{s}^{-1}$ are the limiting factors, leading to the difference in power-conversion

efficiencies [15, 116, 148, 149]. Next to improving these factors, it may also be possible to increase the efficiency of solid-state HTMs by minimizing the loss-in-potential, which is approximately the difference between the optical band-gap of the photoactive semiconductor divided by the charge of an electron, and the open-circuit voltage (V_{OC}) [6]. Reducing the energy offset between the HOMO levels of dye and HTM would thus result in a smaller loss-in-potential and an increased open-circuit voltage. While the heterogeneity of the energy levels requires a certain offset to efficiently drive the hole-transfer process [18, 229], spiro-OMeTAD might still leave room for improvement. The best performing solid-state DSSCs haven an approximate loss-in-potential of 0.72 eV [14]. In contrast, it is estimated that an over-potential of 0.2 eV should be sufficient for near-unity hole regeneration [6].

In this chapter, three novel triarylamine type hole-transporting materials with similar, but varying HOMO levels are compared to spiro-OMeTAD to systematically explore the possibility of reducing the over-potential and improving the power-conversion efficiency. Using transient absorption spectroscopy, and employing the standard ruthenium sensitizing dye Z907 [230], it is shown that all devices based on the new HTMs performed worse than those incorporating spiro-OMeTAD. While the difference for two of the novel HTMs can be explained by a lower hole-transfer yield, one HTM shows a hole-transfer yield of approximately 100% and hence other factors must play a role. Using Scanning Electron Microscopy (SEM) imaging, it is demonstrated that all HTMs reach a similar and sufficiently high pore-filling fraction and it is concluded that observed differences in power-conversion efficiency are not caused by inferior pore filling. Instead, transient photovoltage-photocurrent measurements show that the new HTMs induce a shift of the TiO_2 surface potential towards higher values leading to less efficient electron transfer from sensitizer to TiO_2. Overall, this study shows that changes in molecular design of the HTM can have a complex impact on charge transfer from the dye sensitizer, both for transfer of holes to the HTM and electrons to the TiO_2 electrode.

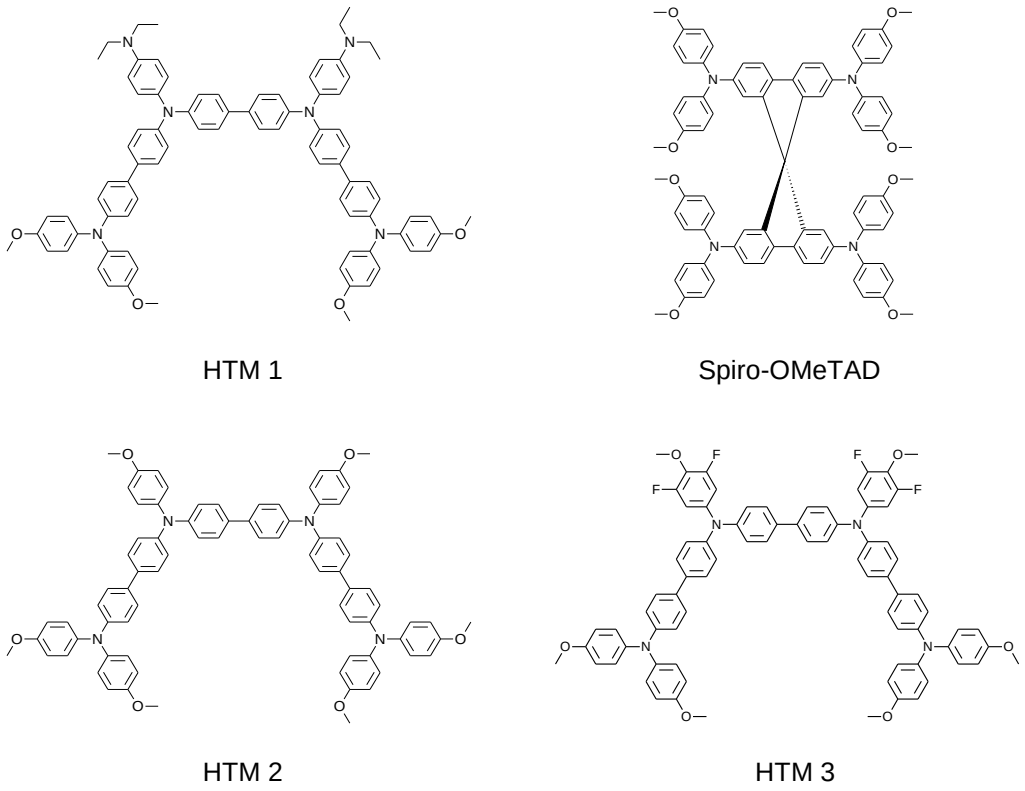

Figure 5.1: Chemical structures of the hole-transporting materials HTM **1-3** provided by BASF SE, and the currently most widely employed HTM, spiro-OMeTAD, which is used as a reference in this study.

5.2 Results and Discussion

5.2.1 Material Properties

Fig. 5.1 shows the chemical structures of the three novel hole-transporting materials N^4,$N^{4'}$-([1,1'-biphenyl]-4,4'-diyl)bis(N^4-(4-(diethylamino)phenyl)-$N^{4'}$,$N^{4'}$-bis(4-methoxyphenyl)- [1,1'-biphenyl]-4,4'-diamine) (**1**), N^4,$N^{4'}$-([1,1'-biphenyl]-4,4'-diyl)bis(N^4,$N^{4'}$,$N^{4'}$-tris(4-methoxyphenyl)-[1,1'-biphenyl]-4,4'-diamine) (**2**), and N^4,$N^{4'}$-([1,1'-biphenyl]-4,4'-diyl)bis(N^4-(3,5-difluoro-4-methoxyphenyl)- N^4,$N^{4'}$-bis(4-methoxyphenyl)-[1,1'-biphenyl]-4,4'-diamine) (**3**) which were provided by BASF SE. Additionally, spiro-OMeTAD is shown which acts as a reference. HTM **1** differs from HTM **2** in that two methoxy groups were substituted by diethylamine groups. HTM **3** was derived from HTM **2** by fluorination of both carbon atoms ortho to the methoxy groups on two of the phenyl rings. All HTMs employ methoxy groups which

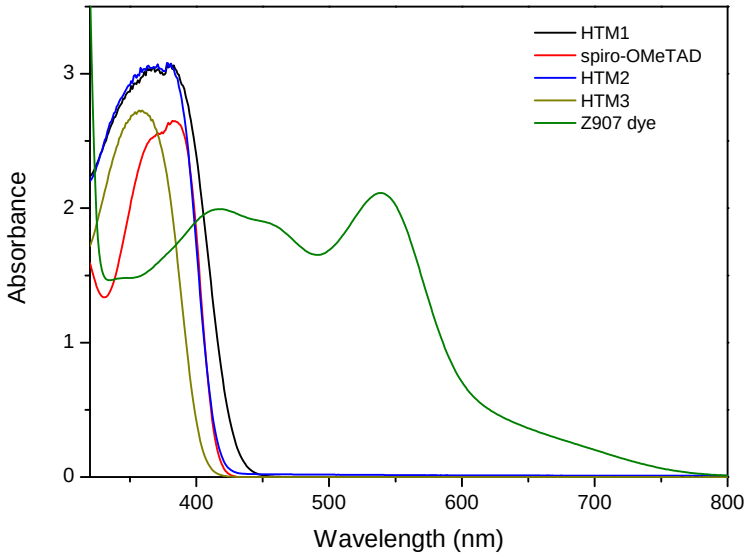

Figure 5.2: UV-VIS absorption measurements of all hole-transporting materials employed in this study with a concentration of $4 \cdot 10^{-4}$ M, as well as the dye Z907 with a concentration of $1.7 \cdot 10^{-4}$ M.

Table 5.1: Characteristics of the hole-transporting materials used in this study. $E_{\mathrm{HOMO}}(eV) = -1.4\,E_{\mathrm{onset,ox}}(V) - 4.6$ [232], where $\mathrm{E_{onset,ox}}$ was determined by solution-based cyclic voltammetry [233]. The optical bandgap E_{opt} was calculated from the absorption onset of the compound in solution.

HTM	**Mol. weight (g/mol)**	$\mathbf{E_{HOMO}}$ **(eV)**	**Over-potential (eV)**	$\mathbf{E_{opt,gap}}$ **(eV)**
HTM 1	1237.57	-4.26	0.70	3.07
Spiro	1225.43	-4.52	0.44	2.99
HTM 2	1155.38	-4.67	0.29	2.97
HTM 3	1227.34	-4.77	0.19	2.88
Z907 dye	870.10	-4.96 [234]		1.48

have a high tendency to stabilize the radical cations due to their steric effect [231]. Fig. 5.2 shows the UV-VIS absorption spectra of all HTMs as well as the dye Z907.

Table 5.1 shows the characteristics of the aforementioned materials. HOMO levels were determined by solution-based cyclic voltammetry using the relationship $E_{\mathrm{HOMO}}(eV) = -1.4\,E_{\mathrm{onset,ox}}(V) - 4.6$ [232], as shown in Fig. 5.3-5.6. All materials have a similar molecular weight, but differ in their HOMO energy levels. Comparing these to the dye Z907, the HTMs have an over-potential between 0.70 and 0.19 eV which is driving the hole-transfer process, although shifts in the dye oxidation potential of about 0.1-0.3 eV due to the adsorption to

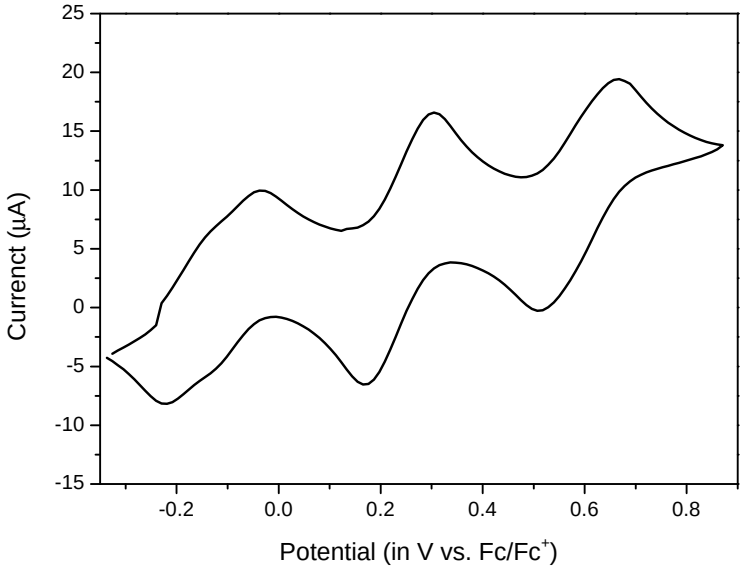

Figure 5.3: Cyclic voltammetry of dissolved HTM **1** 1.7×10^{-3} M in a solution of 0.1 M tetrabutylammonium hexafluorophosphate in dichloromethane. The scan rate was $100\,\mathrm{mVs^{-1}}$. The measurement was taken in collaboration with D. V. Kondratuk.

the TiO_2 surface are possible [18, 235, 236]. Assuming a minimum required over-potential of 0.2 eV [6], it is expected that all HTMs, with the exception of HTM **3**, have a large enough energy difference for hole-transfer yield close to unity. The over-potential of HTM **3** is approximately equal to the estimated minimum and could therefore result in incomplete hole transfer.

5.2.2 Device Data

Table 5.2 summarizes the photovoltaic performance parameters for all HTMs in the presence of and in the absence of the standard additives 4-*tert*-butyl pyridine (tBP) [166] and lithium bis(trifluoromethylsulfonyl)imide salt (Li-TFSI) [169]. While devices employing the new HTMs show a power-conversion efficiency close to zero in absence of the additives, spiro-OMeTAD reaches a value of about 1.3%. In presence of the additives, the efficiency of all devices increases substantially with a significant increase in the short-circuit current J_{SC} for all devices, in agreement with previous studies on liquid-electrolyte and solid-state DSSCs [122, 165, 166, 222, 223]. HTM **3** performed worst out of all devices and might have

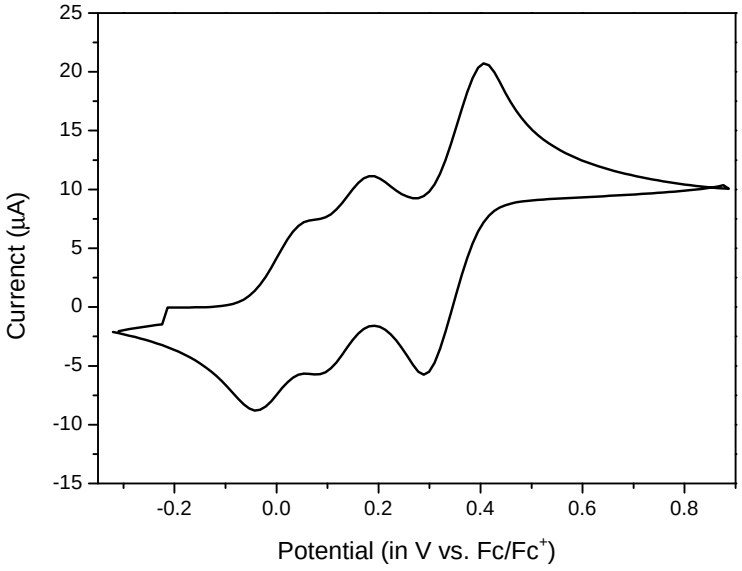

Figure 5.4: Cyclic voltammetry of dissolved spiro-OMeTAD 1.7×10^{-3} M in a solution of 0.1 M tetrabutylammonium hexafluorophosphate in dichloromethane. The scan rate was $100\,\mathrm{mVs^{-1}}$. The measurement was taken in collaboration with D. V. Kondratuk.

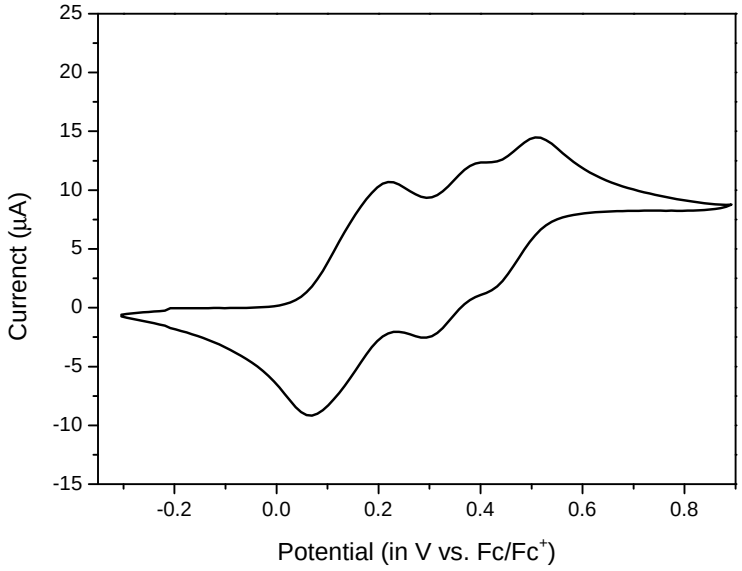

Figure 5.5: Cyclic voltammetry of dissolved HTM **2** 1.8×10^{-3} M in a solution of 0.1 M tetrabutylammonium hexafluorophosphate in dichloromethane. The scan rate was $100\,\mathrm{mVs^{-1}}$. The measurement was taken in collaboration with D. V. Kondratuk.

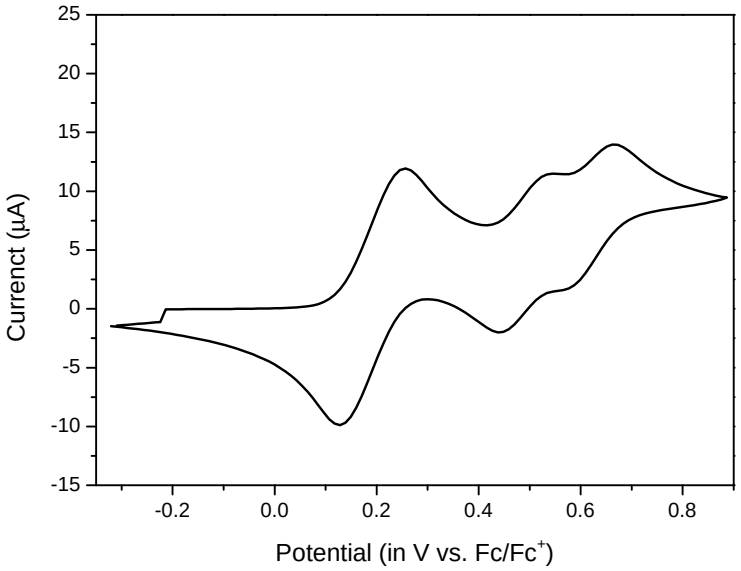

Figure 5.6: Cyclic voltammetry of dissolved HTM **3** 1.5×10^{-3} M in a solution of 0.1 M tetrabutylammonium hexafluorophosphate in dichloromethane. The scan rate was $100\,\mathrm{mVs^{-1}}$. The measurement was taken in collaboration with D. V. Kondratuk.

Table 5.2: Photovoltaic performance parameters for the studied hole-transporting materials. η: Power-conversion efficiency, V_{OC}: Open-circuit voltage, J_{SC}: Short-circuit current, FF: Fill factor. Results are presented for devices with and without the standard additives 4-*tert*-butyl pyridine (tBP) and lithium bis(trifluoromethylsulfonyl)imide salt (Li-TFSI). The measurement was performed by M. M. Lee.

HTM	$\eta(\%)$	$\mathbf{V_{OC}}$(V)	$\mathbf{J_{SC}}$(mA cm^{-2})	**FF**
HTM 1	0.01	0.56	0.13	0.11
spiro	1.26	0.65	3.28	0.59
HTM 2	0.00	0.44	0.01	0.17
HTM 3	0.08	0.63	0.49	0.25
HTM 1 + add.	1.40	0.70	3.99	0.50
spiro + add.	3.10	0.68	6.15	0.74
HTM 2 + add.	1.68	0.75	3.93	0.57
HTM 3 + add.	0.47	0.68	1.08	0.64

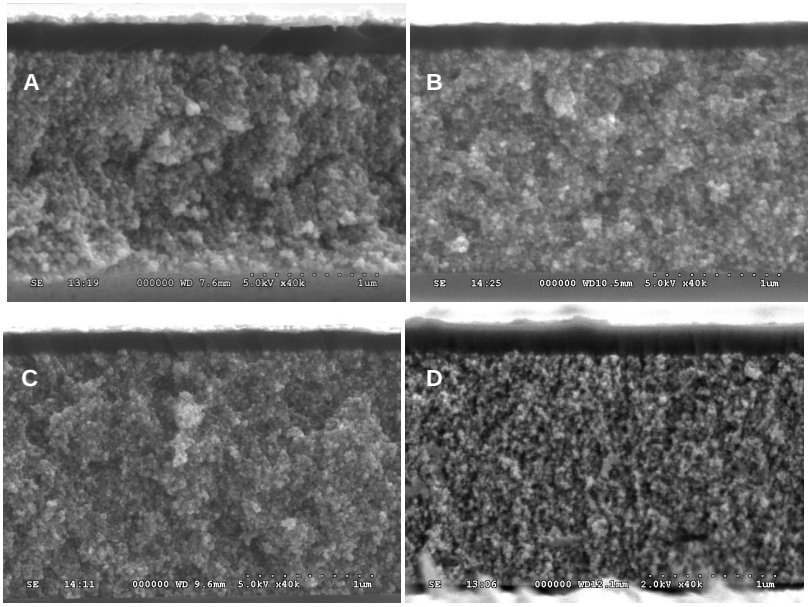

Figure 5.7: SEM images of devices consisting of TiO_2/Z907 and the hole-transporting material (A) HTM **1**, (B) spiro-OMeTAD, (C) HTM **2**, and (D) HTM **3**. The measurement was taken in collaboration with H. J. Joyce.

insufficient over-potential to drive the hole transfer process. Additionally, the efficiency of all new HTMs remained systematically below the efficiency of spiro-OMeTAD, with and without additives. When comparing the correlation and variation in power-conversion efficiency to that of the HOMO levels, no clear dependence is visible. This suggests that other parameters beyond the energy offset might play an important role for the efficiency.

5.2.3 Pore Filling

To determine the reason for the non-systematic dependence on the HOMO level and the difference between the new HTMs and spiro-OMeTAD the pore-filling fractions of all devices were compared. As previously discussed, incomplete filling of the mesoporous network with the HTM is a limiting factor for the device performance [157, 215]. There are two reasons for this: Firstly, it hinders a complete regeneration of the dye in areas where no HTM molecules are present at the dye interface. Secondly, it prolongs the percolation path of the holes to the electrode therefore increasing the recombination probability [148].

Several methods have been proposed to estimate the pore-filling fraction [154, 156, 213,

215]. In one of these methods, the concentration of HTM in the porous network is estimated by adding the concentration in the pores before evaporation, which is given by the initial volume concentration c of the HTM solution, to the increase in concentration due to infiltration of HTM during the evaporation process [154]. The increase in concentration is calculated from the difference in HTM on top of the device before and after evaporation, divided by the volume of the pores given by the porosity p and the TiO_2 thickness d. While the amount of HTM on top of the device before evaporation can be calculated by the thickness d_{sol} of the solution and the concentration c, the amount of HTM after evaporation is given by the thickness d_{cl} of the capping layer. The pore-filling fraction is then given by [154]

$$\mathrm{PFF} = c + \frac{d_{sol}c - d_{cl}}{dp}. \tag{5.1}$$

To measure the thickness d_{cl} of the capping layer SEM images of all devices were taken, as shown in Fig. 5.7. d_{sol} has been measured to be $6.9 \pm 0.5\,\mu$m for spiro-OMeTAD [215], and is assumed to be the same for all materials in this study. Using these values combined with a value of 49 ± 1 % [215] for the porosity p and a concentration c of 10%, the pore-filling fractions are estimated to be between 60% and 70% for all HTMs. Thus, no correlation between pore-filling fraction and device efficiency is observed for the given samples. Since a pore-filling fraction of approximately 60% is estimated to be sufficient for optimized performance, it is concluded that incomplete pore filling is not the main factor responsible for the differences in the power-conversion efficiency [215].

5.2.4 Hole Transfer

Next, photoinduced absorption spectroscopy was used to study the efficiency of the hole-transfer process. To do this, a solution of each HTM with nitrosonium tetrafluoroborate ($NOBF_4$) was chemically oxidized first, as shown in Fig. 5.8 (a), to determine the absorption spectra of the radical cations. Spiro-OMeTAD has been well studied in the past and its radical cation spiro-OMeTAD$^+$ and its diradical cation spiro-OMeTAD^{2+} are known to show

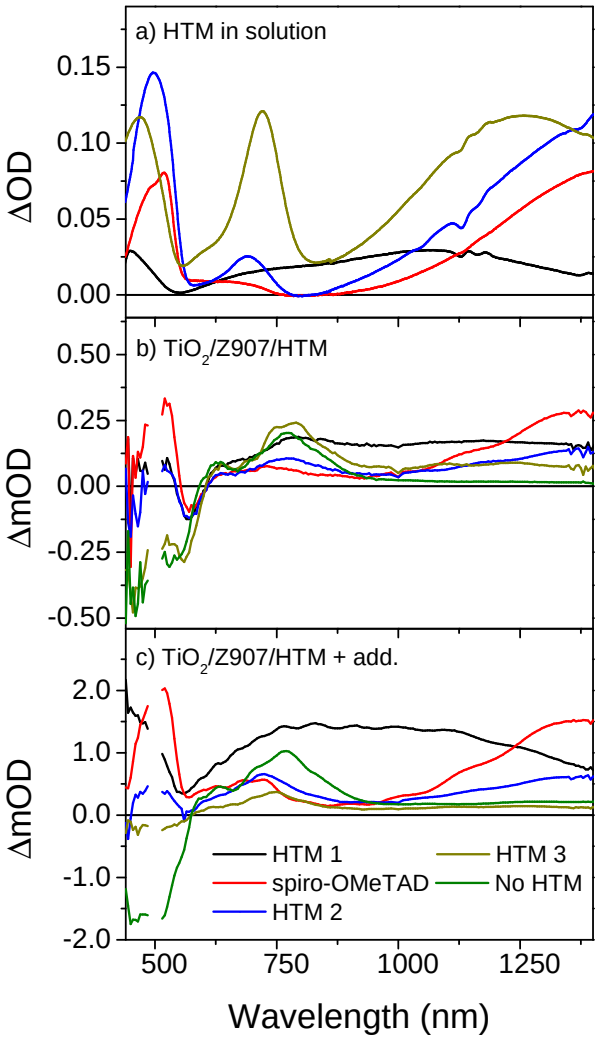

Figure 5.8: (a) UV-VIS spectra of each hole-transporting material in acetonitrile and chlorobenzene (1:1) chemically oxidized with nitrosonium tetrafluoroborate ($NOBF_4$) at a molar ratio of 35%. (b) Photoinduced absorption spectra of TiO_2/Z907 samples with each hole-transporting material and a reference sample without a hole-transporting material. c) Photoinduced absorption spectra of TiO_2/Z907 samples with each hole-transporting material prepared with the standard additives 4-*tert*-butyl pyridine (tBP) and lithium bis(trifluoromethylsulfonyl)imide salt (Li-TFSI) and one reference sample without a hole-transporting material. All samples were photoexcited at a wavelength of 496.5 nm. Measurements (b) and (c) were taken in collaboration with J. Teuscher and S. D. Stranks.

indistinguishable spectra with a peak around 511 nm and a shoulder around 700 nm, as well as a broad peak in the near infrared [146, 154, 217, 237]. Both HTM **2** and HTM **3** show similar peaks in comparison to spiro-OMeTAD, although the peak around 700 nm is stronger for HTM **3**. In contrast, HTM **1** shows a very broad peak spanning from the visible to the near-infrared.

With the absorption spectra of the radical cations known, the photoinduced absorption spectra of complete samples, which are shown in Fig. 5.8 (b), can be interpreted. For a sample containing no HTM a negative feature is observed below 570 nm. This is attributed to photobleaching of the ground-state absorption of the dye caused by the presence of neutral or charged species [238, 239]. For samples which include a HTM, the negative feature becomes smaller once hole-transfer from the dye to the HTM occurs as the photobleaching is reduced. Additionally, the signal is overlayed with the absorption of the radical cation on the HTM, as determined in Fig. 5.8 (a). For all samples except the one containing HTM **3** hole transfer can be observed. Fig. 5.8 (c) shows the results for samples with additives. An increase in absorbance is visible for all HTMs at their respective absorption peaks. This indicates an increase in their long-lived charge density, except for HTM **3** which shows only a small change, in line with the previously observed small improvement of the power-conversion efficiency for the device (see Table 5.2). The poor efficiency of devices incorporating HTM **3** is therefore caused by the lack of long-lived radical cations on the hole-transporting material due to either fast recombination or poor hole-transfer yield.

To confirm these findings and to determine quantitatively the hole-transfer yield, the hole-transfer dynamics were measured using transient absorption spectroscopy. In this measurement, the dye is excited at a wavelength of 550 nm as it coincides with an absorption peak of Z907 and an absence of absorption from spiro-OMeTAD. The sample is then probed at 520 nm since all HTMs show absorption from the radical cations at this wavelength. Fig. 5.9 shows the pico- to nanosecond and micro- to millisecond dynamics. The initial negative signal is attributed to the photobleaching of the dye, whereas the ensuing signal is attributed to the absorption of radical cations on the HTM as well as the reduction of the photobleach-

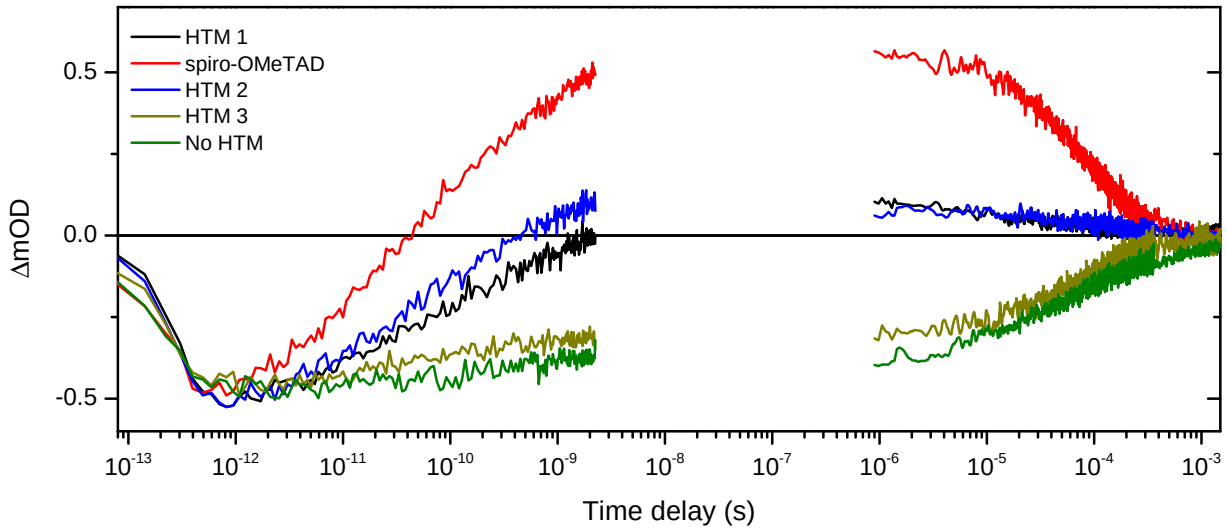

Figure 5.9: Transient absorption measurements of TiO_2/Z907 samples with the hole-transporting materials HTM **1** (black), spiro-OMeTAD (red), HTM **2** (blue), and HTM **3** (dark yellow) excluding additives and at a probe wavelength of 520 nm. Additionally, a TiO_2/Z907 sample without a hole-transporting material (green) is used as a reference. Measurements of samples with additives were omitted due to stability reasons. The samples were photoexcited at 550 nm with a fluence of 50 μJ/cm^2. The micro- to millisecond transient absorption dynamics were scaled by a factor of 1.14 to allow for better comparison. The mismatch in the amplitude between the two time regimes is likely to be caused by a variation in fluence due to the use of two different experimental setups.

ing. The hole-transfer dynamics for spiro-OMeTAD show comparable dynamics to previous results in the literature where cis-RuL_2(SCN)$_2$ (where L is 4,4'-dicarboxy-2,2'-bipyridyl) was employed as a dye [146]. HTM **3** shows almost the same dynamics as the reference sample which does not have a HTM. Thus, very little hole transfer is present between Z907 and HTM **3**. In contrast, for HTM **1** and HTM **2** a hole-injection process is clearly visible. Extrapolating the dynamics into the nano- to microsecond range, all HTMs complete the hole-transfer process within approximately 10 nanoseconds. Recombination, on the other hand, is not visible until approximately 2 μs. The time window between 1-2 μs can therefore be used to calculate the hole-transfer yields.

To relate the signal strength to the hole-transfer yield, the molar extinction coefficient of the HTMs ($\epsilon_{\mathrm{HTM}^+}$) and the dye ($\epsilon_{\mathrm{dye}^+} - \epsilon_{\mathrm{dye}^0}$) need to be taken into account. The extinction coefficient of the ground state of Z907 at 520 nm has been found [239] to be approximately 12000 L mol^{-1} cm^{-1}. In a careful study using chemical oxidation, as shown in Fig. 5.10-

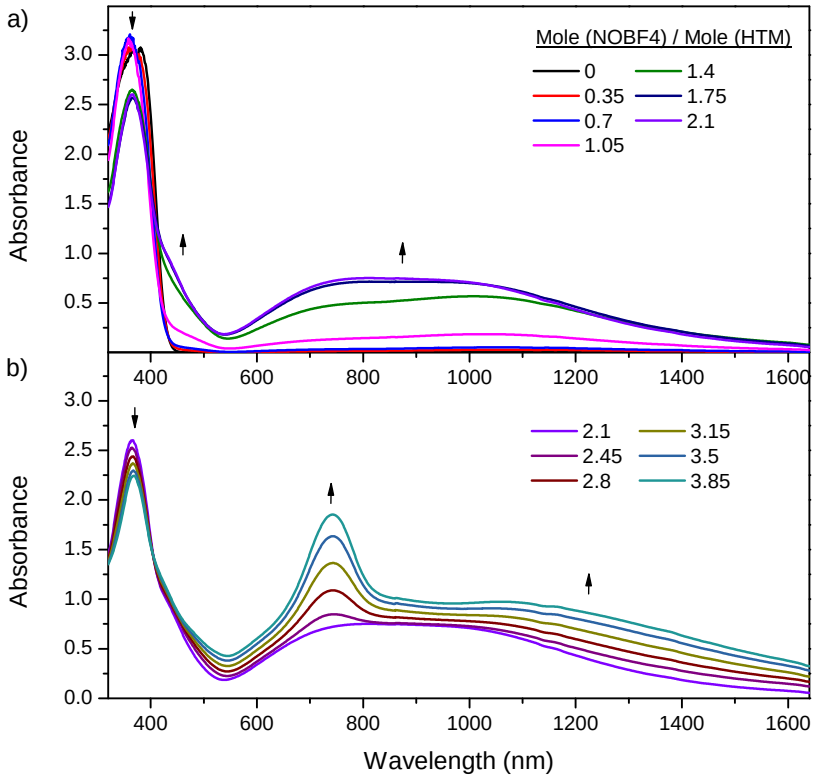

Figure 5.10: Stepwise chemical oxidation of 4×10^{-4} M HTM **1** in acetonitrile and chlorobenzene (1:1) with increasing amounts of $NOBF_4$: (a) From HTM $\mathbf{1}^0$ over HTM $\mathbf{1}^+$ to HTM $\mathbf{1}^{2+}$, (b) from HTM $\mathbf{1}^{2+}$ towards higher oxidized states.

5.14, the extinction coefficients of the spiro-OMeTAD radical cation were determined to be approximately 26800 L mol^{-1} cm^{-1} at 520 nm, slightly higher than a previous value in the literature [240]. For HTM **1-3** the molar extinction coefficients at 520 nm are 2800, 20300, and 7400 L mol^{-1} cm^{-1}, respectively.

The hole-transfer yield is then calculated by comparing the signal strength of the ground-state bleaching (ΔOD_{dye}) to the signal strength of the sample with the HTM between 1 and 2 μs (ΔOD): [18, 146, 157]

$$\text{Yield} = \left(1 - \frac{\Delta OD}{\Delta OD_{dye}}\right)\left(1 + \frac{\epsilon_{HTM^+}}{\epsilon_{dye^+} - \epsilon_{dye^0}}\right)^{-1} \tag{5.2}$$

For spiro-OMeTAD, a value of approximately 75% is calculated [241]. For HTM **1-3** it is

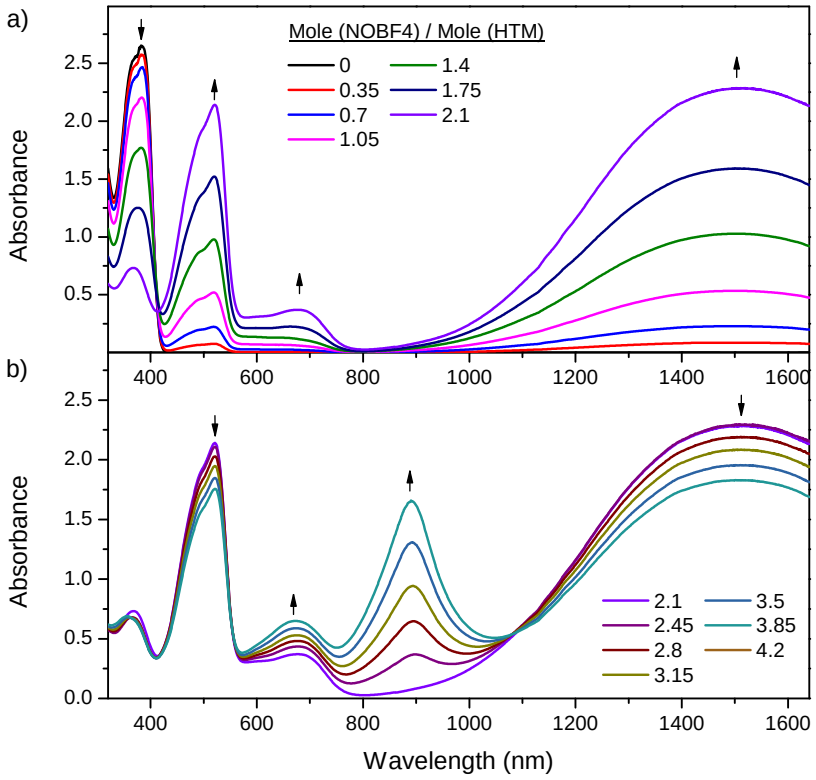

Figure 5.11: Stepwise chemical oxidation of 4×10^{-4} M spiro-OMeTAD in acetonitrile and chlorobenzene (1:1) with increasing amounts of $NOBF_4$: (a) From spiro-OMeTAD^0 over spiro-OMeTAD$^+$ to spiro-OMeTAD^{2+}, (b) from spiro-OMeTAD^{2+} towards spiro-OMeTAD^{4+}.

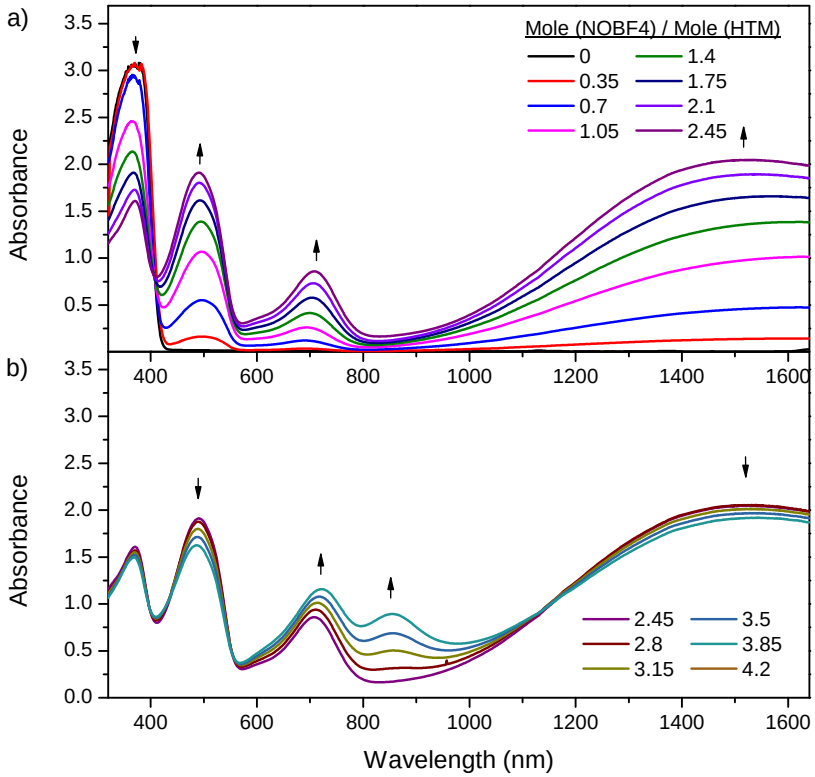

Figure 5.12: Stepwise chemical oxidation of 4×10^{-4} M HTM **2** in acetonitrile and chlorobenzene (1:1) with increasing amounts of $NOBF_4$: (a) From HTM $\mathbf{2}^0$ over HTM $\mathbf{2}^+$ to HTM $\mathbf{2}^{2+}$, (b) from HTM $\mathbf{2}^{2+}$ towards higher oxidized states.

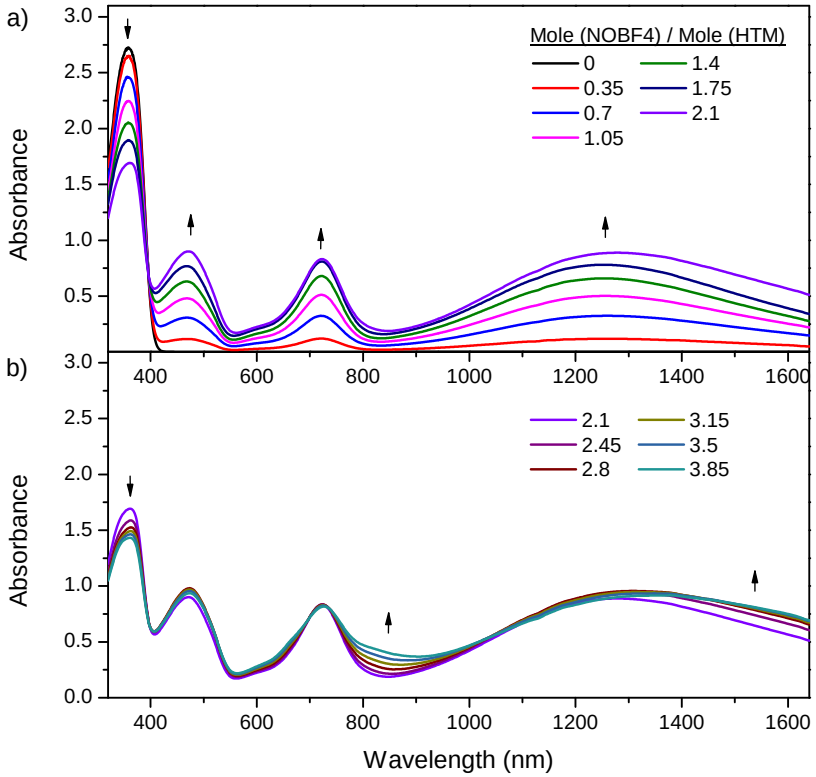

Figure 5.13: Stepwise chemical oxidation of 4×10^{-4} M HTM **3** in acetonitrile and chlorobenzene (1:1) with increasing amounts of $NOBF_4$: (a) From HTM $\mathbf{3}^0$ over HTM $\mathbf{3}^+$ to HTM $\mathbf{3}^{2+}$, (b) from HTM $\mathbf{3}^{2+}$ towards higher oxidized states.

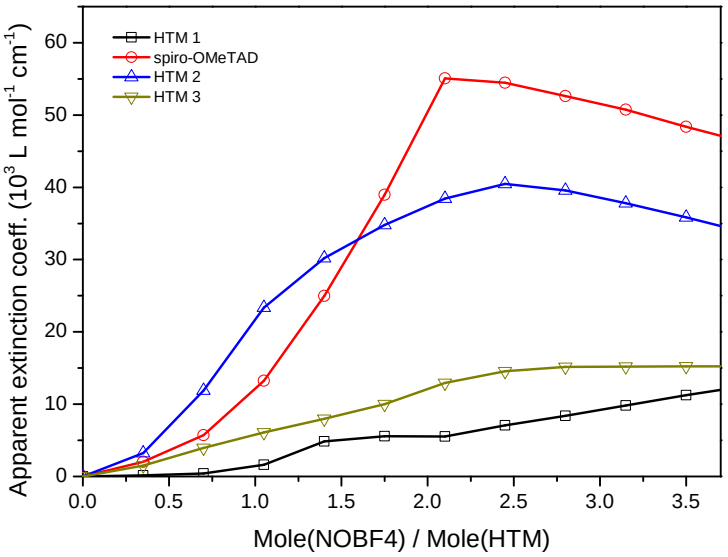

Figure 5.14: Stepwise chemical oxidation at 520 nm of the four different hole-transporting materials for varying concentrations of $NOBF_4$. A decrease in the signal is seen once the molecules go from a 2+ excited state towards higher oxidized states.

estimated that hole-transfer yields of approximately 100%, 46%, and 12%, respectively (see Fig. 5.15).

These hole-transfer yields can be related to the HOMO level of the HTM, as shown in Fig. 5.15. Quantitatively, the dependence is given by the homogeneous thermodynamic equilibrium of holes in the HTM and in the dye [18]. However the results are much broader than what would be expected in this model. Haque *et al.* [18] suggested that the dependence is influenced by inhomogeneous broadening of the energy levels due to local variations in the energetics of the TiO_2/dye/HTM interface. Using this assumption, the data can be fitted with a midpoint of -4.63 eV and a full width at half maximum (FWHM) of 0.33 eV, slightly lower than the value found in the aforementioned study. The midpoint of the fit is shifted by 0.33 eV compared to the HOMO level of Z907 (-4.96 eV [242]). This might be due to several reasons such as shifts in the dye oxidation potential resulting from adsorption to the TiO_2 surface [18, 235, 236] or differences in the cyclic voltammetry measurement techniques such as mismatches in the cyclic reference value for F_{c+}/F_c. Using the results from the model of inhomogeneous broadening, it can be seen that the energy offset between the dye Z907

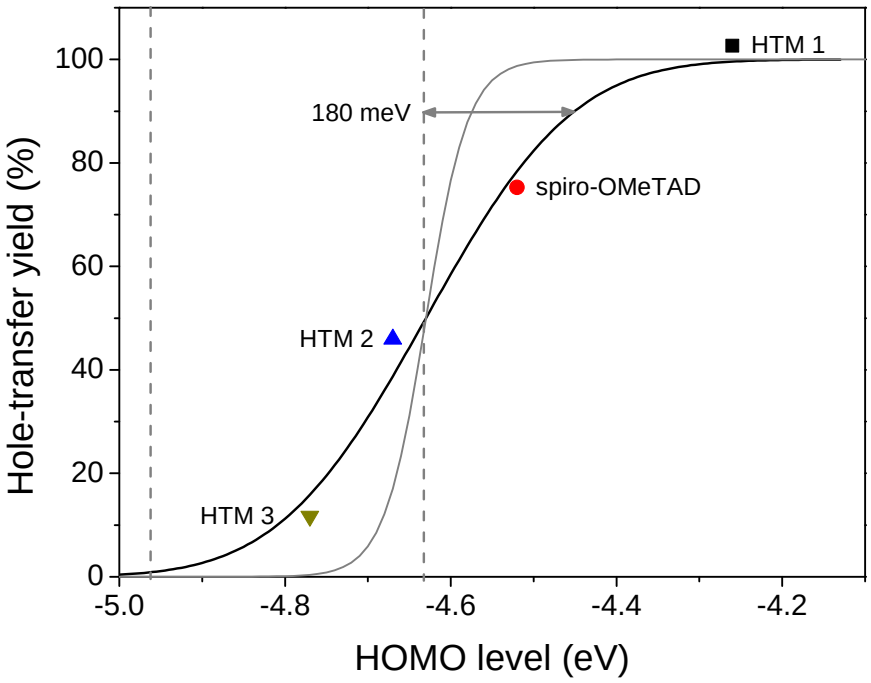

Figure 5.15: Dependence of the hole-transfer yield on the HOMO level of the hole-transporting material. The solid grey line is a fit assuming an inhomogeneous broadening, while the solid black line is a fit to the data based on a model assuming a Gaussian distribution for the local energy offsets between dye and hole-transporting material [18]. The grey dashed lines indicate the position of the Z907 HOMO level (-4.96 eV [242]) and the midpoint of the fit (-4.63 eV).

and spiro-OMeTAD is close to optimal. Only small improvements of the power-conversion efficiency of solid-state DSSCs employing ruthenium based dyes are therefore expected when the HOMO level of the HTM is increased to deeper potentials. It is also estimated that an over-potential of approximately 180 meV should be sufficient to achieve a 90% efficient hole transfer. However, the intrinsic difficulties in determining the exact position of the energy levels of Z907 in the solid sensitized electrode leave quite significant ambiguity in the absolute energy alignment of dye and HTM HOMO levels. For example, the energy level alignment between the dye and the HTM may shift considerably upon physical contact, e.g. as a result of ground-state charge transfer. Hence, while Fig. 5.15 provides an excellent picture of the changes with relative variation in HOMO level of the HTM, the absolute positioning of these energy levels will need to be determined with a higher degree of accuracy in future studies.

5.2.5 Charge Extraction

The hole transfer yields obtained for the different HTMs with the device short circuit currents are now compared in order to assess whether charge extraction may also play a significant role on the overall device performance. The transient absorption experiments show that the deeper HOMO level of HTM **3** causes spiro-OMeTAD to have a 6.3 times higher hole-transfer yield than HTM **3**. Notably, the short-circuit current of the device containing spiro-OMeTAD is approximately 5.8 times higher than the device containing HTM **3**, as shown in Table 5.2. Since the short-circuit current is proportional to the hole-transfer yield and the difference in the power-conversion efficiency between the two devices is largely caused by different short-circuit currents, it can be concluded that the poor performance of HTM **3** is mainly due to a very low hole-transfer yield between the dye and the HTM. Similarly, spiro-OMeTAD has a 1.6 times higher short-circuit current than **2** and shows a 1.6 times higher hole-transfer yield. The poor device performance of HTM **2** can thus be partially attributed to a reduced hole-transfer yield. HTM **1**, on the other hand, shows a higher hole-transfer yield than spiro-OMeTAD. The lower power-conversion efficiencies must therefore be due to other factors. To determine whether the inferior performance might be caused by a reduced

charge-collection efficiency on the HTM or a negative influence of the electron injection into the TiO_2, small-perturbation transient photovoltage-photocurrent measurements were performed for devices illuminated with red light [243, 244]. The charge-collection efficiency through HTM **1**, HTM **2**, and spiro-OMeTAD was observed to be the same, as shown in Fig. 5.16, and hole collection therefore cannot be responsible for the measured variations in device efficiency. In contrast, as can be seen in Fig. 5.17, when measuring the capacitance as a function of the open-circuit voltage, a clear shift of ∼300 meV for the devices containing HTM **1** and HTM **2** is observed in comparison to the device containing spiro-OMeTAD. Such increase in potential without significant change in the slope of the curve is consistent with a shift in the surface potential of the TiO_2. Such shifts will lower the density of states in the TiO_2 that are available for electron injection from the sensitizer [244]. It is thus concluded that electron injection is partially inhibited in devices containing HTM **1** and HTM **2** in comparison to spiro-OMeTAD resulting in a lower electron extraction and hence device efficiency. The observed shift in surface potential may be caused either by direct interactions of the HTM with the TiO_2 electrode, or indirectly by the HTM arrangement, potentially due to crystallization of the HTM, influencing the distribution of ionic additives and thus creating a different ionic environment at the TiO_2 interface.

5.3 Conclusion

In summary, three novel triarylamine type hole-transporting materials with varying HOMO levels to spiro-OMeTAD were compared in order to explore the possibility of reducing the over-potential and improve the power-conversion efficiency. Using transient absorption spectroscopy, the hole-transfer yield of spiro-OMeTAD was estimated to be approximately 75% and further reduction in the energy offset would lead to a small hole-transfer yield. This result shows that the energy alignment of spiro-OMeTAD is already close to optimal for ruthenium-based dyes leaving only small room for improvement. However the use of alternative HTMs such as HTM **2** and HTM **3** may prove to be advantageous for dye sensitizers with slightly different energy levels leading to better device performance than could be

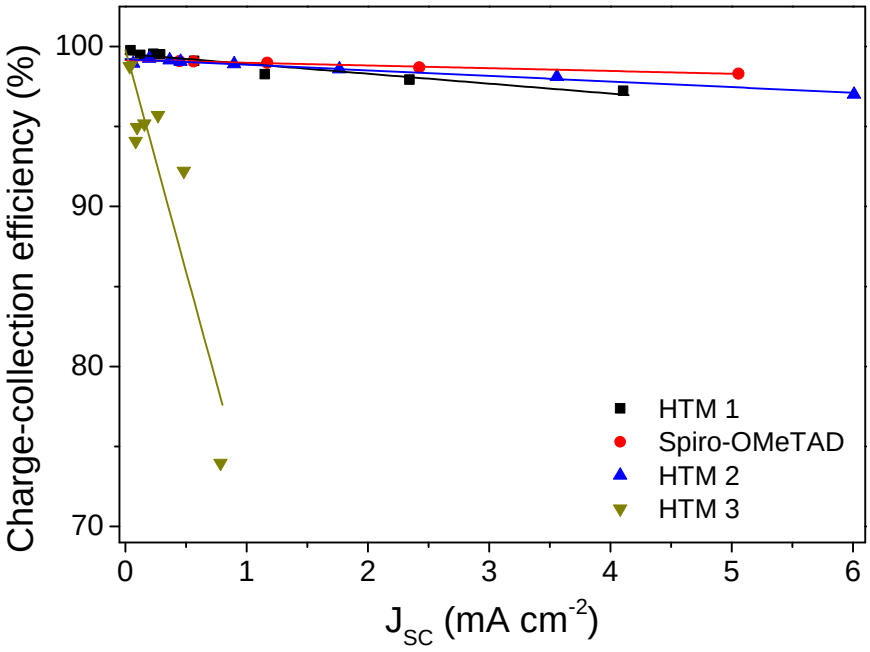

Figure 5.16: Charge-collection efficiency of each HTM for different short-circuit currents. The solid lines are a linear fit to the data. The measurement was taken by M. M. Lee.

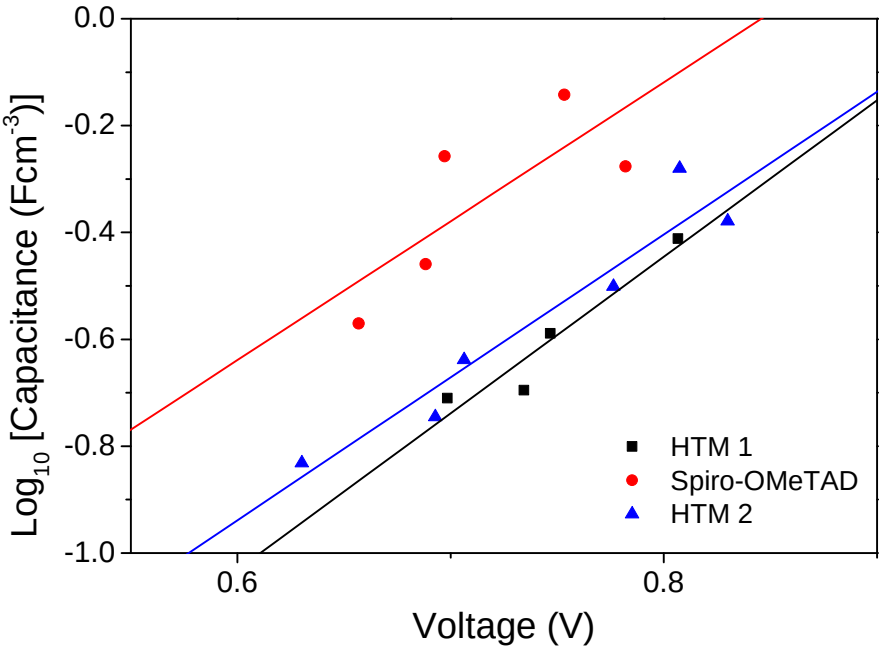

Figure 5.17: Capacitance measurements for HTM1, spiro-OMeTAD and HTM2. The solid lines are an exponential fit to the capacitance. The measurement was taken by M. M. Lee.

achieved when incorporating spiro-OMeTAD.

In addition, it was found that all devices incorporating one of the new HTMs ultimately performed worse than those utilizing spiro-OMeTAD. While the difference in power-conversion efficiency of HTM **2** and HTM **3** in comparison to spiro-OMeTAD can partially be attributed to a lower hole-transfer yield caused by a smaller energy offset, HTM **1** showed a 100% hole-transfer yield and hence other factors must play a role. Using SEM imaging, it was demonstrated that a pore-filling fraction of at least 60-70% is achieved by all HTMs and conclude that inferior pore filling is not limiting relative performance of devices incorporating the different HTMs. It was further shown that devices containing HTM **1** and HTM **2** exhibit a shift of the TiO_2 surface potential towards a higher value which is likely to partially inhibit electron transfer from the dye into the TiO_2 limiting electron collection and device performance. Overall, this study shows that optimization of new hole transporters for solid-state DSCs involves a complex interplay of factors, including energy-level optimization, HTM pore infiltration and HTM interactions with ionic additives and the TiO_2 surface.

Chapter 6

Ultrafast Charge Separation at a Polymer-Single-walled Carbon Nanotube Molecular Junction

The work presented in this chapter has been published in:

S. D. Stranks, C. Weisspfennig, P. Parkinson, M. B. Johnston, L. M. Herz and R. J. Nicholas. Ultrafast charge separation at a polymer–single-walled carbon nanotube molecular junction. *Nano Letters*, **11**:66–72, 2011. [245] Copyright 2011 American Chemical Society.

6.1 Introduction

Organic photovoltaic devices (OPV) are considered to be a low-cost alternative to silicon-based solar cells [116]. The majority of OPV devices utilise exciton dissociation at a type-II heterojunction between two materials, resulting in interfacial charge separation and free polarons in the materials. However, in many OPVs such as polymer-polymer blends, exciton dissociation often results in the formation of an interfacial bound charge pair termed an exciplex or charge-transfer exciton [246–250]. The exciplex is strongly bound and long-lived and therefore presents a major loss channel leading to low power-conversion efficiencies.

To improve the efficiency of OPVs, single-walled carbon nanotubes have been considered as an alternative material due to their high carrier-mobility, large aspect ratios, and controllable solubilization in polymer solutions [19, 20, 65]. Despite these properties, the power-conversion efficiencies of such devices has been poor so far [21, 23, 24, 251]. However, recent studies revealed that these results might have been caused by a lack of a type-II heterojunction and higher efficiencies might still be possible in presence of such heterojunctions [25, 252].

In this chapter, it is shown that charge dissociation across the interface between individually dispersed small-diameter SWNTs coated with a single layer of P3HT occurs on a timescale of approximately 430 fs. The so generated charge pairs either form a bound interfacial charge-transfer state or recombine non-radiatively within the nanotube and, thus, do not generate long-lived free polarons. After the addition of an excess P3HT network, however, long-lived charge separation is achieved on a scale comparable to that in P3HT-fullerene blends.

This is the first time, significant long-lived charge separation is observed in P3HT-NT blends. It is concluded that for efficient charge separation to occur, small diameter SWNT which form a type-II heterojunction with the polymer are required. Additionally, the SWNTs need to be embedded in a matrix of excess polymer to facilitate migration of the charges away from the interface and prevent recombination. These results explain the poor device performance of SWNT-polymer to date and lay a path for future developments of carbon nanotube-polymer organic photovoltaics.

6.2 Experimental Details

Sample preparation is based on the work of Schuettfort *et al.* [253] in which the synthesis of a highly purified nanohybrid structure consisting of a SWNT coated with a single layer of P3HT was presented. In these purified nanohybrids, the P3HT wraps around the carbon nanotube in a sheathlike morphology, aligned at an approximate angle of 48° with respect

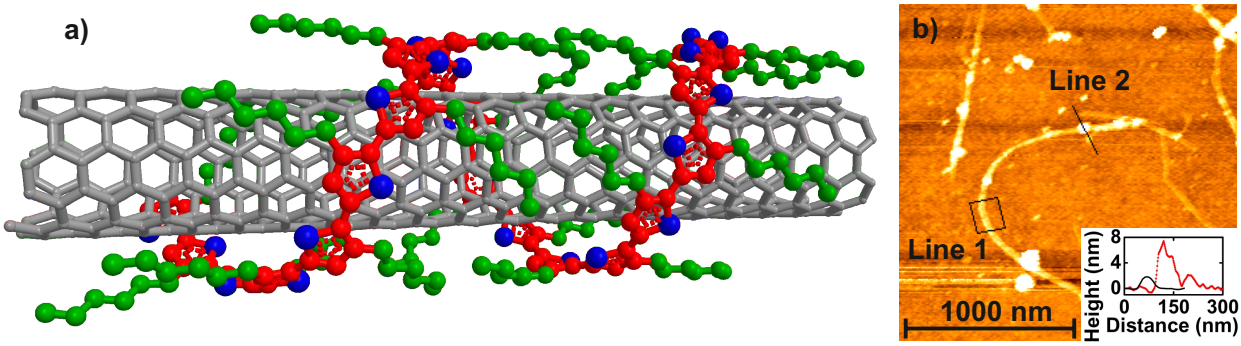

Figure 6.1: (a) Chemical structure of P3HT. (b) AFM image displaying isolated carbon nanotubes coated with sheath P3HT as well as scattered P3HT nanocrystals. Inset: Heights of the AFM slices Line 1 (black solid line) and Line 2 (broken red line) marked on the image. The measured height for Line 1 is consistent with carbon nanotube of diameters 0.7-0.9 nm coated with a single layer of P3HT. Similarly, the measured height for Line 2 is consistent with nanocrystals of typical dimensions 3-5 nm on the sheath. The AFM image was taken by Jack Alexander-Webber.

to the SWNT axis [254] and at a distance of twice the van der Waals radius (0.34 nm) from the nanotube [253]. Fig. 6.1 (a) shows a sketch of this structure. Also shown is an atomic force microscope (AFM) image in which P3HT nanocrystals of the size of 3-5 nm are visible.

Five samples are used in this study: A bulk P3HT as a control sample, a P3HT-NT nanohybrid samples, a sample referred to in the following as P3HT-NT(1%) consisting of an overall concentration of 1% SWNTs wrapped in a P3HT sheath surrounded by excess P3HT, or network P3HT. Additionally, a conventional 60:40 blend of P3HT:[6,6]-phenyl-C_{61}-butyric acid methyl ester (PCBM) and a sample of SWNTs embedded in an inert gelatin matrix were prepared to allow comparative studies. All samples in this study were prepared by Samuel D. Stranks.

Fig. 6.2 shows the UV-VIS absorption spectra of the five samples. The samples containing P3HT show the characteristic features observed for bulk P3HT with strong absorption in the region between 350-650 nm, while the samples containing SWNTs show the E_{11} transitions between 950-1350 nm. The NT-gelatin control sample shows the characteristic nanotube E_{22} transitions in the region between 400-800 nm. In agreement with photoluminescence excitation (PLE) map measurements, it can then be concluded that (6,5) carbon nanotubes are the dominant species in the films containing SWNTs. The amount of metallic

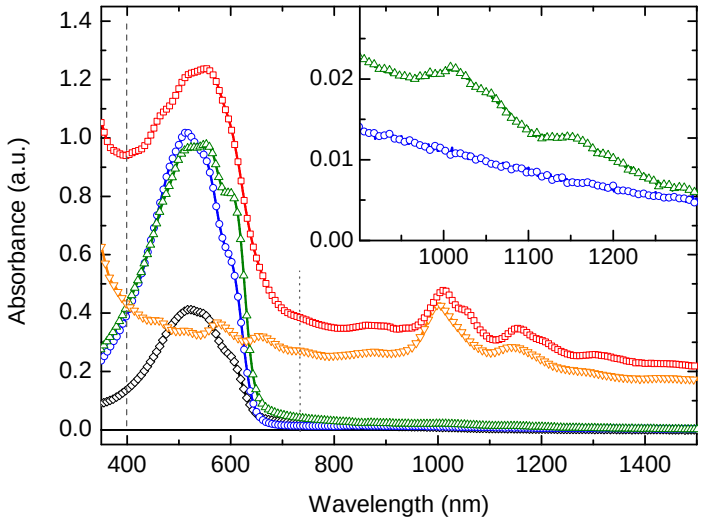

Figure 6.2: UV-VIS absorption spectra for P3HT (blue circles), P3HT-NT (red squares), P3HT-NT(1%) (green triangles), and P3HT-PCBM (black diamonds) samples as spun-cast on quartz, along with that for the gelatin-NT sample (orange inverted triangles). Additionally, the excitation wavelength (400 nm) is marked by a gray dashed vertical line, while the probe wavelength (730 nm) is marked by a gray dotted vertical line. Both, the P3HT-NT (red squares) and gelatin-NT sample (orange inverted triangles) show a non-zero absorbance at higher wavelengths due to the presence of metallic nanotubes. Inset: Region between 900-1300 nm showing the E_{11} nanotube peaks in the P3HT-NT(1%) sample. The measurement was performed by Samuel D. Stranks.

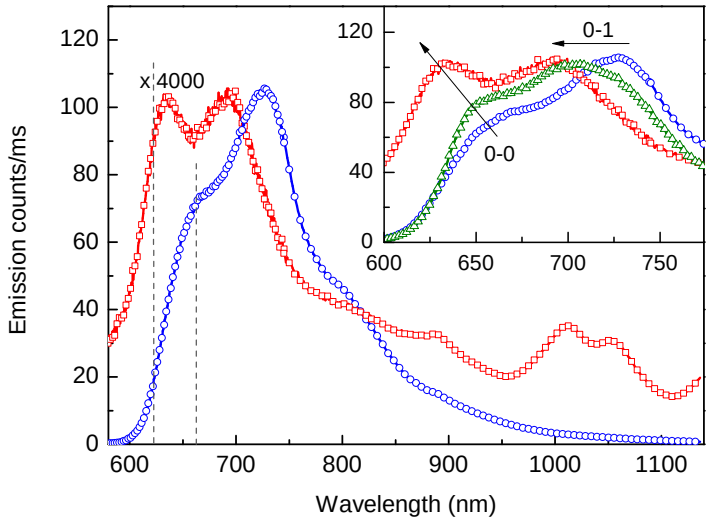

Figure 6.3: Steady-state photoluminescence spectra for P3HT (blue circles) and P3HT-NT (red squares, x4000) samples. Data were taken with an InGaAs detector above 745 nm and a Si CCD below and carefully scaled to match and allow comparison. The detection wavelength used for TCSPC and up-conversion samples is marked by a gray dashed line for each sample, namely the 0-0 P3HT transition wavelength in the bulk P3HT (660 nm) and P3HT-NT (620 nm) samples. The emission of the P3HT sample is red-shifted in comparison to the P3HT-NT sample due to the presence of aggregated P3HT, whose lamellar structure permits efficient electronic coupling between parallel chains leading to a lower energy gap. Inset: Wavelength region between 600 and 775 nm showing the P3HT emission from the samples including the P3HT emission from the P3HT-NT (1%) sample (green triangles, x40). The measurement was performed by Sam Stranks.

SWNTs is considered to be approximately 10%, as given by the manufacturer (SouthWest NanoTechnologies).

The steady-state photoluminescence (PL) measurements are shown in Fig. 6.3. Significant NT emission in the range from 950-1100 nm is only observed from the P3HT-NT sample. Comparing this PL emission to the empirical values deduced by Weisman *et al.*, a large red shift can be noticed [255]. This is caused by the type-II heterojunction alignment of the materials as predicted by Kanai and Grossman [252] and observed by Schuettfort *et al.* [25]. As the samples were excited at a wavelength of 400 nm, the majority of the light is absorbed by the P3HT. The emission of the carbon nanotubes is, thus, likely due to the transfer of excitations from the P3HT to the carbon nanotubes.

All three samples containing P3HT - P3HT-NT, P3HT-NT(1%) and pure P3HT - show

emission associated with P3HT in the wavelength range from 600 to 900 nm. The intensities and spectral shapes of the emission varies, however. The pure P3HT control sample shows a PL spectrum typical for aggregated P3HT, whose lamellar structure permits efficient electronic coupling between parallel chains leading to a red-shift in the emission [256, 257] and the suppression of the lowest (0-0) peak in the Franck-Condon series associated with the C-C stretch vibration [258–261]. Such suppression has been shown to result fundamentally from the high symmetry of the ensemble state comprising a number of identical chains over which the excitation becomes delocalized [260]. For the P3HT-NT sample, on the other hand, a clear 0-0 emission peak is visible in the P3HT emission. Additionally, the emission is blue-shifted in comparison to the bulk P3HT emission. The results suggest that the emission in the P3HT-NT samples is caused by the P3HT sheath. P3HT nanocrystalline aggregates, as shown in the AFM image in Fig. 6.1 do not seem to contribute to the emission. This might be caused by the low PL quantum efficiency of aggregates in comparison to the one of P3HT sheath [262–264]. The proximity to the carbon nanotube will probably also cause some PL quenching. The P3HT-NT(1%) emission has the shape of a superposition of the P3HT and the P3HT-NT emission with a greater contribution of the former. This suggests that aggregated network P3HT has a dominant contribution.

Comparing the intensity differences of the PL emission, it can be seen that the spectrum from pure P3HT is on the order of 4000 times more intense than from P3HT-NT and 40 times more intense than from P3HT-NT(1%). These differences suggest that the intimate contact between sheath P3HT and the nanotubes leads to highly efficient quenching of the excitations placed on the P3HT.

The quenching was further investigated using photoluminescence upconversion (PLUC) and time-correlated single-photon counting (TCSPC). With these two methods, the dynamics of photoexcitation quenching on P3HT was determined. Fig. 6.4 shows the PLUC measurements of the pure P3HT and P3HT-NT samples. The P3HT-NT(1%) sampled exhibited a very similar decay curve to the pure P3HT and is therefore not shown. Measurements were taken at the peaks corresponding to the steady-state P3HT 0-0 transition in each sample,

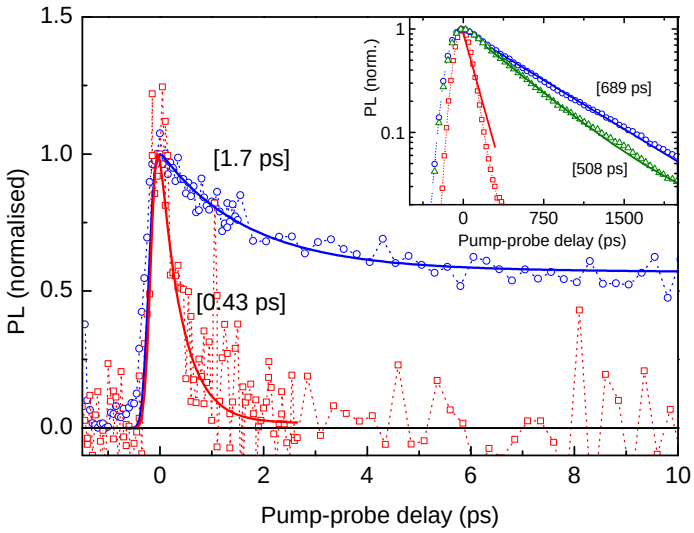

Figure 6.4: Normalized photoluminescence upconversion (PLUC) dynamics for the P3HT (blue circles) and the P3HT-NT sample (red squares) using 400 nm as the excitation wavelength with a fluence of 0.15 μJ/cm^2. The emission wavelength was 660 nm for the P3HT sample and 620 nm for the P3HT-NT sample corresponding to the P3HT 0-0 transition respectively. Similar dynamics were observed for the bulk sample when excited at 620 nm. The curves are fitted with time constants of 0.43 and 1.7 ps for P3HT-NT and P3HT samples, respectively, including a slow component for the P3HT sample only. Inset: TCSPC decay curves at the same probe wavelengths used for PLUC measurements following excitation at a wavelength of 400 nm and a fluence of 9 nJ/cm^2. Additionally, the P3HT-NT(1%) (green triangles) sample was detected at 660 nm. The measurement was performed by Sam Stranks.

i.e. 620 nm for the P3HT-NT sample and 660 nm for the pure P3HT and P3HT-NT(1%) samples. The inset shows the PL data with a time resolution of approximately 120 ps using TCSPC. Pure P3HT and P3HT-NT(1%) show a monoexponential decay of 689 and 508 ps, respectively. The decay of the P3HT-NT is the same as the system response and can therefore not be resolved with TCSPC. Using PLUC, the ultrafast decay components can be extracted. The pure P3HT sample can be fitted with the sum of two exponentials convoluted with a Gaussian system response of width 220 fs. One of the two time-constants is set to that of the extracted long-term decay (689 ps). For the other component a value of 1.7 ps is extracted which is likely to be caused by initial excitation relaxation processes mediated e.g. by vibrational or torsional cooling and migration through a density of states associated with energetic disorder [261, 265–267]. The response from P3HT-NT can be fitted using a monoexponential function with a time-constant of 0.43 ps, again convoluted with a Gaussian system response of width 220 fs. This fast decay is consistent with the previously observed factor 4000 quenching of its time-integrated emission relative to that of the pure P3HT.

These observations can be compared to previous studies where the PL dynamics of P3HT and poly(9,9-dioctylfluorenyl-2,7-diyl) (PFO) wrapped SWNTs were measured using TCSPC to conclude that energy transfer occurred on a timescale of order 400–500 ps [268, 269]. However, these studies were based on films that had a large amount of excess free polymer dominating the emission. The TCSPC data for the film containing excess P3HT, P3HT-NT(1%), shows a decay of the residual P3HT emission of 508 ps that is only slightly faster than the bulk P3HT (689 ps), probably due to regions of excess polymer far from an interface with a NT, in agreement with these previous studies. The fast quenching in the presence of the NTs, however, is masked by the low time resolution of TCSPC, as demonstrated by the PLUC measurements.

In order to determine whether the P3HT emission quenching in the blend samples is caused by charge separation at the interface, ultrafast transient absorption measurements were undertaken on the samples. Samples were excited at 400 nm, the same wavelength the samples were excited at for the PL measurements, and a fluence of 50 μJ/cm^2 at the focus

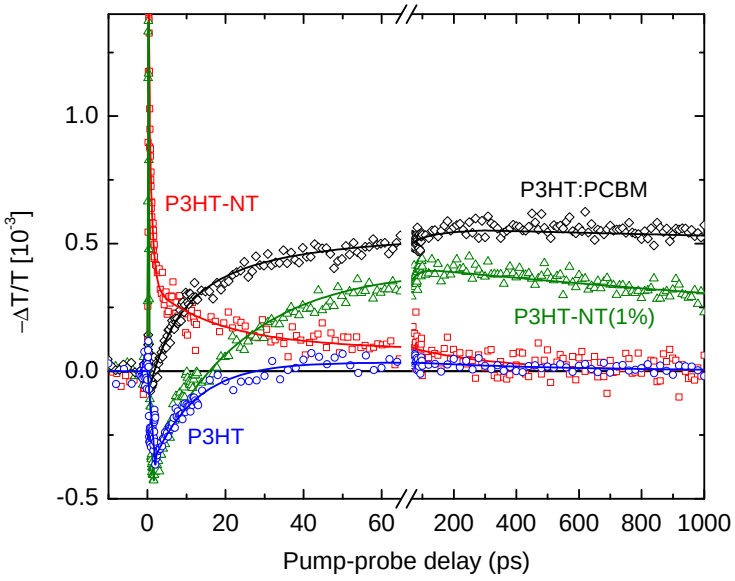

Figure 6.5: Change in relative transmission for varying pump-probe delays for the P3HT-PCBM (black diamonds), P3HT-NT (red squares), and P3HT-NT(1%) (green triangles) samples probed at 730 nm after excitation at 400 nm with a fluence of 50 uJ/cm^2. Solid lines are a guide to the eye.

representing the lowest value for the setup to achieve a high enough signal-to-noise ratio. The resulting charge densities of the samples is estimated to be on the order of 10^{19} cm^{-3} in comparison to values of $10^{16} - 10^{17}$ cm^{-3} for P3HT:PCBM devices when illuminated by the sun [270]. Due to the high fluence absorption measurements are influenced by exciton-exciton annihilations [271]. The change in absorption was probed at a wavelength of 730 nm, the peak of the absorption for the delocalized polaron [272], to monitor the presence and lifetime of free charges.

Fig. 6.5 shows the relative change in transmission for the four P3HT-containing samples. P3HT-PCBM, which is know for their significant photon-to-charge conversion ratios [273], displays the expected well-known trend for long-lived absorption arising from charge separated polaron pairs [274, 275]. The transient response from the P3HT bulk sample is also consistent with previously reported observations showing an initial decreased absorption that has been attributed to stimulated emission from excitons originating from some regions of regio-random P3HT [262, 274, 275]. Exciton-exciton annihilation processes, which are sig-

nificant with the fluences used here [271], cause a fast decay of the absorption signal, which may also contain a very small transient component arising from charge absorption originating from internal hot exciton dissociation intrinsic to the polymer [276–278]. As expected, no long-term charge-separated state exists for the bulk P3HT sample.

The P3HT-NT signal, in contrast, shows no negative stimulated emission signal. Instead, an increased absorption is visible that decays relatively quickly. As the PLUC measurements revealed a quenching of the sheath P3HT excitons on a timescale of 400 fs, the absence of stimulated emission is expected. Additionally, the P3HT nanocrystals attached to some of the SWNTs (Fig. 6.1) are highly regio-regular with no regio-random domains, and thus very low stimulated emission rates should be expected [262, 274, 275]. The absorption signal has an ultrafast rise of approximately 350 fs and a decay occurring on several time scales. These data suggest that fast quenching of the P3HT emission in P3HT-NT films is accompanied by a rise in the presence of free charges on the P3HT. However, these free charges are clearly not long-lived, with the majority of the charge absorption disappearing within 10 ps after excitation and most of the rest decaying within another ∼100 ps. The free holes must therefore be rapidly transferred to states with low quantum efficiency, to account for the strong (4000×) PL quenching. These could either be the nanotube excitons, which are known to have strong Auger recombination at high excitation intensities [279–282] occurring on a timescale of 1-5 ps or bound charge-transfer complexes formed across the interface, similar to exciplexes, which are known to have low radiative efficiencies [246, 247, 250]. Fig. 6.2 shows that although weak in absolute terms, the nanotube PL becomes relatively more significant due to its shorter exciton lifetimes of approximately 100 ps [279, 280, 283], whereas no exciplex emission, which should occur in a similar wavelength region, is obviously visible. The NT emission is expected to dominate since exciplex lifetimes are known to be of order nanoseconds and above [246, 247, 250]. Nevertheless, such exciplex-like states have been shown to play a significant role in a variety of polymer-containing blends with type-II heterointerfaces [246–250] and are thus likely to be also of importance here.

However, the P3HT-NT(1%) sample containing excess P3HT shows significantly different

behavior. During the first 10 ps the data reveal enhanced transmission arising from stimulated emission caused by the majority of carriers which are excited in the network P3HT (including some regio-random) regions. The subsequent dynamics are similar to those for the P3HT:PCBM sample: a rapid growth in the free polaron absorption indicates an effective charge separation process with a rise time of 20–30 ps reflecting the migration time of excitons to the heterointerface. The peak value of the charge absorption signal is also similar to that observed for the P3HT:PCBM sample. Accounting for differences in sample absorption at the excitation wavelength, the peak charge generation efficiency in the P3HT-NT(1%) sample is estimated to be 40% of that found for the standard P3HT:PCBM blend with an optimized mass ratio [274]. The fact that the quenched PL data show a dominant contribution from aggregated network P3HT indicates there are occasional large regions of purely bulk P3HT in the P3HT-NT(1%) sample. The small fraction of P3HT excitons formed in these domains are unable to reach a P3HT:NT interface before recombining and hence do not contribute to free charge generation. Therefore, further optimization of both the film morphology and the P3HT:NT blend ratio may result in an even higher charge-generation being obtained. Removal of any remaining metallic nanotubes ($< 10\%$), which are liable to lead to energy transfer, would also improve the charge generation. The free-charge absorption for the P3HT-NT(1%) sample also shows a slight decline over the time window (1 ns) investigated. However, an accurate determination of the charge lifetime in these systems will require measurements over microsecond timescales, e.g. as those described in Ref. 249.

6.3 Discussion

The interpretation of these results is depicted in the scheme shown in Fig. 6.6. In the case of sheath P3HT, an exciton is generated in the P3HT and charge transfer results in an electron localized on the carbon nanotube with the hole remaining in the P3HT. However, the energy offset between P3HT and SWNT is small. As a result, although the hole is most likely to reside on the polymer side of the interface, it probably also has a significant probability for activated transfer to the SWNT. For the sheath morphology, the hole located on the polymer

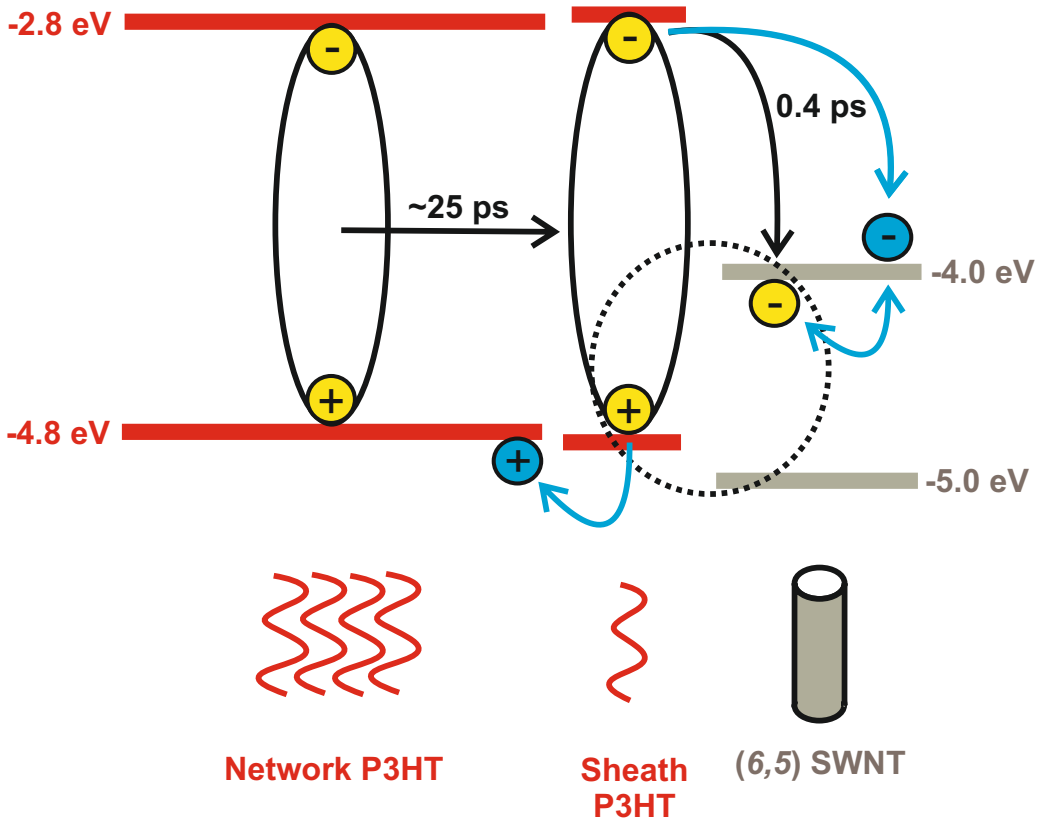

Figure 6.6: Scheme of the interface between a (6,5) carbon nanotube and a single layer of P3HT as well as a network of P3HT to illustrate the observed charge injection dynamics. Photoexcitation creates a bound exciton (yellow) on the P3HT network which subsequently migrates to the sheath P3HT within approximately 25 ps. At the interface the exciton dissociates and transfers an electron onto the carbon nanotube while the electron hole remains on the P3HT. The so created free hole (blue) forms a weakly bound exciplex across the interface or recombines nonradiatively as excitons whithin the nanotubes. In the presence of the P3HT network, the hole can migrate away from the interface and long-lived charge separation is achieved.

is geometrically constrained to be in close proximity to the nanotube. The formation of a bound state charge-transfer compelex, or 'exciplex', is therefore a likely scenario. However, such a charge-transfer state at the interface will differ from those typically observed for polymer-polymer heterojunctions, where it exists across two strands with similar dimensions in which fairly localized particles have similar effective masses. For the SWNT-polymer interface, in contrast, the electron on the nanotube is delocalized around the tube and has a mass for motion along the tube of only one-tenth of the free electron mass [284]. There is therefore a large mismatch in both wavefunction spread and particle masses for an exciplex composed of a charge pair across a nanotube-polymer interface. Estimating conservatively, this will reduce the binding energy of any exciplex by a factor of order 4 [285] compared to polymer-polymer heterojunction analogues [246] where binding energies are typically 100-200 meV. In summary, examination of the band structures leads to the conclusion that at the SWNT-polymer interface, the generated charge pairs will experience weak Coulomb interactions and comprise an electron wavefunction that is delocalized along the NT and a hole wavefunction that is mainly located on the polymer but may cross over into the NT. The charge pairs may therefore decay either through recombination of the charges across the interface, or while they are both located on the NT.

The addition of network polymer, as in the P3HT-NT(1%) sample, will significantly alter this picture by allowing the hole to migrate away from the interface thus eluding such recombination processes. In addition, the expanded dielectric environment of the complex may subtly alter the energetic level alignment at the interface making stable charge separation more favourable and further decreasing the exciplex binding energy. As a result, efficient long-lived charge separation is expected once additional P3HT is added to the individually polymer-wrapped nanotubes.

In the P3HT-NT sample, the PLUC data reveal that the exciton which is created on the sheath P3HT is quenched on a timescale of 0.4 ps, and transient absorption traces indicate that free polarons are produced within this time. These then decay away on a time scale of order 10-100 ps. These observations are attributed to the ultrafast charge dissociation of

P3HT excitons at the heterointerface. However, because the nanotubes are wrapped by only a single layer of P3HT, the positive charge on the P3HT cannot escape from the interface. The generated charge pair will decay through recombination of the charges either across the interface, or while they are both located on the SWNT.

After addition of the excess P3HT network, the majority of excitons are generated initially in the network P3HT. Transient absorption data show that free charges form in P3HT on a time scale of 20–30 ps (signal rise time), as the excitons move to an interface between a sheath-P3HT layer and a NT. This value is consistent with the quenching of the time-integrated polymer PL intensity by a factor of 40 relative to the bulk P3HT sample. At the interface, rapid dissociation of the exciton into free polarons again occurs but the majority of free holes generated are now long-lived. This is consistent with the picture that holes on the P3HT are now able to migrate away from the P3HT-SWNT interface thereby eluding capture. Therefore, the excess P3HT network provides a medium allowing extraction of the free holes and effective charge separation, in accordance with the predictions by Schuettfort *et al.* [25].

For this interpretation to be correct, however, a type-II heterojunction is a prerequisite which is only found in well-dispersed small-diameter carbon nanotubes. If a type-I heterojunction is present, as it is the case for larger diameter tubes [253], energy transfer becomes the dominant process and charge separation is not achieved. OPVs, thus, need to employ small diameter SWNT-polymer nanohybrids embedded in a network of excess polymer. Reported OPV devices to date have so far used only larger diameter HiPCO, arc-discharge or chemical vapour deposition carbon nanotubes and might therefore have type-I instead of type-II heterojunctions which could explain the poor performance observed [21, 23, 24, 251].

6.4 Conclusion

In summary, the charge generation dynamics at the interface formed between a semiconducting single-walled carbon nanotube and a single molecular layer of P3HT were studied [253].

Using femtosecond transient absorption spectroscopy, it was shown that photoexcitation of the sheath P3HT wrapped around a single SWNT leads to an electron transfer on a timescale of approximately 400 fs due to the formation of a type-II heterojunction between the two materials [25, 252]. The spatial separation of the SWNT confines the hole to the molecular layer and leads to the formation of either a charge-transfer complex across the interface or non-radiative recombination. Thus, no free charge carriers are generated. However, the introduction of an excess P3HT network allows the hole to migrate away from the interface and become a long-lived free charge carrier. Additionally, it was shown that a ratio of 1% P3HT wrapped around a SWNT to excess P3HT is sufficient to generate charges with a similar efficiency than optimized 60:40 P3HT:fullerene blends for which the fullerene electron acceptor does not absorb light.

These results suggest that despite the poor performance of nanotube-polymer organic photovoltaics to date, SWNT-polymer blends where the materials form a type-II heterojunction and which are embedded in a network of excess polymer might present a viable route for the development of efficient organic photovoltaic devices given the the high mobilities and large aspect ratios of carbon nanotubes [65, 286].

Chapter 7

Conclusions

7.1 Summary of Key Results

In this thesis, charge-transfer dynamics of organic semiconductors were investigated. Femto- and microsecond transient absorption spectroscopy, along with other spectroscopic techniques were used to understand the requirements for efficient charge transfer in dye-sensitized and nanotube-thiophene based solar cells.

The dependence of dye regeneration and charge collection on the PFF was studied using microsecond transient absorption and picosecond photoluminescence upconversion spectroscopy. It was found that the hole-transfer yield rises rapidly with higher PFFs. Beyond ∼30%, however, further increases of the PFF did change the hole-transfer yield. By applying simple statistical models it was shown that some cations undergo lateral hole-hopping before charge transfer from dye to spiro-OMeTAD occurs. The results suggest that only a small PFF is required to achieve efficient hole transfer in dye-sensitized solar cells. Increases of the device efficiency beyond a PFF of 30% were assigned to an improved charge-collection efficiency which is shown to occur in steps due to the infiltration process. Furthermore, percolation theory was used to predict that no significant improvements of the device efficiency beyond a ∼82% PFF are expected when using standard mesoporous TiO_2 with 20 nm pore sizes.

In a second study, femto- and microsecond transient absorption spectroscopy was employed to study the highest occupied molecular orbital (HOMO) level alignment between dye and three novel triarylamine type hole-transporting materials (HTMs) in dye-sensitized solar cells (DSSCs) in order to explore the possibility of reducing the over-potential and improve the power-conversion efficiency. The hole-transfer yield of the commonly used HTM spiro-OMeTAD was estimated to be approximately 75% and further reductions in the energy offset would lead to a smaller hole-transfer yield and thus device efficiency. Furthermore, it was demonstrated that the design of the HTM has an additional impact on the electronic density of states present at the TiO_2 electrode surface, and hence influences not only hole- but also electron-transfer from the sensitizer.

Finally, nanohybrids consisting of single-walled carbon nanotubes (SWNTs) wrapped with a single layer of Poly(3-hexylthiophene-2,5-diyl) (P3HT) were probed to understand the current poor performance of organic photovoltaic devices currently employing these materials. Using femtosecond transient absorption spectroscopy, it was shown that photoexcitation of the sheath P3HT wrapped around a single SWNT leads to an electron transfer on a timescale of approximately 400 fs due to the formation of a type-II heterojunction between the two materials [25, 252]. The spatial separation of the SWNT confines the hole to the molecular layer and leads to the formation of either a charge-transfer complex across the interface or non-radiative recombination. Thus, no free charge carriers are generated. However, the introduction of an excess P3HT network allows the hole to migrate away from the interface and become a long-lived free charge carrier. Additionally, it was shown that a ratio of 1% P3HT wrapped around a SWNT to excess P3HT is sufficient to generate charges with a similar efficiency than optimized 60:40 P3HT:fullerene blends for which the fullerene electron acceptor does not absorb light.

7.2 Outlook and Future Work

The presented studies in this work have given a new level of understanding of the mechanisms and limitations of dye-sensitized and nanotube-thiophene based solar cells. The insights into solid-state DSSCs, together with further research addressing other issues such as optimizing the ionic additives, will provide a route for improvement of the device efficiency helping to close the gap to the liquid-electrolyte counterpart. Limitations of the power-conversion efficiency due to the small optimal device thickness in solid-state DSSCs might also be overcome by alternative light absorbers with stronger absorption coefficients. Recently, Lee *et al.* used a highly crystalline perovskite with strong light absorbtion in combination with the hole-transporting material spiro-OMeTAD and achieved power-conversion efficiencies of 10.9% [287].

For organic photovoltaic devices, the presented study of charge separation at a polymer-single-walled carbon nanotube heterojunction provides scope for promising future work. Implementation of small-diameter carbon nanotubes-P3HT hybrids in devices and optimization of the ratio of excess P3HT network to the P3HT-NT nanohybrid should provide significant improvements of the power-conversion efficiency in comparison to current devices. Based on these results, OPV devices with P3HT-NT nanohybrids embedded in an excess P3HT network have been recently studied [288]. Using a carbon nanotube weight fraction of 3%, power-conversion efficiencies of approximately 0.7% were achieved. As carbon nanotubes with intermediate diameters were used, further improvements might be still possible by shifting to smaller diameters.

Appendix A

Appendix

A.1 Derivation of Equation 4.5

Lateral "hole-hopping" is modeled by starting with placement of a hole on a random dye molecule. For the subsequent hole motion, it is then assumed that if no spiro-OMeTAD molecule is attached to the dye monolayer at this starting position, the hole transfers to a random adjacent dye molecule. If a spiro-OMeTAD molecule is attached to this dye molecule, hole transfer to that spiro-OMeTAD molecule occurs. If no spiro-OMeTAD molecule is present, the hole transfers to another random adjacent dye molecule. This process is continued until transfer to spiro-OMeTAD or recombination with an electron has occured. If the probability of a spiro-OMeTAD molecule being attached to the specific dye molecule after i steps is defined as p_i and no recombination has occurred within a time interval t, the hole-transfer yield is given by

$$\eta_{\mathrm{ht}}(t) = p_0 + \sum_{i=1}^{n(t)} \left[p_i \prod_{k=0}^{i-1} (1 - p_k) \right]. \tag{A.1}$$

The probability p_i can be calculated by dividing the number s of spiro-OMeTAD molecules in the surface layer by the number $T - i$ of total positions in the surface layer the hole has not transferred to, *i.e.*

$$p_i = \frac{s}{T-i}. \tag{A.2}$$

As $p_0 = p(\mathrm{PFF})$, it follows that

$$p_i = \frac{T}{T-i} p(\mathrm{PFF}). \tag{A.3}$$

The hole-transfer yield is then given by

$$\eta_{\mathrm{ht}}(t) = p(\mathrm{PFF}) \left[1 + \sum_{\mathrm{i}=1}^{\mathrm{n(t)}} \frac{\mathrm{T}}{\mathrm{T-i}} \prod_{\mathrm{k}=0}^{\mathrm{i}-1} \left(1 - \frac{\mathrm{T}}{\mathrm{T-k}} \mathrm{p(PFF)} \right) \right]. \tag{A.4}$$

If the number $n(t)$ of dye molecules the hole transfers to within time interval t is much smaller than the number T of possible spiro-OMeTAD molecules in the surface layer, *i.e.* $n(t) \ll T$, then $p_i \approx p(\mathrm{PFF})$ and

$$\begin{aligned}
\eta_{\mathrm{ht}}(t) &\approx p(\mathrm{PFF}) + \sum_{\mathrm{i}=1}^{\mathrm{n(t)}} \left[\mathrm{p(PFF)} \prod_{\mathrm{k}=0}^{\mathrm{i}-1} (1 - \mathrm{p(PFF)}) \right] && \text{(A.5)} \\
&= p(\mathrm{PFF}) \sum_{\mathrm{i}=0}^{\mathrm{n(t)}} [1 - \mathrm{p(PFF)}]^{\mathrm{i}} && \text{(A.6)} \\
&= 1 - [1 - p(\mathrm{PFF})]^{\mathrm{n(t)}+1} && \text{(A.7)}
\end{aligned}$$

where the geometric series was applied in the last step.

Bibliography

[1] Secretary-General, United Nations, United Nations Conference on Sustainable Development (2011).

[2] International Energy Agency (IEA), World energy outlook 2011 (2011).

[3] International Energy Agency (IEA), Clean energy progress report (2011).

[4] B. Parida, S. Iniyan, & R. Goic, *Renew. Sust. Energ. Rev.*, 15 1625 (2011).

[5] E. Kymakis, I. Alexandrou, & G. A. J. Amaratunga, *J. Appl. Phys.*, 93 1764 (2003).

[6] B. E. Hardin, H. J. Snaith, & M. D. McGehee, *Nat. Photonics*, 6 162 (2012).

[7] National Renewable Energy Laboratory (NREL), Best-research cell efficiencies (2012).

[8] G. Chamberlain, *Solar Cells*, 8 (1) 47 (1983).

[9] B. O'Regan & M. Grätzel, *Nature*, 353 737 (1991).

[10] M. Gr"atzel, *Nature*, 414 338 (2001).

[11] A. Hagfeldt & M. Grätzel, *Accounts Chem. Res.*, 33 269 (2000).

[12] C.-C. Chen, L. Dou, R. Zhu, C.-H. Chung, T.-B. Song *et al.*, *ACS Nano*, 6 (8) 7185 (2012).

[13] W. Shockley & H. J. Queisser, *J. Appl. Phys.*, 32 510 (1961).

[14] H. J. Snaith, *Adv. Funct. Mater.*, 20 13 (2010).

[15] J. E. Kroeze, N. Hirata, L. Schmidt-Mende, C. Orizu, S. D. Ogier *et al.*, *Adv. Funct. Mater.*, 16 1832 (2006).

[16] U. Bach, D. Lupo, P. Comte, J.-E. Moser, F. Weissörtel *et al.*, *Nature*, 395 583 (1998).

[17] J. Burschka, A. Dualeh, F. Kessler, E. Baranoff, Cevey-Ha *et al.*, *J. Am. Chem. Soc.*, 133 18042 (2011).

[18] S. A. Haque, T. Park, A. B. Holmes, & J. R. Durrant, *ChemPhysChem*, 4 89 (2003).

[19] A. Nish, J. Y. Hwang, J. Doig, & R. J. Nicholas, *Nat. Nanotechnol.*, 2 640 (2007).

[20] J. Y. Hwang, A. Nish, J. Doig, S. Douven, C.-W. Chen *et al.*, *J. Am. Chem. Soc.*, 130 3543 (2008).

[21] J. X. Geng & T. Y. Zeng, *J. Am. Chem. Soc.*, 128 16827 (2006).

[22] A. T. Mallajosyula, S. S. K. Iyer, & B. Mazhari, *J. Appl. Phys.*, 108 094902 (2010).

[23] E. Kymakis, P. Servati, P. Tzanetakis, E. Koudoumas, N. Kornilios *et al.*, *Nanotechnology*, 18 435702 (2007).

[24] J. Arranz-andres & W. J. Blau, *Carbon*, 46 2067 (2008).

[25] T. Schuettfort, A. Nish, & R. J. Nicholas, *Nano Lett.*, 9 3871 (2009).

[26] C. K. Chiang, C. R. Fincher, Y. W. Park, A. J. Heeger, H. Shirakawa *et al.*, *Phys. Rev. Lett.*, 39 1098 (1977).

[27] F. C. Grozema & L. D. A. Siebbeles, *Int. Rev. Phys. Chem.*, 27 87 (2008).

[28] C. W. Tang & S. A. V. Slyke, *Appl. Phys. Lett.*, 51 913 (1987).

[29] J. H. Burroughes, D. D. C. Bradley, A. R. Brown, R. N. Marks, K. Mackay *et al.*, *Nature*, 347 539 (1990).

[30] J. R. Sheats, H. Antoniadis, M. Hueschen, W. Leonard, J. Miller *et al.*, *Science*, 273 884 (1996).

[31] R. H. Friend, R. W. Gymer, A. B. Holmes, J. H. Burroughes, R. N. Marks *et al.*, *Nature*, 397 121 (1999).

[32] M. Gr"atzel, *Nature*, 421 586 (2003).

[33] A. Tsumura, H. Koezuka, & T. Ando, *Appl. Phys. Lett.*, 49 1210 (1986).

[34] H. Koezuka, A. Tsumura, & T. Ando, *Synth. Met.*, 18 699 (1987).

[35] G. Horowitz, X. Z. Peng, D. Fichou, & F. GARNIER, *J. Appl. Phys.*, 67 528 (1990).

[36] F. Garnier, *Pure Appl. Chem.*, 68 1455 (1996).

[37] J. K. W. Marye Anne Fox, *Organic Chemistry, 3rd ed.*, Jones & Bartlett Publishers (2004).

[38] T. U. Kampen, *Low Molecular Weight Organic Semiconductors*, John Wiley & Sons (2011).

[39] J. Zyss & J. L. Oudar, *Phys. Rev. A*, 26 2028 (1982).

[40] C. E. Pope, M.; Swenberg, *Electronic Processes in Organic Crystals*, Clarendon Press (1982).

[41] J.-L. Brdas, D. Beljonne, V. Coropceanu, & J. Cornil, *Chemical Reviews*, 104 (11) 4971 (2004), pMID: 15535639.

[42] A. Ruini, M. J. Caldas, G. Bussi, & E. Molinari, *Phys. Rev. Lett.*, 88 206403 (2002).

[43] H. C. W. M. Schwoerer, *Organic Molecular Solids*, Wiley-VCH (2007).

[44] M. P. Charles Swenberg, *Electronic Processes in Organic Crystals and Polymers.*, Oxford Science Publications (1999).

[45] R. A. Marcus, *Rev. Mod. Phys.*, 65 (3) 599 (1993).

[46] R. A. Marcus, *The Journal of Chemical Physics*, 24 (5) 966 (1956).

[47] P. F. Barbara, T. J. Meyer, & M. A. Ratner, *J. Phys. Chem.*, 100 (31) 13148 (1996).

[48] D. DeVault, *Quantum Mechanical Tunneling in Biological Systems*, Cambridge University Press (1984).

[49] J. Jortner, *The Journal of Chemical Physics*, 64 (12) 4860 (1976).

[50] V. Coropceanu, J. Cornil, D. A. da Silva Filho, Y. Olivier, R. Silbey *et al.*, *Chem. Rev.*, 107 (4) 926 (2007).

[51] N. Karl, in *Crystals*, vol. 4, pp. 1–100–, Springer Berlin Heidelberg (1980).

[52] W. Shockley, *Electrons and Holes in Semiconductors*, van Nostrand Reinhold, Princeton, NJ (1950).

[53] E. M. Conwell, *Phys. Rev.*, 103 51 (1956).

[54] A. Miller & E. Abrahams, *Phys. Rev.*, 120 745 (1960).

[55] H. B"assler, *Phys. Status Solidi B-Basic Res.*, 175 15 (1993).

[56] H. Scher & E. W. Montroll, *Phys. Rev. B*, 12 2455 (1975).

[57] O. H. Leblanc, *J. Chem. Phys.*, 30 1443 (1959).

[58] W. Warta & N. Karl, *Phys. Rev. B*, 32 1172 (1985).

[59] S. Iijima, *Nature*, 354 56 (1991).

[60] S. Berber, Y.-K. Kwon, & D. Tománek, *Phys. Rev. Lett.*, 84 4613 (2000).

[61] E. Pop, D. Mann, Q. Wang, K. Goodson, & H. Dai, *Nano Letters*, 6 (1) 96 (2006).

[62] E. T. Thostenson, Z. Ren, & T.-W. Chou, *Composites Science and Technology*, 61 (13) 1899 (2001).

[63] H. W. C. Postma, T. Teepen, Z. Yao, M. Grifoni, & C. Dekker, *Science*, 293 (5527) 76 (2001).

[64] H. J. Dai, J. H. Hafner, A. G. Rinzler, D. T. Colbert, & R. E. Smalley, *Nature*, 384 (6605) 147 (1996).

[65] J. M. S. Reich, C. Thomsen, *Carbon Nanotubes*, WILEY-VCH (2003).

[66] P. M. Ajayan, *Chem. Rev.*, 99 (7) 1787 (1999).

[67] R. Saito, G. Dresselhaus, & M. S. Dresselhaus, *Phys. Rev. B*, 61 2981 (2000).

[68] X. Lu & Z. Chen, *Chem. Rev.*, 105 (10) 3643 (2005).

[69] H. Kataura, Y. Kumazawa, Y. Maniwa, I. Umezu, S. Suzuki *et al.*, *Synthetic Metals*, 103 (13) 2555 (1999).

[70] V. N. Popov, *New Journal of Physics*, 6 (1) 17 (2004).

[71] S. M. Bachilo, M. S. Strano, C. Kittrell, R. H. Hauge, R. E. Smalley *et al.*, *Science*, 298 (5602) 2361 (2002).

[72] R. B. Weisman & S. M. Bachilo, *Nano Letters*, 3 (9) 1235 (2003).

[73] R. Krupke, F. Hennrich, H. v. Lhneysen, & M. M. Kappes, *Science*, 301 (5631) 344 (2003).

[74] C. Fritts, *American Journal of Science*, 26 465 (1883).

[75] M. A. Green, *Solar cells : operating principles, technology, and system applications*, Prentice Hall (1982).

[76] J. Nelson, *The Physics of Solar Cells*, Imperial College Press (2003).

[77] P. Frass, *Solar Cells and Their Applications*, WILEY (2010).

[78] American Society for Testing and Materials (ASTM), Terrestrial reference spectra for photovoltaic performance evaluation.

[79] W. Shockley & W. T. Read, *Phys. Rev.*, 87 835 (1952).

[80] R. N. Hall, *Phys. Rev.*, 87 387 (1952).

[81] R. A. Street & M. Schoendorf, *Phys. Rev. B*, 81 205307 (2010).

[82] T. Kirchartz, B. E. Pieters, J. Kirkpatrick, U. Rau, & J. Nelson, *Phys. Rev. B*, 83 115209 (2011).

[83] S. R. Cowan, W. L. Leong, N. Banerji, G. Dennler, & A. J. Heeger, *Adv. Funct. Mater.*, 21 3083 (2011).

[84] G. A. H. Wetzelaer, M. Kuik, M. Lenes, & P. W. M. Blom, *Appl. Phys. Lett.*, 99 153506 (2011).

[85] P. Würfel, *CHIMIA International Journal for Chemistry*, 61 (12) 770 (2007).

[86] G. D. Scholes & G. Rumbles, *Nat Mater*, 5 (9) 683 (2006).

[87] I. Hill, A. Kahn, Z. Soos, & R. Pascal, Jr, *Chemical Physics Letters*, 327 (34) 181 (2000).

[88] N. C. Giebink, G. P. Wiederrecht, M. R. Wasielewski, & S. R. Forrest, *Phys. Rev. B*, 83 195326 (2011).

[89] H. Kallmann & M. Pope, *The Journal of Chemical Physics*, 30 (2) 585 (1959).

[90] C. W. Tang, *Appl. Phys. Lett.*, 48 183 (1986).

[91] R. F. Service, *Science*, 332 (6027) 293 (2011).

[92] P. G. Nicholson & F. A. Castro, *Nanotechnology*, 21 (49) 492001 (2010).

[93] J. Hou, Z. Tan, Y. Yan, Y. He, C. Yang *et al.*, *J. Am. Chem. Soc.*, 128 (14) 4911 (2006).

[94] E. Bundgaard & F. C. Krebs, *Solar Energy Materials and Solar Cells*, 91 (11) 954 (2007), ¡ce:title¿Low Band Gap Polymer Materials for Organic Solar Cells¡/ce:title¿.

[95] R. Kroon, M. Lenes, J. C. Hummelen, P. W. M. Blom, & B. de Boer, *Polymer Reviews*, 48 (3) 531 (2008).

[96] B. Gregg & M. Hanna, *JOURNAL OF APPLIED PHYSICS*, 93 (6) 3605 (2003).

[97] I. H. Campbell, T. W. Hagler, D. L. Smith, & J. P. Ferraris, *Phys. Rev. Lett.*, 76 1900 (1996).

[98] Z. D. Popovic, A. mee Hor, & R. O. Loutfy, *Chemical Physics*, 127 (13) 451 (1988).

[99] B. A. Gregg, J. Sprague, & M. W. Peterson, *The Journal of Physical Chemistry B*, 101 (27) 5362 (1997).

[100] J. E. Kroeze, T. J. Savenije, & J. M. Warman, *Journal of Photochemistry and Photobiology A: Chemistry*, 148 (13) 49 (2002).

[101] H. Kerp, H. Donker, R. Koehorst, T. Schaafsma, & E. van Faassen, *Chemical Physics Letters*, 298 (46) 302 (1998).

[102] M. Hiramoto, H. Fujiwara, & M. Yokoyama, *Applied Physics Letters*, 58 (10) 1062 (1991).

[103] J. J. M. Halls, C. A. Walsh, N. Greenham, E. A. Marseglia, R. Friend *et al.*, *Nature*, 376 (6540) 498 (1995).

[104] G. Yu, J. Gao, J. C. Hummelen, F. Wudl, & A. J. Heeger, *Science*, 270 (5243) 1789 (1995).

[105] W. U. Huynh, J. J. Dittmer, & A. P. Alivisatos, *Science*, 295 (5564) 2425 (2002).

[106] K. Vandewal, S. Albrecht, E. T. Hoke, K. R. Graham, J. Widmer *et al.*, *Nat Mater*, 13 (1) 63 (2014).

[107] J.-L. Brdas, J. E. Norton, J. Cornil, & V. Coropceanu, *Accounts of Chemical Research*, 42 (11) 1691 (2009), pMID: 19653630.

[108] T. M. Clarke & J. R. Durrant, *Chem. Rev.*, 110 (11) 6736 (2010).

[109] I. A. Howard, R. Mauer, M. Meister, & F. Laquai, *Journal of the American Chemical Society*, 132 (42) 14866 (2010).

[110] P. Peumans & S. R. Forrest, *Chemical Physics Letters*, 398 (13) 27 (2004).

[111] S. De, T. Pascher, M. Maiti, K. G. Jespersen, T. Kesti *et al.*, *J. Am. Chem. Soc.*, 129 (27) 8466 (2007).

[112] S. Westenhoff, I. A. Howard, J. M. Hodgkiss, K. R. Kirov, H. A. Bronstein *et al.*, *Journal of the American Chemical Society*, 130 (41) 13653 (2008).

[113] C. G. Shuttle, B. O'Regan, A. M. Ballantyne, J. Nelson, D. D. C. Bradley *et al.*, *Phys. Rev. B*, 78 113201 (2008).

[114] T. M. Clarke, F. C. Jamieson, & J. R. Durrant, *J. Phys. Chem. C*, 113 (49) 20934 (2009).

[115] A. Yella, H. W. Lee, H. N. Tsao, C. Y. Yi, A. K. Chandiran *et al.*, *Science*, 334 629 (2011).

[116] H. J. Snaith & L. Schmidt-Mende, *Adv. Mater.*, 19 3187 (2007).

[117] L. Schmidt-Mende, W. M. Campbell, Q. Wang, K. W. Jolley, D. L. Officer *et al.*, *ChemPhysChem*, 6 1253 (2005).

[118] S. Ferrere, A. Zaban, & B. A. Gregg, *J. Phys. Chem. B*, 101 4490 (1997).

[119] A. Burke, L. Schmidt-Mende, S. Ito, & M. Grätzel, *Chem. Commun.*, 0 234 (2007).

[120] P. Wang, S. M. Zakeeruddin, J.-E. Moser, M. K. Nazeeruddin, T. Sekiguchi *et al.*, *Nat. Mater.*, 2 402 (2003).

[121] Y. M. Cao, Y. Bai, Q. J. Yu, Y. M. Cheng, S. Liu *et al.*, *J. Phys. Chem. C*, 113 6290 (2009).

[122] M. K. Nazeeruddin, A. Kay, I. Rodicio, R. Humphrybaker, E. Muller *et al.*, *J. Am. Chem. Soc.*, 115 6382 (1993).

[123] U.S. Geological Survey, 2010 minerals yearbook (2010).

[124] P. Y. Reddy, L. Giribabu, C. Lyness, H. J. Snaith, C. Vijaykumar *et al.*, *Angew. Chem.-Int. Edit.*, 46 373 (2007).

[125] J. J. He, G. Benko, F. Korodi, T. Polìvka, R. Lomoth *et al.*, *J. Am. Chem. Soc.*, 124 4922 (2002).

[126] A. delaEscosura, M. Martnez-Daz, T. Torres, R. Grubbs, D. Guldi *et al.*, *Chemistry An Asian Journal*, 1 (1-2) 148 (2006).

[127] R. Katoh, A. Furube, T. Yoshihara, K. Hara, G. Fujihashi *et al.*, *J. Phys. Chem. B*, 108 4818 (2004).

[128] J. B. Asbury, E. Hao, Y. Q. Wang, H. N. Ghosh, & T. Q. Lian, *J. Phys. Chem. B*, 105 4545 (2001).

[129] Y. Fukai, Y. Kondo, S. Mori, & E. Suzuki, *Electrochem. Commun.*, 9 1439 (2007).

[130] P. Tiwana, P. Docampo, M. B. Johnston, H. J. Snaith, & L. M. Herz, *ACS Nano*, 5 5158 (2011).

[131] R. W. Fessenden & P. V. Kamat, *J. Phys. Chem.*, 99 12902 (1995).

[132] A. Furube, R. Katoh, K. Hara, S. Murata, H. Arakawa *et al.*, *J. Phys. Chem. B*, 107 4162 (2003).

[133] P. Tiwana, P. Parkinson, M. B. Johnston, H. J. Snaith, & L. M. Herz, *J. Phys. Chem. C*, 114 1365 (2010).

[134] G. Benko, P. Myllyperkio, J. Pan, A. P. Yartsev, & V. Sundström, *J. Am. Chem. Soc.*, 125 1118 (2003).

[135] L. M. Peter, *Phys. Chem. Chem. Phys.*, 9 (21) 2630 (2007).

[136] D. Kuang, C. Klein, H. J. Snaith, J. E. Moser, R. Humphry-Baker *et al.*, *Nano Lett.*, 6 769 (2006).

[137] A. Hagfeldt & M. Grätzel, *Chem. Rev.*, 95 49 (1995).

[138] B. O'Regan, J. Moser, M. Anderson, & M. Grätzel, *J. Phys. Chem.*, 94 8720 (1990).

[139] S. A. Haque, Y. Tachibana, D. R. Klug, & J. R. Durrant, *J. Phys. Chem. B*, 102 1745 (1998).

[140] G. Boschloo & A. Hagfeldt, *Accounts Chem. Res.*, 42 1819 (2009).

[141] A. F. Nogueira & C. Longo, *Coord. Chem. Rev.*, 248 1455 (2004).

[142] K. Tennakone, G. R. R. A. Kumara, A. R. Kumarasinghe, K. G. U. Wijayantha, & P. M. Sirimanne, *Semicond. Sci. Technol.*, 10 1689 (1995).

[143] K. Murakoshi, R. Kogure, Y. Wada, & S. Yanagida, *Chem. Lett.*, 26 471 (1997).

[144] B. O'Regan & D. T. Schwartz, *Chem. Mat.*, 10 1501 (1998).

[145] A. Abrusci, I. K. Ding, M. Al-hashimi, T. Segal-peretz, M. D. McGehee *et al.*, *Energy Environ. Sci.*, 4 3051 (2011).

[146] U. Bach, Y. Tachibana, J.-E. Moser, S. A. Haque, J. R. Durrant *et al.*, *J. Am. Chem. Soc.*, 121 7445 (1999).

[147] L. Schmidt-Mende, S. M. Zakeeruddin, & M. Grätzel, *Appl. Phys. Lett.*, 86 013504 (2005).

[148] L. Schmidt-Mende & M. Grätzel, *Thin Solid Films*, 500 296 (2006).

[149] D. Poplavskyy & J. Nelson, *J. Appl. Phys.*, 93 341 (2003).

[150] C. Jager, R. Bilke, M. Heim, D. Haarer, H. Karickal *et al.*, *Synth. Met.*, 121 1543 (2001).

[151] W. M. Campbell, K. W. Jolley, P. Wagner, K. Wagner, P. J. Walsh *et al.*, *J. Phys. Chem. C*, 111 11760 (2007).

[152] B. O'Regan, F. Lenzmann, R. Muis, & J. Wienke, *Chem. Mat.*, 14 5023 (2002).

[153] W. Feng, T. Umeda, A. Fujii, X. G. Wang, & K. Yoshino, *Jpn. J. Appl. Phys. Part 1 - Regul. Pap. Short Notes Rev. Pap.*, 43 3473 (2004).

[154] H. J. Snaith, R. Humphry-Baker, P. Chen, I. Cesar, S. M. Zakeeruddin *et al.*, *Nanotechnology*, 19 424003 (2008).

[155] P. Docampo, A. Hey, S. Guldin, R. Gunning, U. Steiner *et al.*, *Advanced Functional Materials*, pp. n/a–n/a (2012).

[156] U. B. Cappel, E. A. Gibson, A. Hagfeldt, & G. Boschloo, *J. Phys. Chem. C*, 113 6275 (2009).

[157] J. Melas-Kyriazi, I. K. Ding, A. Marchioro, A. Punzi, B. E. Hardin *et al.*, *Adv. Energy Mater.*, 1 407 (2011).

[158] D. Gebeyehu, C. J. Brabec, & N. S. Sariciftci, *Thin Solid Films*, 403 271 (2002).

[159] S. X. Tan, J. Zhai, B. F. Xue, M. X. Wan, Q. B. Meng *et al.*, *Langmuir*, 20 2934 (2004).

[160] S. X. Tan, J. Zhai, M. X. Wan, Q. B. Meng, Y. L. Li *et al.*, *J. Phys. Chem. B*, 108 18693 (2004).

[161] Y. P. Wang, K. Yang, S. C. Kim, R. Nagarajan, L. A. Samuelson *et al.*, *Chem. Mat.*, 18 4215 (2006).

[162] G. Bartholomew & A. Heeger, *Advanced Functional Materials*, 15 (4) 677 (2005).

[163] K. Coakley, B. Srinivasan, J. Ziebarth, C. Goh, Y. Liu *et al.*, *Advanced Functional Materials*, 15 (12) 1927 (2005).

[164] J. B. Xia, N. Masaki, M. Lira-cantu, Y. Kim, K. J. Jiang *et al.*, *J. Am. Chem. Soc.*, 130 1258 (2008).

[165] G. Redmond, D. Fitzmaurice, & M. Grätzel, *J. Phys. Chem.*, 97 6951 (1993).

[166] J. Krüger, R. Plass, L. Cevey, M. Piccirelli, M. Grätzel *et al.*, *Appl. Phys. Lett.*, 79 2085 (2001).

[167] Y. Liu, A. Hagfeldt, X. R. Xiao, & S. E. Lindquist, *Sol. Energy Mater. Sol. Cells*, 55 267 (1998).

[168] B. Enright & D. Fitzmaurice, *J. Phys. Chem.*, 100 1027 (1996).

[169] H. J. Snaith & M. Grätzel, *Appl. Phys. Lett.*, 89 262114 (2006).

[170] C. A. Kelly, F. Farzad, D. W. Thompson, J. M. Stipkala, & G. J. Meyer, *Langmuir*, 15 7047 (1999).

[171] V. I. Arkhipov, P. Heremans, E. V. Emelianova, & H. Bässler, *Phys. Rev. B*, 71 045214 (2005).

[172] B. A. Gregg, S. G. Chen, & R. A. Cormier, *Chem. Mat.*, 16 4586 (2004).

[173] A. Abate, T. Leijtens, S. Pathak, J. Teuscher, R. Avolio *et al.*, *Phys. Chem. Chem. Phys.*, 15 (7) 2572 (2013).

[174] M. Fox, *Optical Properties of Solids*, Oxford University Press, first edn (2001).

[175] J. R. M. Evgenij Barsoukov, *Impedance Spectroscopy: Theory, Experiment, and Applications*, Wiley-IEEE (2005).

[176] C. Rulliere, *Femtosecond Laser Pulses: Principles and Experiments*, Springer-Verlag, Berlin, 2nd Ed. (2004).

[177] G. H. C. New, *Reports on Progress in Physics*, 46 (8) 877 (1983).

[178] P. Horowitz & W. Hill, *The Art of Electronics*, Cambridge University Press (1980).

[179] G. New, *Introduction to Nonlinear Optics*, Cambridge University Press (2011).

[180] T. H. Maiman, *Nature*, 187 493 (1960).

[181] P. A. Franken, G. Weinreich, C. W. Peters, & A. E. Hill, *Phys. Rev. Lett.*, 7 118 (1961).

[182] P. Mandel, *Nonlinear Optics*, Wiley-VC (2010).

[183] Demtroeder, *Laser Spectrosocopy*, Springer-Verlag, Berlin (2003).

[184] R. L. Fork, C. V. Shank, C. Hirlimann, R. Yen, & W. J. Tomlinson, *Opt. Lett.*, 8 (1) 1 (1983).

[185] R. R. Alfano & S. L. Shapiro, *Phys. Rev. Lett.*, 24 584 (1970).

[186] G. Yang & Y. R. Shen, *Opt. Lett.*, 9 (11) 510 (1984).

[187] M. Nakazawa & M. Tokuda, *Japanese Journal of Applied Physics*, 22 (Part 2, No. 4) L239 (1983).

[188] K. Midorikawa, H. Kawano, A. Suda, C. Nagura, & M. Obara, *Applied Physics Letters*, 80 (6) 923 (2002).

[189] A. L. Gaeta, *Phys. Rev. Lett.*, 84 3582 (2000).

[190] L. D. Boni, C. Toro, & F. E. Hernández, *Opt. Express*, 16 (2) 957 (2008).

[191] H. Hundertmark, S. Rammler, T. Wilken, R. Holzwarth, T. W. Hänsch *et al.*, *Opt. Express*, 17 (3) 1919 (2009).

[192] G. Cerullo & S. D. Silvestri, *Review of Scientific Instruments*, 74 (1) 1 (2003).

[193] P. Tzankov, I. Buchvarov, & T. Fiebig, *Optics Communications*, 203 (12) 107 (2002).

[194] C. Nagura, A. Suda, H. Kawano, M. Obara, & K. Midorikawa, *Appl. Opt.*, 41 (18) 3735 (2002).

[195] P. Tzankov, T. Fiebig, & I. Buchvarov, *Applied Physics Letters*, 82 (4) 517 (2003).

[196] M. Ziolek, R. Naskrecki, & J. Karolczak, *Optics Communications*, 241 (13) 221 (2004).

[197] P. J. M. Johnson, V. I. Prokhorenko, & R. J. D. Miller, *Opt. Express*, 17 21488 (2009).

[198] H. E. Lessing & A. V. Jena, *Chem. Phys. Lett.*, 42 213 (1976).

[199] R. L. Fork, O. E. Martinez, & J. P. Gordon, *Opt. Lett.*, 9 150 (1984).

[200] C. H. B. Cruz, P. C. Becker, R. L. Fork, & C. V. Shank, *Opt. Lett.*, 13 123 (1988).

[201] S. Akturk, X. Gu, M. Kimmel, & R. Trebino, *Opt. Express*, 14 10101 (2006).

[202] V. I. Klimov & D. W. McBranch, *Opt. Lett.*, 23 277 (1998).

[203] R. L. Fork, C. V. Shank, C. Hirlimann, R. Yen, & W. J. Tomlinson, *Opt. Lett.*, 8 1 (1983).

[204] R. A. Negres, J. M. Hales, A. Kobyakov, & D. J. Hagan, *IEEE J. Quantum Electron.*, 39 392 (2003).

[205] W. Sellmeier, *Ann. Phys. Chem.*, 143 272 (1871).

[206] Schott optical glass collection datasheets (2012).

[207] Becker, *Advanced Time-Correlated Single Photon Counting Techniques*, Springer (2005).

[208] M. Matsumoto & T. Nishimura, *ACM Trans. Model. Comput. Simul.*, 8 (1) 3 (1998).

[209] M. Theander, A. Yartsev, D. Zigmantas, V. Sundström, W. Mammo *et al.*, *Phys. Rev. B*, 61 12957 (2000).

[210] J. E. Kroeze, T. J. Savenije, M. J. W. Vermeulen, & J. M. Warman, *J. Phys. Chem. B*, 107 7696 (2003).

[211] S. R. Scully & M. D. McGehee, *J. Appl. Phys.*, 100 034907 (2006).

[212] A. Hagfeldt, G. Boschloo, L. C. Sun, L. Kloo, & H. Pettersson, *Chem. Rev.*, 110 6595 (2010).

[213] I. K. Ding, N. Tetreault, J. Brillet, B. E. Hardin, E. H. Smith *et al.*, *Adv. Funct. Mater.*, 19 2431 (2009).

[214] Q. Wang, S. M. Zakeeruddin, M. K. Nazeeruddin, R. Humphry-Baker, & M. Grätzel, *J. Am. Chem. Soc.*, 128 4446 (2006).

[215] P. Docampo, A. Hey, S. Guldin, R. Gunning, U. Steiner *et al.*, *Adv. Funct. Mater.*, 22 5010 (2012).

[216] C. J. Barbe, F. Arendse, P. Comte, M. Jirousek, F. Lenzmann *et al.*, *J. Am. Ceram. Soc.*, 80 3157 (1997).

[217] S. Fantacci, F. De Angelis, M. K. Nazeeruddin, & M. Grätzel, *J. Phys. Chem. C*, 115 23126 (2011).

[218] B. E. Hardin, A. Sellinger, T. Moehl, R. Humphry-Baker, J.-E. Moser *et al.*, *J. Am. Chem. Soc.*, 133 10662 (2011).

[219] S. A. Haque, Y. Tachibana, R. L. Willis, J.-E. Moser, M. Grätzel *et al.*, *J. Phys. Chem. B*, 104 538 (2000).

[220] N. Hirata, J. E. Kroeze, T. Park, D. Jones, S. A. Haque *et al.*, *Chem. Commun.*, 2006 535 (2006).

[221] M. K. Nazeeruddin, A. Kay, I. Rodicio, R. Humphrybaker, E. Muller *et al.*, *J. Am. Chem. Soc.*, 115 6382 (1993).

[222] S. A. Haque, T. Park, C. Xu, S. Koops, N. Schulte *et al.*, *Adv. Funct. Mater.*, 14 435 (2004).

[223] S. A. Haque, E. Palomares, B. M. Cho, A. N. M. Green, N. Hirata *et al.*, *J. Am. Chem. Soc.*, 127 3456 (2005).

[224] S. N. Mori, W. Kubo, T. Kanzaki, N. Masaki, Y. Wada *et al.*, *J. Phys. Chem. C*, 111 3522 (2007).

[225] J. Salbeck, N. Yu, J. Bauer, F. Weissörtel, & H. Bestgen, *Synth. Met.*, 91 209 (1997).

[226] P. Strohriegl & J. V. Grazulevicius, *Adv. Mater.*, 14 1439 (2002).

[227] A. A. Dietrich Stauffer, *Introduction to Percolation Theory*, CRC Press (1994).

[228] M. F. Sykes & J. W. Essam, *J. Math. Phys.*, 5 1117 (1964).

[229] J. Garcia-Canadas, F. Fabregat-Santiago, H. J. Bolink, E. Palomares, G. Garcia-Belmonte *et al.*, *Synth. Met.*, 156 944 (2006).

[230] S. M. Zakeeruddin, M. K. Nazeeruddin, R. Humphry-Baker, P. Pechy, P. Quagliotto *et al.*, *Langmuir*, 18 952 (2002).

[231] E. T. Seo, R. F. Nelson, J. M. Fritsch, L. S. Marcoux, D. W. Leedy *et al.*, *J. Am. Chem. Soc.*, 88 3498 (1966).

[232] B. W. D'andrade, S. Datta, S. R. Forrest, P. Djurovich, E. Polikarpov *et al.*, *Org. Electron.*, 6 11 (2005).

[233] J. L. Bredas, R. Silbey, D. S. Boudreaux, & R. R. Chance, *J. Am. Chem. Soc.*, 105 6555 (1983).

[234] J. R. Jennings, Y. Liu, Q. Wang, S. M. Zakeeruddin, & M. Grätzel, *Phys. Chem. Chem. Phys.*, 13 6637 (2011).

[235] A. Zaban, S. Ferrere, & B. A. Gregg, *J. Phys. Chem. B*, 102 452 (1998).

[236] M. Planells, A. Abate, D. J. Hollman, S. D. Stranks, V. Bharti *et al.*, *J. Mater. Chem. A*, 1 6949 (2013).

[237] U. Bach, *Solid-State Dye-Sensitized Mesoporous TiO_2 Solar Cells*, Ph.D. thesis, École Polytechnique Fédérale de Lausanne (2000).

[238] G. Boschloo & A. Hagfeldt, *Chem. Phys. Lett.*, 370 381 (2003).

[239] M. K. Nazeeruddin, S. M. Zakeeruddin, J. J. Lagref, P. Liska, P. Comte *et al.*, *Coord. Chem. Rev.*, 248 1317 (2004).

[240] In a previous study, a value of 18700 L mol^{-1} cm^{-1} was found [146, 289]. We assume that the difference is mainly due to reasons of concentration calibration and not due to differences during the chemical oxidation measurement.

[241] We note that previous studies found a hole-transfer yield of 90-100% [15, 146]. The difference to the value of 75% found in this study is solely attributed to the assumption of a different molar extinction coefficent for spiro-OMeTAD radical cations at 520 nm, as detailed earlier.

[242] A. Mishra, N. Pootrakulchote, M. K. Wang, S. J. Moon, S. M. Zakeeruddin *et al.*, *Adv. Funct. Mater.*, 21 963 (2011).

[243] P. Docampo, S. Guldin, M. Stefik, P. Tiwana, M. C. Orilall *et al.*, *Adv. Funct. Mater.*, 20 1787 (2010).

[244] P. Tiwana, P. Docampo, M. B. Johnston, L. M. Herz, & H. J. Snaith, *Energy Environ. Sci.*, 5 9566 (2012).

[245] S. D. Stranks, C. Weisspfennig, P. Parkinson, M. B. Johnston, L. M. Herz *et al.*, *Nano Lett.*, 11 66 (2011).

[246] A. C. Morteani, P. Sreearunothai, L. M. Herz, R. H. Friend, & C. Silva, *Phys. Rev. Lett.*, 92 247402 (2004).

[247] T. Offermans, S. C. J. Meskers, M. M. Koetse, & R. A. J. Janssen, *Phys. Rev. B*, 72 045213 (2005).

[248] C. Yin, T. Kietzke, D. Neher, & H. H. Horhold, *Appl. Phys. Lett.*, 90 092117 (2007).

[249] H. Ohkita, S. Cook, Y. Astuti, W. Duffy, S. Tierney *et al.*, *J. Am. Chem. Soc.*, 130 3030 (2008).

[250] J. J. Benson-Smith, J. Wilson, C. Dyer-smith, K. Mouri, S. Yamaguchi *et al.*, *J. Phys. Chem. B*, 113 7794 (2009).

[251] A. T. Mallajosyula, S. S. K. Iyer, & B. Mazhari, *Nanoelectronics Conference, 2008. INEC 2*, 1 550 (2008).

[252] Y. Kanai & J. C. Grossman, *Nano Lett.*, 8 908 (2008).

[253] T. Schuettfort, H. Snaith, A. Nish, & R. Nicholas, *Nanotechnology*, 21 025201 (2010).

[254] R. G. S. Goh, N. Motta, J. M. Bell, & E. R. Waclawik, *Appl. Phys. Lett.*, 88 053101 (2006).

[255] R. B. Weisman & S. M. Bachilo, *Nano Lett.*, 3 1235 (2003).

[256] A. Gutierrez-llorente, G. Horowitz, R. Perez-casero, J. Perriere, J. L. Fave *et al.*, *Org. Electron.*, 5 29 (2004).

[257] X. M. Jiang, R. Österbacka, C. P. An, & Z. V. Vardeny, *Synth. Met.*, 137 1465 (2003).

[258] F. C. Spano, *Chem. Phys.*, 325 22 (2006).

[259] J. Clark, C. Silva, R. H. Friend, & F. C. Spano, *Phys. Rev. Lett.*, 98 206406 (2007).

[260] F. C. Spano, J. Clark, C. Silva, & R. H. Friend, *J. Chem. Phys.*, 130 074904 (2009).

[261] P. Parkinson, C. Müller, N. Stingelin, M. B. Johnston, & L. M. Herz, *J. Phys. Chem. Lett.*, 1 2788 (2010).

[262] O. J. Korovyanko, R. Österbacka, X. M. Jiang, Z. V. Vardeny, & R. A. J. Janssen, *Phys. Rev. B*, 64 235122 (2001).

[263] C. X. Sheng, M. Tong, S. Singh, & Z. V. Vardeny, *Phys. Rev. B*, 75 085206 (2007).

[264] M. Theander, O. Inganäs, W. Mammo, T. Olinga, M. Svensson *et al.*, *J. Phys. Chem. B*, 103 7771 (1999).

[265] S. Westenhoff, W. J. D. Beenken, R. H. Friend, N. C. Greenham, A. Yartsev *et al.*, *Phys. Rev. Lett.*, 97 166804 (2006).

[266] S. Trotzky, *J. Phys. D-Appl. Phys.*, 42 055105 (2009).

[267] M. H. Chang, M. Hoffmann, H. L. Anderson, & L. M. Herz, *J. Am. Chem. Soc.*, 130 10171 (2008).

[268] J. X. Geng, B. S. Kong, S. B. Yang, S. C. Youn, S. Park *et al.*, *Adv. Funct. Mater.*, 18 2659 (2008).

[269] F. M. Chen, W. J. Zhang, M. L. Jia, L. Wei, X. F. Fan *et al.*, *J. Phys. Chem. C*, 113 14946 (2009).

[270] C. G. Shuttle, R. Hamilton, B. C. ORegan, J. Nelson, & J. R. Durrant, *Proceedings of the National Academy of Sciences*, 107 (38) 16448 (2010).

[271] J. M. Guo, H. Ohkita, H. Benten, & S. Ito, *J. Am. Chem. Soc.*, 131 16869 (2009).

[272] R. "Osterbacka, C. P. An, X. M. Jiang, & Z. V. Vardeny, *Science*, 287 839 (2000).

[273] T. J. Savenije, J. E. Kroeze, X. N. Yang, & J. Loos, *Adv. Funct. Mater.*, 15 1260 (2005).

[274] I. W. Hwang, D. Moses, & A. J. Heeger, *J. Phys. Chem. C*, 112 4350 (2008).

[275] J. Piris, T. E. Dykstra, A. A. Bakulin, W. Knulst, M. T. Trinh *et al.*, *J. Phys. Chem. C*, 113 14500 (2009).

[276] G. Dicker, L. D. A. Siebbeles, & J. M. Warman, *Phys. Rev. B*, 70 045203 (2004).

[277] X. Ai, M. C. Beard, K. P. Knutsen, S. E. Shaheen, G. Rumbles *et al.*, *J. Phys. Chem. B*, 110 25462 (2006).

[278] E. Hendry, M. Koeberg, J. M. Schins, L. D. A. Siebbeles, & M. Bonn, *Chem. Phys. Lett.*, 432 441 (2006).

[279] X. Xu, K. Chuang, R. J. Nicholas, M. B. Johnston, & L. M. Herz, *J. Phys. Chem. C*, 113 18106 (2009).

[280] L. B. Huang & T. D. Krauss, *Phys. Rev. Lett.*, 96 057407 (2006).

[281] F. Wang, G. Dukovic, E. Knoesel, L. E. Brus, & T. F. Heinz, *Phys. Rev. B*, 70 241403 (2004).

[282] Y. Z. Ma, L. Valkunas, S. L. Dexheimer, S. M. Bachilo, & G. R. Fleming, *Phys. Rev. Lett.*, 94 157402 (2005).

[283] A. Hagen, M. Steiner, M. B. Raschke, C. Lienau, T. Hertel *et al.*, *Phys. Rev. Lett.*, 95 197401 (2005).

[284] T. G. Pedersen, *Phys. Rev. B*, 67 073401 (2003).

[285] V. Perebeinos, J. Tersoff, & P. Avouris, *Phys. Rev. Lett.*, 92 257402 (2004).

[286] H. Sirringhaus, N. Tessler, & R. H. Friend, *Science*, 280 1741 (1998).

[287] M. M. Lee, J. Teuscher, T. Miyasaka, T. N. Murakami, & H. J. Snaith, *Science*, 338 643 (2012).

[288] S. Q. Ren, M. Bernardi, R. R. Lunt, V. Bulovic, J. C. Grossman *et al.*, *Nano Lett.*, 11 5316 (2011).

[289] F. Weissörtel, *Amorphe, Niedermolekulare Ladungstransportmaterialien für Nanokristalline Solarzellen*, Diplomarbeit Universität Regensburg, 1996.

Abbreviations

AFM	Atomic force microscope
ASTM	American Society for Testing and Materials
BBO	β-barium borate
BK7	Borosilicate crown glass
CaF_2	Calcium fluoride
CPA	Chirped pulse amplification
CT	Charge-transfer state
DOS	Density of states
EQE	External quantum efficiency
FWHM	Full-width at half maximum
GaAs	Gallium arsenide
GVD	Group velocity dispersion
HOMO	Highest occupied molecular orbital
HTM	Hole-transporting material
HWP	Half-wave plate
IPCE	Incident-photon-to-electron conversion efficiency
IQE	Internal quantum efficiency
LiF	Lithium fluoride
LUMO	Lowest unoccupied molecular orbital
MWNT	Multi-walled carbon nanotube
ND	Neutral-density

OAP	Off-axis parabolic mirror
OFET	Organic field-effect transistor
OLED	Organic light-emitting diode
OPA	Optical parametric amplification
OPV	Organic photovoltaics
OS	Organic semiconductors
P3HT	Poly(3-hexylthiophene)
PCBM	[6,6]-phenyl-C_{61}-butyric acid methyl ester
PFF	Pore-filling fraction
PIA	Photoinduced absorption
PL	Photoluminescence
PLE	Photoluminescence excitation/emission
PLUC	Photoluminescence upconversion
SCG	Supercontinuum generation
SEM	Scanning electron microscope
SHG	Second harmonic generation
Si	Silicon
spiro-OMeTAD	2,2',7,7'-tetrakis(N,N-di-p-methoxyphenylamine)-9,9'-spirobifluorene
SWNT	Single-walled carbon nanotube
TAS	Transient absorption spectroscopy
TCSPC	Time-correlated single photon counting
TOF	Time-of-flight
UV-VIS	Ultraviolet-visible